#### Jean-Pierre André Immarigeon

SUBSTRUCTURAL CHANGES DURING THE TRANSIENT DEFORMATION OF ARMCO IRON AND SILICON STEEL

#### **ABSTRACT**

Cylinders of Armco iron and silicon steel were deformed at 675°C and at strain rates of 10<sup>-3</sup> and 10<sup>-1</sup> s<sup>-1</sup>. Two steady state substructures were produced with mean subgrain sizes of 2.4 and 1.2 µm respectively for the Armco iron and 2.0 and 1.3 µm for the silicon steel. The breakdown of the substructure upon an increase or decrease in strain rate was studied by means of electron microscopy. The final structures were similar to those developed through steady state deformation. In the Armco iron, the changes in subgrain size paralleled the gradual changes in flow stress and occurred over strains of 0.2 to 0.3. Thus the internal stress can be associated with the sub-boundary density. By contrast, in the silicon steel, only brief flow stress transients over strains of 0.05 to 0.08 or less were observed. However, the subgrain size continued to change during the period of constant flow stress. This indicated that the back stress in this case can be associated with the network dislocation density and not with the sub-boundary density.

# Short Title

"TRANSIENT DEFORMATION OF ARMCO IRON AND SILICON STEEL"

# SUBSTRUCTURAL CHANGES DURING THE TRANSIENT DEFORMATION OF ARMCO IRON AND SILICON STEEL

by

Jean-Pierre André Immarigeon

A thesis submitted to the Faculty of Graduate Studies and Research in partial fulfillment of the requirements for the degree of Master of Engineering

Department of Metallurgical Engineering

McGill University

Montreal

C Jean-Pierre André Immarigeon 1971

#### **ABSTRACT**

Cylinders of Armco iron and silicon steel were deformed at 675°C and at strain rates of 10<sup>-3</sup> and 10<sup>-1</sup> s<sup>-1</sup>. Two steady state substructures were produced with mean subgrain sizes of 2.4 and 1.2 µm respectively for the Armco iron and 2.0 and 1.3 µm for the silicon steel. The breakdown of the substructure upon an increase or decrease in strain rate was studied by means of electron microscopy. The final structures were similar to those developed through steady state deformation. In the Armco iron, the changes in subgrain size paralleled the gradual changes in flow stress and occurred over strains of 0.2 to 0.3. Thus the internal stress can be associated with the sub-boundary density. By contrast, in the silicon steel, only brief flow stress transients over strains of 0.05 to 0.08 or less were observed. However, the subgrain size continued to change during the period of constant flow stress. This indicated that the back stress in this case can be associated with the network dislocation density and not with the sub-boundary density.

#### RESUME

L'auteur rapporte des essais de compression à chaud (675°C) sur des échantillons cylindriques de fer Armco et d'acier au silicium. La machine d'essais Instron, a été modifiée en vue de l'obtention d'une vitesse de déformation constante. On a produit, à des vitesses de déformation de 10<sup>-3</sup> et de 10<sup>-1</sup> s<sup>-1</sup>, deux sous-structures d'état de régime caractérisées, entre autres, par des tailles moyennes de sous-grains de 2.4 et 1.2 μm dans le fer Armco et de 2.0 et 1.3 μm dans l'acier au silicium.

On a étudié au microscope électronique l'évolution des sousstructures à la suite d'un changement de vitesse de déformation de 10<sup>-3</sup> à 10<sup>-1</sup> s<sup>-1</sup> et vice-versa. Les structures définitives obtenues tant à la suite d'une déformation transitoire qu'à la suite d'une déformation de régime se sont révélées semblables. Toutefois, les périodes transitoires n'étaient pas les mêmes dans les deux matériaux étudiés. Pour ce qui est du fer Armco, les changements structurels vont de paire avec les changements de la contrainte d'écoulement et interviennent au cours d'une déformation rationnelle de l'ordre de 0.2 à 0.3. Par contre, en ce qui concerne l'acier au silicium, on n'observe que de brèves périodes transitoires dans la contrainte, correspondant à une déformation rationnelle de 0.05 à 0.08 ou moins. La taille des sous-grains continue à se modifier alors que la contrainte d'écoulement s'est déjà fixée à une valeur constante de régime. Ces observations indiquent que ni la contrainte interne ni la contrainte d'écoulement ne sont directement déterminées par la densité des sous-joints dans l'acier au silicium.

Les résultats de l'étude au microscope électronique étayent la validité d'un modèle pour la déformation à haute temperature fondé sur la notion de contrainte effective. Dans ce modèle, les sous-joints et la densité du réseau de dislocations contribuent aux contraintes internes. Bien que dans le cas du fer Armco l'on puisse attribuer l'origine des contraintes internes à la densité des sous-joints, une semblable correlation n'est pas valable pour l'acier au silicium. Dans ce dernier cas on peut associer les contraintes internes à la densité du réseau de dislocations.

Les résultats actuels montrent que pour les opérations de corroyage au niveau industriel, on peut évaluer les pressions requises à
partir des résultats indiqués par la déformation à l'état de régime.

Cette conclusion résulte du fait que les changements des contraintes
internes sont relativement peu importants par rapport aux changements
des contraintes effectives.

#### ACKNOWLEDGEMENTS

The author wishes to express his sincere gratitude and appreciation to Dr. J. J. Jonas, director of this research, for his useful guidance and constant encouragement.

The author would also like to express his particular gratitude to Mr. M. J. Luton, who designed the essential features of the high temperature compression train, and whose advice and helpful suggestions were greatly appreciated.

Thanks are also due to Dr. D. J. Abson, whose useful comments contributed to the solution of problems of mutual interest, particularly in the field of electron microscopy.

Grateful acknowledgement must also be made for the assistance of Messrs. M. Knoepfel, L. J. Vroomen and F. Caresi in the construction of the equipment and of Mr. O. Muehling in the preparation of the specimens.

The writer would like to thank the Aluminum Company of Canada Limited for the provision of a fellowship (Alcan Research and Development Graduate Fellowship) and the Defence Research Board of Canada for financial support through Grant No. 9535-34. The writer also acknowledges the receipt of the Horace Young Fellowship.

# TABLE OF CONTENTS

ABSTRACT	T.	í
RESUME		ii
ACKNOWLEDG:	EMENTS	iv
TABLE OF C		v
LIST OF FIG		vii
LIST OF TAI	BLES	×
		•
INTRODUCTION	ON	
en . 1	HIGH MURCHEN AND DEPONANTON	
Chapter 1.	HIGH TEMPERATURE DEFORMATION	
	1.1 Definition of Hot Working	,
	1.2 Hot Working Investigations	
	1.3 The Nature of the Stress-Strain Curve under	
•	Hot Working Conditions	
	1.4 Empirical Flow Stress Relationships	• ;
	1.4.1 Interdependence of stress and strain rate	
	1.4.2 Interdependence of stress and temperature	10
	1.5 Microstructural Changes in High Temperature	
	Deformation	14
	1.5.1 Steady state microstructure during creep	
	and hot working	1.
	A. Subgrain formation	10
	B. Subgrain size	1
	C. Subgrain misorientation and the nature	
	of sub-boundaries	18
	D. Dislocations within subgrains	20
	1.5.2 Dynamic recovery mechanisms in hot working	2:
	1.5.3 Dynamic recrystallization	2:
	1.6 Theories of Hot Working	24
	1.6.1 Jogged screw-dislocation models	26
	1.6.2 Climb models	28
	1.6.3 Network models	29
	1.6.4 Effective stress models	30
_		
Chapter 2.	EXPERIMENTAL MATERIALS AND APPARATUS	37
	2.1 Experimental Materials	37
	2.2 Specimen Preparation	37
	2.2.1 Machining	37
	2.2.2 Strain-annealing	39
	2.3 High Temperature Compression Machine	42
	2.3.1 Description of the modified Instron	
	compression machine	43
	A. Quenching device	43
	B. Temperature control	46
	C. Atmosphere control	46
	2.3.2 Strain rate controller and load detector	47

	<ul><li>2.3.3 Load and strain recording</li><li>2.3.4 Experimental range of the equipment</li><li>2.4 High Temperature Lubricants</li></ul>	50 52 53
Chapter 3.	EXPERIMENTAL PROCEDURE	54
	<ul> <li>3.1 Testing Procedure</li> <li>3.2 Measurement of the Deformation Variables</li> <li>3.3 Calculation of True Stress and True Strain</li> <li>3.4 Preparation of Specimens for Optical Metallography</li> <li>3.5 Preparation of Specimens for Electron Microscopy</li> <li>3.5.1 Sectioning of specimens</li> </ul>	54 55 56 57 57
	<ul> <li>3.5.2 Mechanical polishing of specimens</li> <li>3.5.3 Thinning procedures <ul> <li>A. Jet machining and electrolytic thinning</li> <li>B. Chemical thinning</li> </ul> </li> <li>3.5.4 Electron microscopy</li> </ul>	58 60 60 63 63
	3.6 Determination of Subgrain Size 3.6.1 Planimetric method (Jeffries' procedure) 3.6.2 Intercept method (Heyn's procedure)	65 65 66
Chapter 4.	EXPERIMENTAL RESULTS	68
	4.1 True Stress-True Strain Curves 4.1.1 Elastic compression of the testing train under load	68
	4.1.2 Transient stress-strain behaviour 4.1.3 Reproducibility of tests	76 77 78
	4.2 Electron Microscopy 4.2.1 Steady state substructures 4.2.2 Transient region substructures	79 79 82
	4.3 Subgrain Size Measurements	90
Chapter 5.	DISCUSSION	100
	5.1 True Stress-True Strain Curves 5.1.1 General features of the curves 5.1.2 Characteristics of the transient region	100 100 103
	<ul><li>5.2 Microstructural Changes during Transient Deformation</li><li>5.2.1 Subgrain size determination</li><li>5.2.2 Subgrain size distributions</li></ul>	106 106 108
	5.2.3 Sub-boundary misorientation and dislocation density 5.2.4 Substructure under transient conditions	109 111
	<ul><li>5.3 Applicability of the Effective Stress Model</li><li>5.4 Industrial Significance of the Present Results</li><li>5.5 Suggestions for Further Work</li></ul>	111 114 117
CONCLUSIONS		119
REFERENCES		121

# LIST OF FIGURES

FIGURE	• 1	Typical true stress-true strain curves in hot working.	6
FIGURE	2	Relation between the Zener-Hollomon parameter Z and sinh ( $\alpha\sigma$ ) for $\beta$ -Ti, $\alpha$ -Zr and $\gamma$ -U (after Jonas and Immarigeon (38)).	13
FIGURE	3	Variation of the Zener-Hollomon parameter Z with flow stress $\sigma$ , illustrating the increase in $\emptyset_f$ and decrease in V with increasing $\sigma$ (after Jonas and Immarigeon (38)).	32
FIGURE	4	Behaviour of the internal and effective stresses following a strain rate change.	34
FIGURE	5	Specimen and modified thread chaser geometry.	41
FIGURE	6	General layout of the equipment.	44
FIGURE	7	Cross-section of the hot compression train.	45
FIGURE	8	Gas purification train.	48
FIGURE	9	Circuit diagrams for the constant strain rate device and the load detector .	51
FIGURE	10	Polishing holder for thin slices.	59
FIGURE	11	Circuit diagram of the DC power supply.	62
FIGURE	12	True stress-true strain curves for Armco iron.	69
FIGURE	13	True stress-true strain curves for silicon steel.	70
FIGURE	14	True stress-true strain curve for Armco iron showing the effect on the flow stress of:	
		<ul><li>a) a sudden increase in strain rate</li><li>b) a sudden decrease in strain rate.</li></ul>	71
FIGURE	15	True stress-true strain curve for silicon steel showing the effect on the flow stress of:	
		<ul><li>a) a sudden increase in strain rate</li><li>b) a sudden decrease in strain rate.</li></ul>	72
FIGURE	16	Armco iron quenching sequence along the transient resulting from a strain rate increase:	
		<ul><li>a) uncorrected</li><li>b) corrected for elastic compression of the testing train.</li></ul>	73

FIGURE	17	Armco iron quenching sequence along the transient resulting from a strain rate decrease:	
		<ul><li>a) uncorrected</li><li>b) corrected for elastic compression of the testing train.</li></ul>	74
FIGURE	18	Silicon steel quenching sequence along the transient resulting from a strain rate increase:	
		<ul><li>a) uncorrected</li><li>b) corrected for elastic compression of the testing train.</li></ul>	75
FIGURE	19	Electron micrograph of Armco iron deformed at $675^{\circ}$ C and at $10^{-3}$ s <sup>-1</sup> . $\epsilon$ = 0.74.	80
FIGURE	20	Electron micrograph of Armco iron deformed at $675^{\circ}$ C and at $10^{-1}$ s <sup>-1</sup> . $\epsilon$ = 0.52.	80
FIGURE	21	Electron micrograph of silicon steel deformed at $675^{\circ}C$ and at $10^{-3}$ s <sup>-1</sup> . $\epsilon$ = 0.82.	81
FIGURE	22	Electron micrograph of silicon steel deformed at $675^{\circ}$ C and at $10^{-1}$ s <sup>-1</sup> . $\epsilon$ = 0.53.	81
FIGURE		Electron micrograph of Armco iron deformed at $675^{\circ}$ C. Transient region following a strain rate change from $10^{-3}$ to $10^{-1}$ s <sup>-1</sup> $\epsilon$ = 0.04 after change.	83
FIGURE		Electron micrograph of Armco iron deformed at $675^{\circ}$ C. Transient region following a strain rate change from $10^{-3}$ to $10^{-1}$ s <sup>-1</sup> . $\epsilon$ = 0.11 after change.	83
FIGURE		Electron micrograph of Armco iron deformed at $675^{\circ}$ C. Transient region following a strain rate change from $10^{-3}$ to $10^{-1}$ s <sup>-1</sup> . $\epsilon$ = 0.14 after change.	84
FIGURE	1	Electron micrograph of Armco iron deformed at $675^{\circ}$ C. Transient region following a strain rate change from $10^{-3}$ to $10^{-1}$ s <sup>-1</sup> . $\epsilon$ = 0.57 after change.	84
FIGURE		Electron micrograph of Armco iron deformed at $675^{\circ}$ C. Transient region following a strain rate change from $10^{-1}$ to $10^{-3}$ s <sup>-1</sup> . $\epsilon$ = 0.03 after change.	85
FIGURE	•	Electron micrograph of Armco iron deformed at $675^{\circ}$ C. Transient region following a strain rate change from $10^{-1}$ to $10^{-3}$ s <sup>-1</sup> . $\varepsilon$ = 0.08 after change.	85
FIGURE	7	Electron micrograph of Armco iron deformed at $675^{\circ}$ C. Fransient region following a strain rate change from $10^{-1}$ to $10^{-3}$ s <sup>-1</sup> . $\epsilon$ = 0.17 after change.	86

FIGURE 30	Electron micrograph of Armco iron deformed at 675°C. Transient region following a strain rate change from $10^{-1}$ to $10^{-3}$ s <sup>-1</sup> . $\varepsilon = 0.32$ after change.	86
FIGURE 31	Electron micrograph of silicon steel deformed at $675^{\circ}$ C. Transient region following a strain rate change from $10^{-3}$ to $10^{-1}$ s <sup>-1</sup> . $\epsilon$ = 0.03 after change.	87
FIGURE 32	Electron micrograph of silicon steel deformed at $675^{\circ}$ C. Transient region following a strain rate change from $10^{-3}$ to $10^{-1}$ s <sup>-1</sup> . $\epsilon$ = 0.06 after change.	87
FIGURE 33	Electron micrograph of silicon steel deformed at $675^{\circ}$ C. Transient region following a strain rate change from $10^{-3}$ to $10^{-1}$ s <sup>-1</sup> . $\epsilon$ = 0.09 after change.	88
FIGURE 34	Electron micrograph of silicon steel deformed at $675^{\circ}$ C. Transient region following a strain rate change from $10^{-3}$ to $10^{-1}$ s <sup>-1</sup> . $\epsilon$ = 0.25 after change.	88
FIGURE 35	Electron diffraction pattern from a cluster of subgrains in Armco iron (111 reflections).	89
FIGURE 36	Electron diffraction pattern from a cluster of subgrains in silicon steel (110 reflections).	89
FIGURE 37	Variation of subgrain size during the transient deformation of Armco iron:	
	<ul><li>a) strain rate increase</li><li>b) strain rate decrease.</li></ul>	96
FIGURE 38	Variation of subgrain size during the transient deformation of silicon steel.	97
FIGURE 39	Subgrain size distributions in silicon steel during transient deformation following a strain rate increase.	98
FIGURE 40	Comparison of transient and steady state flow stresses.	116.

# LIST OF TABLES

TABLE	I	ACTIVATION ENERGIES IN SELF DIFFUSION AND IN HIGH TEMPERATURE DEFORMATION.	12
TABLE	II	CHEMICAL COMPOSITION OF THE MATERIALS.	38
TABLE	III	SPECIMEN PREPARATION PROCEDURE.	40
TABLE	IV	GLASS LUBRICANT FOR HIGH TEMPERATURE DEFORMATION.	53
TABLE	V	MEAN SUBGRAIN SIZES IN IRON DEFORMED AT HIGH TEMPERATURES.	92
<b>FA</b> BLE	VI	EXPERIMENTAL MEAN SUBGRAIN SIZES FOR ARMCO IRON.	94
FABLE	VII	EXPERIMENTAL MEAN SUBGRAIN SIZES FOR SILICON STEEL.	95

#### INTRODUCTION

High temperature forming is used extensively in industry because the relatively low flow stresses involved and the high ductilities encountered allow for large reductions without intermediate annealing. Not only is the flow stress-ductility combination obtainable in hot working superior to that which results from cold working followed by annealing, but it also requires less massive equipment. Most of the steel produced today, except for foundry products, is hot worked during processing and up to 80% of it is marketed in the hot finished condition. Clearly, hot working is of great industrial importance. However, it is only recently that the fundamental mechanisms taking place during high temperature deformation have been investigated.

The behaviour of metals during high temperature deformation is not completely understood. Since the conditions of hot working determine the final mechanical properties of the material, various researchers have begun to investigate the effect of the different variables on the end product. Most of the work carried out to date has dealt with steady state deformation, that is with deformation at constant temperature and strain rate. However, industrial hot working operations are not usually carried out under constant conditions, but at varying local strain rates and temperatures. During such unsteady or transient deformation, the substructural characteristics are continuously changing. Since strength and structure are intimately related, it is now of importance to determine the relationship between the deformation variables, namely strain rate, stress, temperature and structure, during transient deformation.

In the present work the changes in substructure following a rapid change in strain rate, that is during the transition from one set of steady state conditions to another, are investigated. The relation between the internal stresses that oppose the deformation and the structural changes during unsteady deformation are also discussed. The main purpose of the investigation was to increase our knowledge of substructure strengthening under transient conditions, an increased understanding of which will eventually lead to the development of stronger creep resistant and ambient temperature materials.

#### Chapter 1

## HIGH TEMPERATURE DEFORMATION

In this section the background relevant to the present work will be outlined. Following a definition of hot working, the flow curve will be described, and the different relationships linking the deformation variables will be surveyed. Particular emphasis will be given to substructural changes during hot working and high temperature creep. The reason for including creep in this study is that, as suggested by some workers, hot working can reasonably be considered as creep carried out at relatively high strain rates. Theories of high temperature deformation as applied to steady state creep and hot working will be reviewed, as well as some more recent proposals involving internal and effective stresses, which can describe both transient and steady state deformation.

#### 1.1 Definition of Hot Working

Hot working can be defined as a deformation process carried out at high temperatures and strain rates. In this context high temperature refers to those temperatures at which restoration processes can occur during the deformation. Since metals have different melting temperatures, a homologous temperature, or fraction of the melting temperature (in degrees Kelvin) is used for comparison purposes. Hot working temperatures are then those above 0.5  $T_m$  ( $T_m$ -melting temp.,  $^O$ K). The true strain rates at which the deformations are carried out are usually in the range from .01 to 500 s<sup>-1</sup>. Very large strains can be achieved, as almost no strain

hardening occurs, since the high temperatures favour the operation of various restoration processes. In brief, hot working can be defined as a type of deformation during which strain hardening and dynamic softening processes are concurrent.

## 1.2 Hot Working Investigations

A relatively limited amount of work has been carried out in the field of hot working for various reasons. First, it has been possible for industrial concerns to turn out satisfactory products without the help of fundamental theories. Second, the establishment of such theories requires extensive investigation covering very wide ranges of the deformation variables. Thus, the experimental work involved is in general quite complex and demanding, and the experimental apparatus required is not readily available. However, in view of the continuous development of new materials such as the super-alloys, and of the increase in complexity of the strengthening mechanisms which are of importance in such materials, a need has more recently been felt for the establishment of a suitable theoretical framework.

The modern investigation of the principles of hot working began with the researches of Rossard and co-workers  $^{(1-7)}$  in the late fifties. They carried out hot torsion testing on various steels at IRSID in France. The mechanisms of hot working have also been investigated by Sellars and Tegart and co-workers in Sheffield  $^{(8-13)}$ , by Stüwe and associates in Aachen  $^{(14,15)}$ , by Shapiro and Dieter at Drexel  $^{(16,17)}$  and by McQueen and Jonas and co-workers in Montreal  $^{(18-34)}$ . Recently, the present author has studied the substructural changes taking place during the hot rolling of aluminum  $^{(35)}$ , and has also carried out an analysis of Bühler's hot comp-

ression data<sup>(36,37)</sup> for titanium, zirconium and uranium<sup>(38)</sup>. The more detailed aspects of some of these investigations will now be considered in turn.

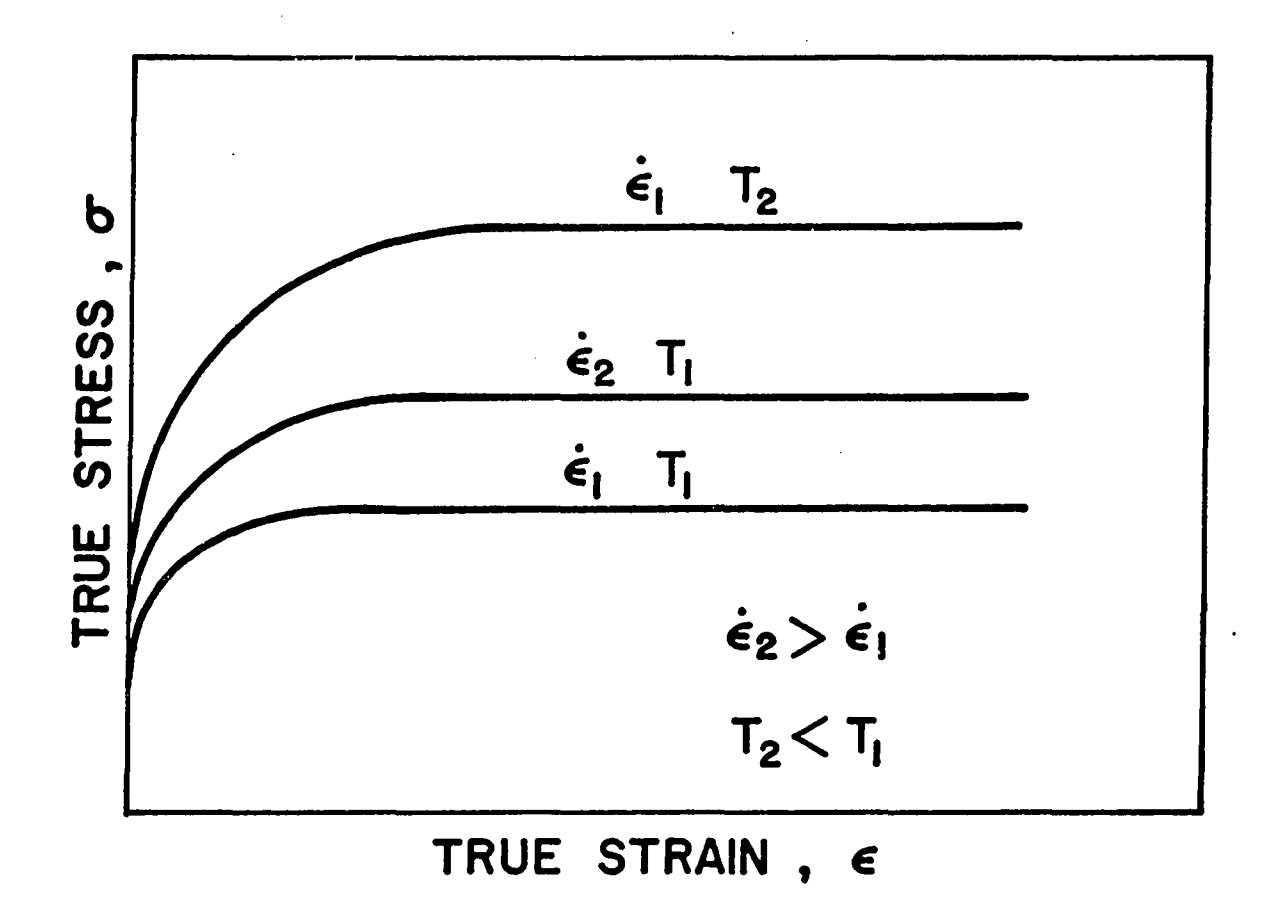
## 1.3 The Nature of the Stress-Strain Curve under Hot Working Conditions

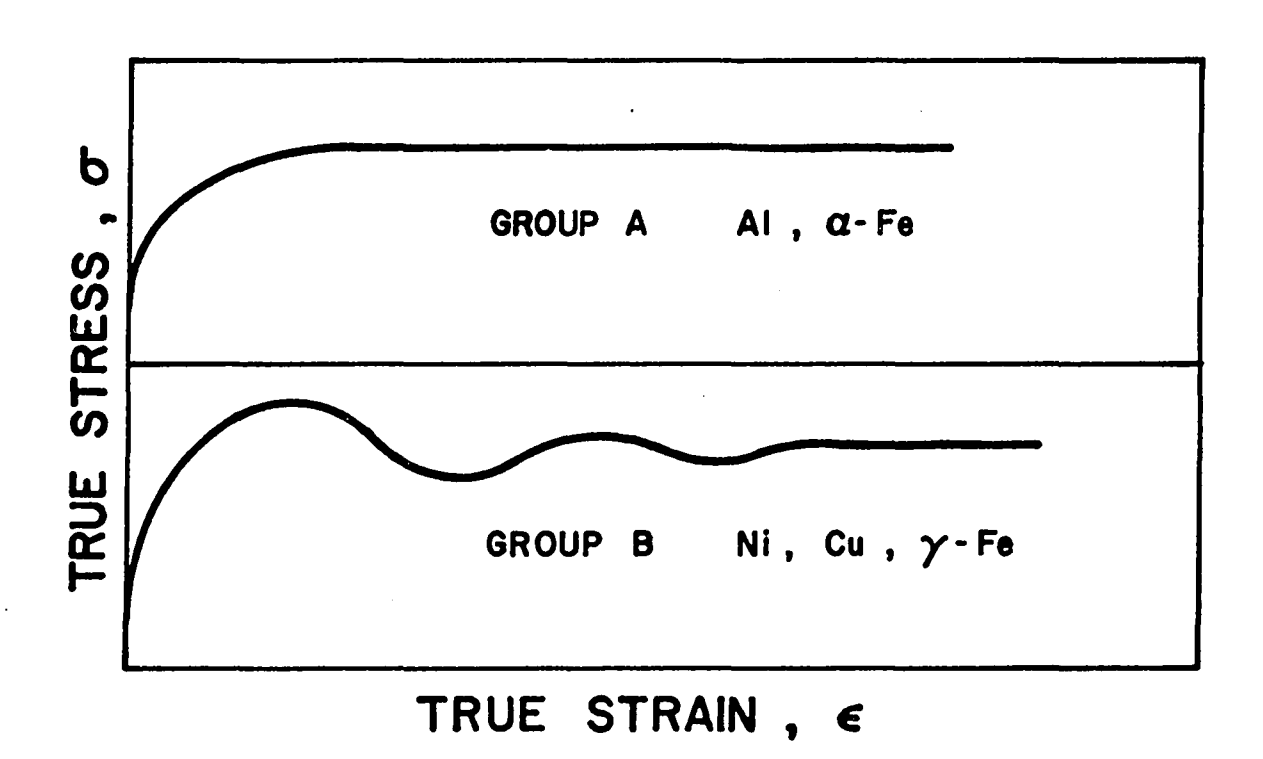
Before discussing quantitative relationships between hot working variables, it is necessary to examine the main features of the true stress-true strain curve under hot working conditions. The interdependence of the deformation variables, namely stress, strain, strain rate and temperature, can be described by a set of curves in which the uniaxial flow stress is plotted against true strain at various strain rates and temperatures. The main features of such curves have been discussed by previous investigators (2,5,8,14,27,31) and their observations will now be considered with particular reference to the shapes of the curves obtained during the hot compression of iron and steel.

The significant features of the curves shown in Fig.1 are a transient region and a subsequent steady state region. In the transient region, the true stress rises rapidly with strain until a peak stress is reached. The slope of the curve,  $h = d\sigma/d\epsilon$ , is a measure of the net hardening rate. When the dynamic softening rate becomes equal to the hardening rate, the steady state region is established. Under steady state conditions, the flow stress is constant and independent of strain. The steady state flow stress increases with an increase in strain rate or a decrease in temperature  $^{(31)}$ . A peak in stress usually precedes the establishment of the steady state. The strain to the peak stress increases with strain rate at a given temperature. It also increases with a decrease in temperature at a given strain rate. Furthermore, the peak and its width are more

FIGURE 1.

Typical true stress-true strain curves in hot working





pronounced at high strain rates or at low temperatures (5,8,31). For certain metals the peak is followed by oscillations which gradually damp out (5,12). It has also been observed that lower flow stresses lead to greater ductility (8). The modes of deformation do not seem to affect the shape of the true stress-true strain curve (5,31). However, the softening at the onset of the steady state appears to be more marked in torsion than in the other test methods. For example, in the case of Armco iron and silicon steel, the curves obtained by hot compression (25-27) do not exhibit pronounced peaks before the inception of the steady state, unlike the curves obtained from hot torsion. The dependence of the flow stress on strain rate and temperature indicates that the mechanisms involved in hot working can be regarded as thermally activated processes. This aspect of high temperature deformation will be discussed in more detail later.

Similar steady state behaviour has been observed in the creep range of strain rates (10<sup>-8</sup> to 10<sup>-4</sup> s<sup>-1</sup>) (40-43). When a metal is deformed at high temperature and under a constant stress, an initial transient precedes a linear increase in strain with time. In other words, a steady state is established during which the stress, the strain rate and the temperature remain constant. This is equivalent to the steady state regime in flow stress described earlier. The transient creep region can be compared with the hardening stage of hot working. It is interesting to note that the experimental procedures involved in hot working studies differ from those of creep in that, in the former, a deformation rate is imposed upon the specimen and the induced flow stress is measured. In the latter, a constant stress is applied to the specimen, and the strain rate is measured. However, in both cases a steady state results, in

which the flow stress and strain rate remain constant.

#### 1.4 Empirical Flow Stress Relationships

## 1.4.1 <u>Interdependence of stress and strain rate</u>

A number of investigators have proposed various mathematical expressions to correlate strength with strain rate and temperature.

Early attempts made use of a power relationship where the flow stress is given by:

$$\sigma_{\varepsilon} = \sigma_{O}(T) \dot{\varepsilon}^{N(T)} \tag{1-1}$$

Here  $\sigma_0(T)$  and N(T) are temperature dependent constants, which are also strain dependent at low strains. It has been reported (11) that an equation of the form

$$\dot{\varepsilon}_{s} = A' \sigma^{n} \tag{1-2}$$

can be used successfully to fit high strain rate data for low stresses.

At high stresses the data are better described by an exponential law of the form

$$\dot{\varepsilon}_{S} = A'' \exp(\beta \sigma) \tag{1-3}$$

Both these relations describe steady state deformation and are similar to those proposed for high temperature steady state creep  $^{(40)}$ . Since high temperature deformation appears to be thermally activated, an Arrhenius term (exp(- Q/RT) has frequently been added to the above relations. This led Sellars and Tegart  $^{(11)}$  to apply to hot working data the following more general equation, first proposed by Garofalo for steady state creep  $^{(44)}$ :

$$\dot{\varepsilon}_{S} = A \sinh(\alpha\sigma)^{n'} \exp(\frac{-Q}{RT})$$
 (1-4)

Here A,  $\alpha$  and n' are temperature independent constants and Q is an apparent activation energy. It is interesting to note that at high stresses (for  $\alpha\sigma > 1.2$ ) Eq.(1-4) reduces to an exponential relation, whereas at low stresses ( $\alpha\sigma < 0.8$ ) it approximates to a power relation because of the nature of the power hyperbolic sine function. In Eq.(1-4) the constants  $\alpha$  and n' are related to  $\beta$  of Eq.(1-3) by the relation  $\beta=\alpha n'$ . Direct analysis of creep and hot working data can therefore lead to the determination of  $\alpha$  and n'. Eq.(1-4) has been used to fit data from creep and hot working experiments and has generally been found satisfactory (11, 20,23-27,38,45). Recently, a modification of Eq.(1-4) was proposed (26), in order to cover not only the steady state, but also the transient regime between two steady state conditions. The proposed relation reads:

$$\dot{\varepsilon} = A_1 S_d \sinh(S_{\Theta} \sigma)^m \exp(\frac{-Q}{RT})$$
 (1-5)

where  $S_d$  and  $S_{\odot}$  are substructure parameters,  $S_d$  being related to the average subgrain size and  $S_{\odot}$  to the average subgrain misorientation. The validity and limitations of Eq.(1-5) are discussed in reference 26. Eq.(1-4) can be rearranged in terms of the Zener-Hollomon parameter  $Z = \dot{\varepsilon} \exp(Q/RT)$  as:

$$Z = A \sinh(\alpha\sigma)^{n'}$$
 (1-6)

This relation has been used to correlate creep and hot working data by various investigators. However, it is difficult to explain Eq.(1-6) in terms of a theoretical model  $^{(46)}$ , and the constants A,  $\alpha$  and n' cannot be given any simple physical interpretation. This difficulty can be overcome by the use of an exponential stress law of the form  $^{(32,46)}$ .

$$\dot{\varepsilon} = A_3 \exp(\beta \sigma) \exp(\frac{-Q}{RT})$$
 (1-7)

or 
$$Z = A_3 \exp(\beta \sigma)$$
 (1-8)

where A<sub>3</sub> is a structure factor related to the density of mobile dislocations or of activatable sites, and  $\beta=v/RT$ , where v is an apparent activation volume. Eq.(1-8) has been applied to various FCC, BCC and HCP metals (32,38,46). It is interesting to note that Eq.(1-8) can be derived from rate theory without specifying any particular model (31).

The good correlation between creep and hot working data when Eq. (1-4) is used, and the similarity obtained between the constants for hot working and those for creep (40), suggest that similar mechanisms are involved in both high temperature deformation processes (29).

#### 1.4.2 Interdependence of stress and temperature

When creep or hot working data are fitted by means of the power hyperbolic sine law,  $(\epsilon_s^{\alpha}[\sinh(\alpha\sigma)]^n)$  a series of parallel straight lines is obtained, one for each temperature. The temperature dependence can then be calculated by plotting at constant strain rate the variation of the flow stress against the reciprocal of the absolute temperature. Alternatively, the strain rate can be plotted against the reciprocal temperature at a given stress (11,20,26,38). The apparent activation energy for steady state high temperature deformation is determined from the slope of such curves, since manipulation of Eq. (1-4) leads to:

$$Q = -2.3 R \left( \frac{\partial \log \dot{\varepsilon}}{\partial 1/T} \right)_{\sigma}$$
 (1-9)

$$Q = -2.3 R \left( \frac{\partial \log \dot{\epsilon}}{\partial 1/T} \right)_{\sigma}$$

$$Q = 2.3 R \left( \frac{\partial \log \dot{\epsilon}}{\partial \log(\sinh \alpha \sigma)} \right)_{T} \left( \frac{\partial \log(\sinh \alpha \sigma)}{\partial 1/T} \right)_{\dot{\epsilon}}$$

$$(1-9)$$

In the above, it is assumed that the structure depends on the steady state stress alone and is independent of temperature (31).

Hot working can therefore be considered to be, like creep, a thermally activated process. The Arrhenius term which enters all the

above equations is simply a measure of the rate at which the deformation process will be aided by thermal fluctuations at a given temperature. According to this view, the activation energy corresponds to an energy barrier which must be overcome by moving dislocations for the deformation to proceed. It can be regarded as the "height" of the obstacles involved in the rate-controlling glide or dynamic softening mechanism. Apparent activation energies have been determined for various FCC, BCC and HCP metals (11,12,23,26,45) These values can be compared with other activation energies associated with hot deformation, namely those for creep and self diffusion. This is done in Table I. It is clear from a study of this table, that metals and alloys can be grouped into two categories with regard to hot working activation energies. In the first group, the activation energies are very similar to those for self diffusion, whereas in the other category, the values can differ substantially from the self diffusion energies, and from those of creep. This indicates that in the former cases recovery is rate controlling over a very wide range of strain rates, while in the latter cases, the controlling process is recovery during creep but may be recrystallization during hot working. A more thorough discussion of such anomalies can be found in the original papers.

We have now reviewed some of the more important equations for the correlation of the flow parameters involved in high temperature - high strain rate deformation. Fig.2 shows the data for three metals plotted according to one of these equations (Eq.(1-8)) (38). Similar correlations have been obtained for various other metals and solid solution alloys. From Fig.2 it can be seen that a higher flow stress results from a lower temperature or a higher strain rate, and plots of this type can be used

TABLE I

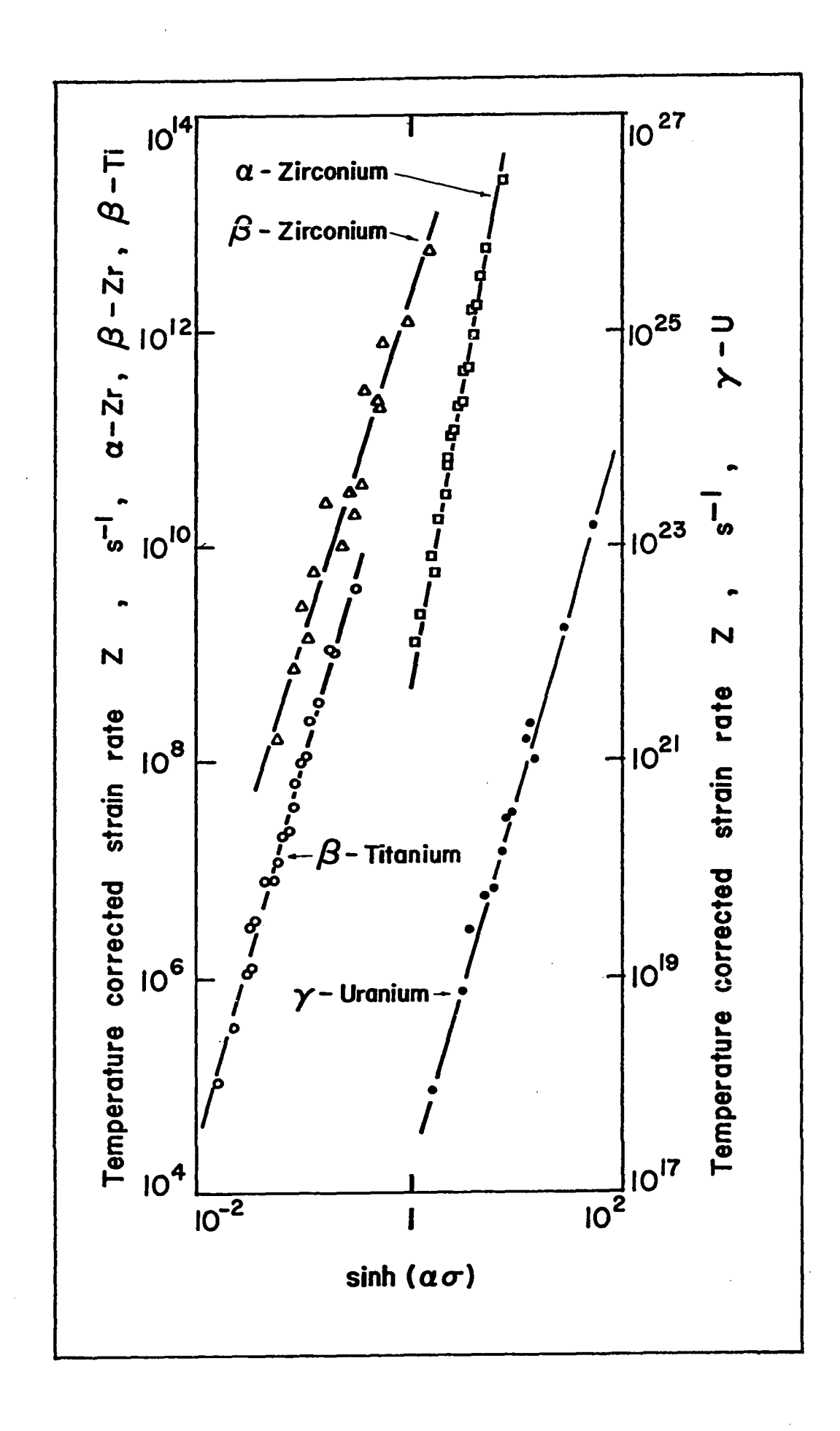
ACTIVATION ENERGIES (Kcal/gm atom) IN SELF DIFFUSION AND IN HIGH TEMPERATURE DEFORMATION

Material	$^{\Delta  ext{H}}$ Self diffusion	Ref.	<sup>∆H</sup> Creep	Ref.	<sup>ΔΗ</sup> Hot working	Ref.
A1	33	40	33–36	40	37	23–26
Ni - 20% Fe	70 53 Ni in Ni-Fe 53 Fe in Ni-Fe	40 *	65–67 48	40 *	71 (comm. pur.) 56 (hi. pur.) 94	11 12 12
Cu	44-56	40	47–56	40	72	11
Fe - 0.03% C (α) Fe - 2.8% Si (α) Fe - 0.25% C (γ)	57-67 48 Si in Fe-Si 56 Fe in Fe-Si 59	40 * * 40	68 75 74	40 * 40	66 80 73	26 26
Zn	23	*	21 0.5-0.6T <sub>m</sub> 38 0.8-1.0T <sub>m</sub>	* *	23	45
Ti (β)	30-49	**			41	38
υ (γ)	27-29	**	42-122	**	107	38
Zr (α) Zr (β)	22-67 21-65	** **	51-78 32-45	** **	46 63	38 38

<sup>\*</sup> data collected by Jonas et al (31) \*\* data collected by Jonas and Immarigeon (38)

# FIGURE 2.

Relation between the Zener-Hollomon parameter Z and sinh( $\alpha\sigma$ ) for  $\beta$ -Ti,  $\alpha$ -Zr and  $\gamma$ -U (after Jonas and Immarigeon (38))



to predict industrial working loads. Fig.2 also suggests that hot deformation is a thermally activated process. According to such an interpretation, fewer activated events take place per unit time at low temperatures, and at high speeds, more mechanical assistance must be provided for the thermally activated events to take place (29).

# 1.5 Microstructural Changes in High Temperature Deformation

It has generally been observed that significant structural changes take place during high temperature deformation. Since these changes can be used to test the various proposed deformation mechanisms, it is of importance that they be described not only as being of scientific interest but as a matter of practical importance, inasmuch as strength and structure are closely related. In this section, the main features of the structual changes taking place during creep and hot working will be reviewed, since both processes behave in a similar manner with regard to such changes.

There are many similarities between the structures developed during high and low temperature deformation (47). This is not surprising, since the same dislocation interactions can take place in both cases. However, as the temperature is raised, processes that are difficult to activate at low temperatures, such as recovery or recrystallization, can contribute increasingly to the final arrangement of dislocations. During cold working, a cellular structure is established within the deformed grains of the material: the cell walls consist of densely packed dislocation arrays that surround more open dislocation networks (41,48). The cells decrease in size as deformation proceeds, resulting in increasing resistance to deformation. The strain hardening is further augmented by the generation of fresh dislocations that get entangled within the existing cell walls.

It has been observed that if such a cold worked structure is submitted to a high temperature recovery anneal, the cell structure gradually polygonizes and is converted to a collection of subgrains (48,49). Polygonization or rearrangement into low angle boundaries is believed to be the result of thermally activated climb, glide and cross-glide of dislocations. Recovery is more pronounced with an increase in time or temperature and the application of a small stress during the restoration process greatly accelerates it (49). Further annealing leads to recrystallization. However, it is not known whether the recrystallization nuclei form by coalescence or by sub-boundary migration (49).

If one now considers high temperature deformation, it appears that the above phenomena should take place concurrently, with possible interactions between the various aspects of strain hardening and dynamic softening. In the case of high temperature creep, it has been shown that dynamic recovery is the mechanism by which the strain hardening is reduced (40). In hot working, however, whether dynamic recovery or dynamic recrystallization plays the more important role seems to depend on the material tested (31). This aspect of hot working has been discussed by various investigators (8,11,12,14,21,28,29,31). In the following description of substructure formation, those metals which soften by dynamic recovery alone, as well as those for which dynamic recovery is followed by dynamic recrystallization will both be considered.

#### 1.5.1 Steady state microstructure during creep and hot working

Upon initial straining, the dislocations are arranged into a cellular structure somewhat similar to that present in cold worked metals. However, due to the ease of thermal activation, climb and cross-slip now

operate and significant substructural changes occur throughout transient creep (47). In hot working, this corresponds to that region of the flow curve where the stress rises abruptly with strain.

## A. <u>Subgrain formation</u>

The initial cellular pattern is gradually replaced by roughly formed subgrains. As deformation proceeds, the sub-boundaries become better defined and more tightly knit (47). The dislocations have a high degree of mobility, and some sub-boundary migration probably takes place by glide and climb in order to develop a subgrain structure (50). By the time strains of 0.01 to 0.1 and 0.2 to 0.3 are reached, in the case of creep (40) and of hot working (26,27,31), respectively, the subgrain structure is fully developed. This corresponds to the establishment of the steady state for both creep and hot working. It appears that such a structure forms during creep whenever dislocation climb is rate controlling.

At the onset of the steady state, the structure of hot worked metals superficially resembles that of cold worked metals. The grains are elongated in the direction of working and appear "fibrous". However, the fibrous grains have been shown to be made up of subgrains similar to those resulting from creep (24,28-31,35). In the following discussion, the main features of such a substructure will be considered with regard to the three main characteristics that can be used to describe it, namely the mean subgrain size, the average misorientation across the sub-boundaries and finally the dislocation density within the subgrains.

#### B. Subgrain size

In steady state creep, the subgrains that develop during primary creep have been observed to remain equiaxed and constant in size with increasing strain (40,42,47,51). In view of the fact that, even at high strains, subgrain size and shape remain fixed, it can be concluded that the substructure is in a dynamic state, and that local changes in structure continually occur in the process of deformation. It has been clearly established that the mean subgrain size is solely a function of stress (40,42) and is independent of temperature (52,53), strain (52,53) and of grain size (54). In other words, if the stress is kept constant and any one of the other three variables is changed, the subgrain size is not altered. Some authors prefer to correlate the subgrain size with  $\sigma/G(52)$ , where G is the shear modulus of the material. The subgrain diameter has been found to increase linearly with  $(\sigma/G)^{-1}$  according to the relation (47):

$$\frac{\overline{d}}{b} = 20 \left(\frac{\sigma}{G}\right)^{-1} \tag{1-11}$$

where b is the burgers vector.

Similar observations can be made in the case of hot working. The subgrains remain approximately constant in size throughout steady state deformation (8-11,14,31). The subgrain diameter increases with temperature at constant strain rate (3,5,10,11,13,22,24,27) and with decreasing strain rate at constant temperature (3,4,20,21,26,27). It depends only on the stress (11), since the structure term  $A_3$ =Z/exp  $(\beta\sigma)$  is a function of stress alone. A linear relationship has actually been shown to hold between the reciprocal of the subgrain diameter and the logarithm of the Zener-Hollomon parameter (20,27,29,31). When an annealed metal is deformed at a given value of Z, the subgrain size is independent of the

actual temperature or strain rate involved and is always the same for identical stress levels (20,26,27,29). If an initial substructure is present, that is, if the material has not been annealed prior to deformation, the subgrain size which results is the same as that produced in the initially annealed material (31). As in creep, the initial grain size does not seem to have an effect on the steady state flow stress and on the subgrain size (13). At homologous temperatures in the range from 0.3 to 0.6, it has been observed that, while at low strain rates the subgrains are equiaxed, they appear somewhat elongated at higher strain rates (20,22). However, at homologous temperatures above 0.6 the subgrains are always equiaxed, even after very large strains (20,22,24,47). Insofar as subgrain size is concerned, hot working behaviour is similar to creep behaviour. The continuity of flow stress-subgrain size relationships means that smaller subgrains are generated in hot working than in creep, since higher flow stresses are involved.

# C. Subgrain misorientation and the nature of the sub-boundaries

The subgrain boundaries that have been observed during secondary or steady state creep consist of well formed tilt boundaries, regular hexagonal networks and irregular networks made up of mixed edge-screw dislocations (47,51). Recently, extensive work (50,55) was carried out in order to determine the nature of the sub-boundaries formed during the creep of molybdenum and copper single crystals. Most of the sub-boundaries observed by electron microscopy were simply tilt boundaries. Since the proposed mechanism for substructure formation (50,55) appears to be based on the interaction of several slip systems, it has been suggested (47) that the formation of the substructure is not solely the result of simple

polygonization, but is also affected by sub-boundary coalescence during the course of creep. However, the ultimate formation of subgrains is not yet fully understood.

With regard to subgrain misorientation, early investigations tended to support the view that the misorientation,  $\theta$ , between neighbouring subgrains, was directly proportional to the strain (56). However, this conclusion was reached through the study by means of polarized light microscopy of anodized aluminum, a technique which has since been found to be misleading (22,35,57). X-ray microbeam techniques have also been used to study the misorientation between subgrains. They also support the increase in  $\theta$  with strain, but these findings are inconclusive (47).

In hot working, more systematic studies of subgrain misorientation have been carried out by means of electron microscopy (22,26,27), a technique which has been shown to be more reliable than the other methods discussed above. It appears that, to a first order, the misorientation does not vary with strain. Misorientations of only a few degrees are observed even after true strains of  $4^{(22,24,26,27,28)}$ . In Armco iron and silicon steel, the misorientations between subgrains were in the range  $<1^{\circ}$  to  $\sim7^{\circ}$ , but no systematic variation with strain, strain rate, temperature or flow stress was observed (26,27,31). It appears from these observations that a limiting subgrain misorientation exists in high temperature deformation. This is effectively in accord with the variation of the structure term,  $A_3$ , with stress. Since  $A_3$  is a function of stress alone, it might be anticipated that the misorientation should achieve a steady state when the flow stress does.

During steady state hot working, it has been observed that the

subgrain boundaries are better defined at higher temperatures (27,29,30,35). A similar effect is observed when the strain rate is decreased. The perfection of the subgrain boundaries has been found to decrease with decrease in stacking fault energy (28,30). This is predictable, since metals with similar structures but different stacking fault width differ in the ability of the dislocations to climb out of their slip planes. If climb is rate controlling, then differences in stacking fault energy can be expected to affect both the flow stress and the structure.

## D <u>Dislocations within subgrains</u>

The dislocation density within subgrains during steady state creep has been extensively studied (47,50,58,59). The data have been found to fit the relation (47)

$$\frac{\sigma}{2} = \alpha Gb \sqrt{\rho} \tag{1-13}$$

for a wide variety of metals. Here  $\alpha$  is a constant, G is the shear modulus, b is the burgers vector and  $\rho$  is the dislocation density. It is worth noting that this relation also holds at low temperatures, in which case  $\alpha = 0.5$ . In high temperature creep by climb,  $\alpha = 0.6$ .

Regarding the character of the dislocations within the subgrains, recent investigations (50,55) have shown that, in molybdenum most dislocations are in edge orientation, an observation which favours the climb mechanism as the rate controlling process. The fact that piled up arrays of edge dislocations have never been observed after high temperature creep is not considered to refute the applicability of climb models since piled-up arrays have been shown to be unstable (J.E. Dorn, discussion, ref. 43).

Much less quantitative information is available in the case of hot working. It has been observed that increasing the temperature or decreasing the strain rate results in lower dislocation densities within the subgrains (20,28-30,35). The influence of stacking fault energy has been investigated qualitatively with regard to hot working substructures in FCC metals and it was found that the dislocation density appears to be higher in metals with low stacking fault energies (29,30). For the reasons mentioned previously with respect to subgrain size and misorientation, it is likely that the dislocation density remains constant during steady state deformation, as the structure is a function of stress alone. If these observations are reliable, then it is possible that a relation of the form

$$\rho = k(-\frac{1}{d})^{N} \tag{1-13}$$

holds between the dislocation density,  $\rho$ , and the subgrain diameter,  $\overline{d}$ , where k and N are constants. This relation should hold at low and high strain rates, and it is believed that in the creep range of strain rates N has a value between 2 and  $3^{(55)}$ . It is very probable that dislocations inside the subgrains act as sources of additional dislocation segments as they cross-slip and climb (22,55). It is probable that both grain boundaries (51) and sub-boundaries (22) also act as sources of dislocations, although in general, they are more likely to act as sinks.

#### 1.5.2 Dynamic recovery mechanisms in hot working

In view of the above observations, investigators have proposed various models to explain the structural behaviour of hot deformed metals. The steady state regime is viewed as a balance between a hardening process

and a restoration process. In creep, dynamic recovery has been shown to be, in general, the principal restoration process. Since the structural behaviour in hot working is similar to that in creep, the same restoration mechanism has been considered to be controlling in high strain rate deformation. In the model proposed by Stüwe (14), the dislocations are produced within the subgrains and are annihilated at the sub-boundaries by means of a climb controlled mechanism. The dislocations glide to the sub-boundaries, where the screw dislocations cross slip into the sub-boundaries without delay. The edge components await thermal activation for climb, the required vacancies originating in the intersection of the moving screw dislocations. According to this model, the constant level of dislocation density during steady state deformation is achieved when the rates of dislocation generation and annihilation become equal.

It should be noted that very large strains can be reached during hot working, resulting in a fibrous or "cold-worked" structure. Under these conditions, the grains are highly elongated and, as the subgrains are completely formed by the time the steady state is attained, the subgrains should elongate almost as much as the grains. Nevertheless, the substructure remains equiaxed even after very large strains. In order to account for this conflict, it has been suggested that the subboundaries migrate continuously so as to maintain the equiaxiality of the subgrains. Larger subgrains consume smaller subgrains, and the steady state is achieved when the rates of sub-boundaries generation and annilibation are equal. Although this explanation may be valid at low strain rates, at the higher strain rates encountered in hot working, there may not be sufficient time for sub-boundary migration. It has also been proposed that the sub-boundaries are continuously breaking-up and

reforming during steady state hot working (20,21). As in Stüwe's model (14), the rate of dislocation generation becomes equal to the frequency of annihilation at the onset of the steady state. The balance between hardening and recovery is maintained throughout the steady state, and explains the constant geometry of the internal structure as well as the constant level of the flow stress. The process by which the sub-boundaries disintegrate is described in the literature (20,21,28,29,30). Briefly, the stability of the sub-boundaries is decreased once they become heavily jogged by means of interaction with the mobile dislocations. The dislocations emanating from the disintegrated networks rearrange themselves into new sub-boundaries, so that an equilibrium spacing which depends on Z is maintained throughout steady state (20,21). This dynamic process of regeneration has been termed repolygonization.

#### 1.5.3 Dynamic recrystallization

As already mentioned, metals and solid solution alloys can be divided into two groups with regard to their hot working behaviour  $^{(31)}$ . The structural considerations described above apply to the first group, which includes commercial purity  $\alpha$ -iron and ferritic alloys, aluminum and aluminum alloys. For these materials, a substructure is formed at either low or high strain levels and dynamic recovery is the principal hot working mechanism. In copper and copper alloys, nickel and its alloys, austenitic steel and zone refined  $\alpha$ -iron, after small strains, an initial substructure develops within the distorted grains. However, after large deformations, these metals and alloys show an equiaxed recrystallized grain structure. For this group, the activation energies are substantially different from those for creep of the same materials (Table I).

With regard to structure, the first recrystallized grains appear at strains equivalent to the peak flow stress described earlier. The optical microstructure observed after static recrystallization is similar to that reported for dynamic recrystallization (3,8,9,12,31). The most important feature of the recrystallized grains observed in hot worked metals of the second group, however, is that they contain a substructure similar to that which develops within the initial grains before the peak flow stress is reached (10,12,28). Since the statically recrystallized grains are dislocation free, the above observations support the occurrence of dynamic recrystallization. Thorough discussions for and against dynamic recrystallization are found in the literature (15,30,31). A dynamic recrystallization mechanism has been proposed (31) in which extensive migration of grain boundaries takes place. Although the high stresses involved in high strain rate deformation should favour a recovery mechanism, it is argued that, once initiated, recrystallization can proceed at sufficiently high rates to allow for local boundary migration. Evidence for this interpretation has recently been presented for nickel and nickel alloys (12), although no formal model for dynamic recrystallization has yet been proposed.

#### 1.6 Theories of High Temperature Deformation

Various theories based on dynamic recovery have been proposed for high temperature creep. Since the structural changes taking place during creep and hot working are so similar, as outlined earlier on, it will be of interest first to survey the creep theories and then to extend them to the hot working range of strain rates. It is important to note that the proposed theories usually apply to steady state deformation,

the transient region being more difficult to investigate and to describe.

Also of importance with regard to hot working is that a viscous creep theory such as the Nabarro-Herring mechanism cannot be expected to apply at the high strain rates involved.

The theoretical work on creep has been greatly influenced by the reaction-rate theory. It was first applied by Kauzman in 1941 (quoted in ref. 40) to steady state creep. Without specifying a particular model, he derived a relation between the steady state shear strain rate  $\dot{\gamma}_s$  and the applied shear stress  $\tau$ . He assumed that  $\dot{\gamma}_s$  was directly proportional to the net number of jumps per second of "units of flow" made in the direction of shear. The derived equation reads (40):

$$\dot{\gamma}_{s} = C \exp(\frac{\Delta S}{k}) \exp(\frac{-\Delta H}{kT}) \sinh(\frac{A \ell \tau}{kT})$$
 (1-14)

where C is a temperature dependent parameter inversely proportional to the average distance between layers of flow

ΔS is the change in entropy

ΔH is the activation energy for the motion of units of flow

A is the projected area of the unit of flow on the shear plane

\$\ell\$ is the distance the shear stress acts in surmounting the potential barrier, and

A x  $\mbox{\ensuremath{\text{l}}}$  is an apparent activation volume

This equation can be rewritten as follows  $^{(31)}$ :

$$\dot{\varepsilon} = \emptyset_{f} \exp(\frac{-\Delta H_{O}}{kT}) \exp(\frac{V\sigma}{kT})$$
 (1-15)

Here, Vo has replaced the term Alτ=vτ,

V = v/M, where M is the effective Taylor orientation factor and v is the activation volume

σ is the applied normal stress

k is Boltzmann's constant, and is equal to R/N, where N is Avogadro's number

 $\Delta H_{_{\rm O}}$  is the activation enthalpy in the absence of stress, and  $\emptyset_{_{\rm f}}$  is a structure parameter.

It can be shown that for large enough values of  $\frac{V\sigma}{kT}$  (>1), the hyperbolic sine function reduces to an exponential term (11,31). It should be noted that  $\emptyset_f$  and V in Eq.(1-15) are not necessarily fixed in value (31,40). The more specific models that were subsequently derived are based on mechanisms dealing with the motion of dislocations rather than "units of flow". However, Kauzman's early proposal can still be applied. In general, the differences between the more recent models arise in the detailed interpretation of the physical terms  $\emptyset_f$  and V of Eq.(1-15). The common characteristic of all the models is that the apparent activation energy,  $\Delta H_0$ , is equal to that for self diffusion (31) (Table I). There are four basic groups of such models, and these will now be described in turn.

#### 1.6.1 Jogged screw-dislocation models

In these models, it is assumed that the rate controlling factor lies in the deformation itself. An activation energy,  $\Delta H_0$ , is required to overcome the obstacles impeding dislocation glide. These obstacles can be regarded as jogs of edge orientation, of height h burgers vectors, and spaced a mean distance  $\ell_j$  along the dislocations. When the screw dislocations glide, the jogs must climb, a process during which vacancies are created or absorbed. The vacancies must continue to diffuse to or away from the jogs for the jogged screw dislocations to keep on moving. Eq.(1-15) applies to these models, since reaction-rate theory can be

applied to slip. Various strain rate equations have been proposed in which  $^{\Delta H}_{o}$ = $^{\Delta H}_{Sd}$ , although  $^{\emptyset}_{f}$  and V differ. In the version of Hirsch and Warrington  $^{(60)}$ .

$$\emptyset_{f} = N l_{j} b^{2} z v \exp(\frac{\Delta S}{k})$$
 (1-16)

where  $\ell_j$  is the mean distance between the jogs along the dislocations

N is the density of activatable sites

b is the burgers vector

z is the coordination number

v is an atomic vibration frequency and

ΔS is the entropy of activation

Other similar relations have been proposed  $^{(61,62)}$ . In the analysis of Barrett and Nix  $^{(61)}$ , the steady state strain rate is given by:

$$\dot{\varepsilon}_{s} = C_{1} \rho_{m} \exp(\frac{-\Delta H_{0}}{kT}) \sinh(\frac{\ell_{j} b^{2} \sigma}{2kT})$$
 (1-17)

where  $C_1$  is defined in reference (61) and

 $\rho_m$  the density of mobile dislocation, has replaced the term Nl  $_j$  in Eq.(1-16).

Barrett and Nix made the assumption that  $\rho_m$  is directly proportional to  $\sigma^m$ , where m=3 for silicon iron. In their model, unit jogs are assumed, so that the activation volume V is given by  $\ell_j b^2$  instead of  $\ell_j b^2/h$  for the other models (31,62). The validity of the jogged screw dislocation models has been discussed by Jonas et al (31), Mukherjee et al (63) and Weertman (64). Jonas et al suggest (32) that some of the difficulties in interpretation can be avoided if a back stress term is included in relation (1-15), which then takes the form

$$\dot{\varepsilon} = \emptyset_{f} \exp(\frac{-\Delta H_{O}}{kT}) \exp(\frac{v(\sigma - \sigma_{B})}{kT})$$
 (1-18)

Here  $\sigma_{\mbox{\scriptsize B}}$  is a back stress attributable to the long range stress fields of the forest dislocations.

# 1.6.2 Climb models

In the second type of model, the rate controlling mechanism is assumed to be the continuous annealing which, due to the high temperatures involved, takes place concurrently with the deformation. Although the cross-slip of screw dislocations has been proposed as an important recovery mechanism, it appears that above 0.5 Tm the rate controlling process is that of climb, which eliminates the edge components of the disloca-In the model proposed by Weertman (65) and modified by Dorn (66), recovery is the result of the annihilation of dislocations of opposite These dislocations escape from piled-up arrays by climb under the action of a local stress. The rate of climb, and therefore the strain rate, is proportional to this local stress. The latter is in turn related to the applied stress by a stress concentration factor  $K \propto d^2 \sigma^2$ , where d is the mean subgrain size. In the derived equation, the stress dependence of the strain rate arises from  $\emptyset_{\mathbf{f}}$ , which is a function of stress, and from the term  $\exp(\frac{Kb^3\sigma}{kT})$  where  $Kb^3$  is an apparent activation volume. For the climb models, Eq. (1-15) can be modified to read:

$$\dot{\varepsilon}_{s} = C_{2} N d^{4} \sigma^{3} \exp(\frac{-\Delta H_{0}}{kT}) \sinh(\frac{K b^{3} \sigma}{kT})$$
 (1-19)

where  $C_2$  is a constant

- N is the density of activatable sites
- d is the mean subgrain size
- o is the applied stress

 $\Delta H_{\rm O}$  is the activation enthalpy for self diffusion, and kT has its usual significance.

At low stresses this equation reduces to (65,66)

$$\dot{\varepsilon}_{s} = Nd^{4}\sigma^{4} \tag{1-20}$$

Under hot working conditions, that is at high stresses, Eq.(1-19) becomes:

$$\dot{\varepsilon}_{s} = C_{3} N d^{3} \sigma^{2} \exp(\frac{-\Delta H_{0}}{kT}) \exp(\frac{K b^{3} \sigma}{kT})$$
 (1-21)

Here  $\mathbf{C}_3$  is proportional to the density of the arrested arrays of dislocations and the exponential term replaces the hyperbolic sine function. Most of the stress dependence arises from the exponential term, in qualitative agreement with the experimental results of many researchers.

The dislocation climb theories of steady state creep have recently been reviewed by Weertman<sup>(64)</sup>. As far as hot working theories are concerned, Stüwe's model<sup>(14)</sup>, already mentioned in section 1.5.2, falls into the general category of climb theories. The limitations of this model are discussed in reference 31.

#### 1.6.3 Network models

It is difficult to consider the above two groups of models separately, since both glide and recovery operate simultaneously in high temperature deformation. Furthermore, neither of the above models applies to transient deformation. Hence a need was felt for a different approach. If the stress is a function of strain and time, then the following relation (Bailey-Orowan equation) applies

$$d\sigma = \left(\frac{\partial \sigma}{\partial \varepsilon}\right)_{t} d\varepsilon + \left(\frac{\partial \varepsilon}{\partial t}\right)_{\varepsilon} dt \tag{1-22}$$

where the partial differentials can be identified as

h = the rate of work hardening = 
$$(\frac{\partial \sigma}{\partial \epsilon})_{t}$$
 (1-23)

$$r = the rate of recovery = \left(\frac{\partial \sigma}{\partial t}\right)_{\epsilon}$$
 (1-24)

On this basis, Bailey $^{(67)}$  and Orowan $^{(68)}$  derived the following equation for the steady state strain rate

$$\left(\frac{\mathrm{d}\varepsilon}{\mathrm{d}t}\right)_{\sigma} = \dot{\varepsilon}_{\mathrm{s}} = \frac{\mathrm{r}}{\mathrm{h}} \tag{1-25}$$

Following McLean and others  $^{(69,70)}$ , the transient strain rate can be given by

$$\dot{\hat{\epsilon}} = \dot{\hat{\epsilon}}_{0} \exp(\frac{-v(h\epsilon - rt)}{kT})$$
 (1-26)

where  $\dot{\epsilon}_{_{O}}$  is the initial strain rate in a creep test

t is the time, and

v is an activation volume.

An important feature of these models is that the barriers to dislocation motion are individual dislocation links in the three dimensional network present within the subgrains. Only a small percentage of the links contributes to the flow at any instant  $^{(70,71)}$ . Recently an interpretation of the recovery/work hardening model of creep has been presented in terms of the cooperative relationship between dislocation glide and recovery  $^{(72)}$ . In this analysis, it is shown that, although the accepted experimental technique led to predicted values of  $\dot{\varepsilon}_s$  close to the true value, the experimental estimates of r and h in  $\dot{\varepsilon}_s$  = r/h are generally invalid. This is because applied stresses rather than internal stresses have been used to date. The notion of internal stress was introduced earlier with Eq.(1-18) and will now be discussed in a separate section.

# 1.6.4 Effective stress models

It has been pointed out (31) that Eq.(1-18)

$$\dot{\varepsilon} = \emptyset_{f} \exp(\frac{-\Delta H}{kT}) \exp(\frac{V(\sigma - \sigma_{B})}{kT})$$
 (1-18)

is equivalent to Eqs.(1-25) and (1-26) with

$$\emptyset_{f} \exp(\frac{-\Delta H_{O}}{kT}) \exp(\frac{V_{O}}{kT})$$

equivalent to r in Eq.(1-25) and to  $\dot{\epsilon}_0$  in Eq.(1-26) and

$$\exp(\frac{-V\sigma_B}{kT})$$

equivalent to  $\frac{1}{h}$  and to  $\exp(\frac{-V(h\epsilon-rt)}{kT})$  respectively in Eqs.(1-25) and (1-26)

The applicability of Eq.(1-18) to high temperature deformation has been discussed by Jonas  $^{(32)}$ . Under steady state conditions he assumed that the back stress remains constant, so that Eq.(1-18) reduces to:

$$\dot{\varepsilon}_{S} = \emptyset_{f} \exp(\frac{-\Delta H_{O}}{kT}) \exp(\frac{V'\sigma}{kT})$$
 (1-27)

Here V' is an apparent activation volume equal to  $(\frac{f-1}{f})$ V, with  $f = \frac{\sigma}{\sigma_B}$  (32,34,38). Eq.(1-27) has been used to correlate creep and hot working data (32,38).

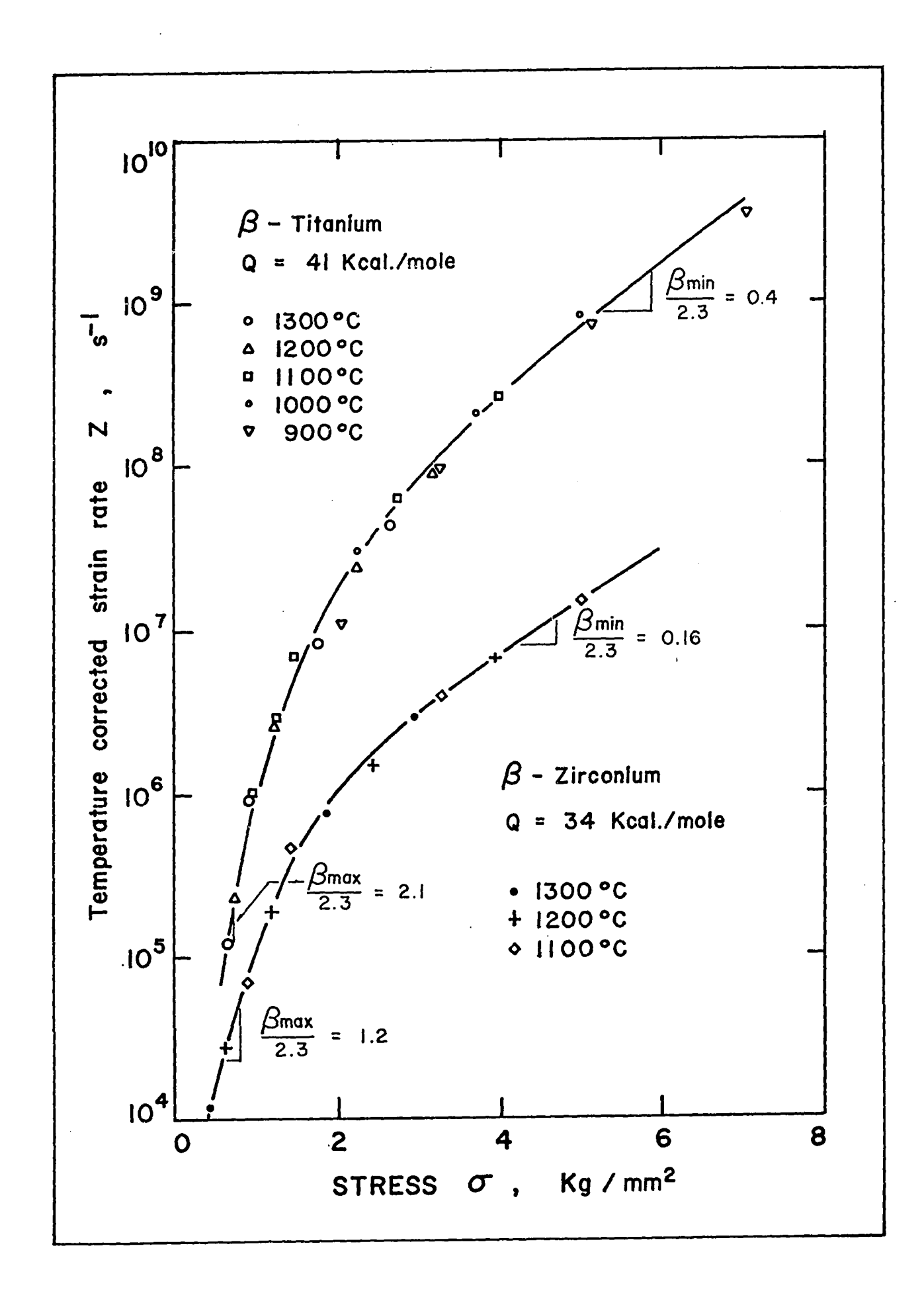
Fig.3 shows the data from Fig.1 replotted according to the relation:

$$\log Z = \log \emptyset_{f} + (\frac{\beta}{2.3} \circ)$$
 (1-28)

where  $\beta$  = V'/kT. It should be noted that  $\emptyset_f$  increases and that V'/kT decreases with increasing stress. Both of these dependences can be predicted on physical grounds:  $\emptyset_f$  is proportional to the density of activatable sites, N, or the density of mobile dislocations, both of which are considered to increase with stress. With regard to the decrease in activation volume, the physical significance varies with the three models discussed earlier: V is proportional to the jog spacing  $\ell_j$  in the jog models, to the stress concentration factor K in the climb models and to the average link length or mean network spacing,  $\ell_n$ , in the network models. Thus a decrease in V can be attributable to decrease in  $\ell_j$ , K or  $\ell_n$  respectively.

# FIGURE 3.

Variation of the Zener-Hollomon parameter Z with flow stress  $\sigma$ , illustrating the increase in  $\emptyset_f$  and decrease in V with increasing  $\sigma$ . (after Jonas and Immarigeon (38)).



An important feature of Eq.(1-27) is that it can be applied not only to steady state deformation, but also to transient deformation. The decrease in strain rate to a steady state value during constant stress creep tests, or the levelling of the flow stress to a constant value in hot working operations is then explained by the increase from zero to a constant value of an internally generated back stress:

$$\sigma_{\rm B} = h_{\rm E} - rt$$
 (1-29)

Fig.4 depicts the probable variation of the two components of the flow stress  $\sigma$  , namely the effective stress  $\sigma^*$  and the internal or back stress  $\sigma_R^*$  . The relation

$$\sigma = \sigma^* - \sigma_{\rm R} \tag{1-30}$$

holds at all strains. It can therefore be expected that upon a change in strain rate, the change in flow stress will be governed by changes in both the effective stress and the internal stress. In Fig.4, such a strain rate change is depicted. The transient region that follows is composed of two regions: one corresponding to an essentially instantaneous change in effective stress ( $\Delta\sigma$ \*) and another corresponding to a slow change in the back stress ( $\Delta\sigma$ B). These two regions will now be discussed in turn.

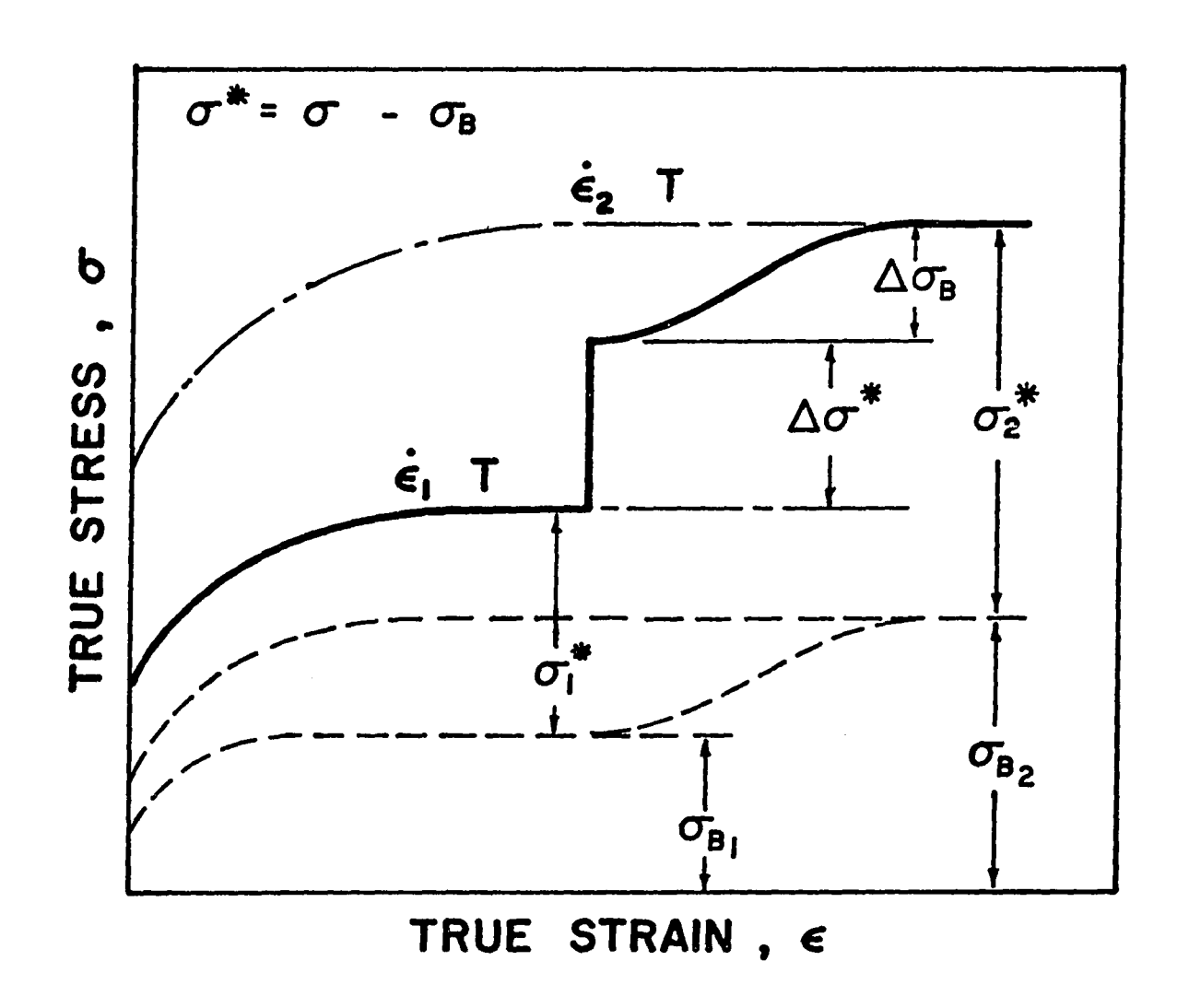
The effective stress concept is best interpreted in terms of dislocation dynamics, which gives the strain rate as:

$$\dot{\hat{\epsilon}} = \alpha b \rho_{m} \quad \bar{v} \tag{1-31}$$

Here  $\alpha$  is an orientation factor, b is the burgers vector,  $\rho_m$  is the mobile dislocation density and  $\bar{v}$  is the average dislocation velocity. From the classic work of Gilman and Johnston (73) and others, it is

FIGURE 4.

Behaviour of the internal and effective stresses following a strain rate change.



known that the average velocity of mobile dislocation can be expressed as:

$$\bar{\mathbf{v}} = \mathbf{B} \tau^{*m} = \mathbf{B}^{!} \sigma^{*m} \tag{1-32}$$

where m is a constant > 1 and B and B' are constants, with B/B' = M, the average Taylor orientation factor. Thus, from Eqs.(1-31) and (1-32):

$$\dot{\varepsilon} = B' \alpha b \rho_m \sigma^{*m} \tag{1-33}$$

Eq.(1-32) shows explicitly the high stress sensitivity of the dislocation velocity; i.e. the higher is  $\sigma^*$ , the faster will the dislocations move. Bearing in mind that  $\rho_m$  in Eq.(1-33) cannot change rapidly by large factors, if the strain rate is suddenly changed, the existing dislocations must move faster to produce the imposed deformation. This in turn requires an instantaneous change in the effective stress, as indicated by Eq.(1-33) and Fig.4.

With regard to the slow changes that take place subsequently, the following explanation can be given: when the temperature-corrected strain rate is changed from  $\mathbf{Z}_1$  to  $\mathbf{Z}_2$ , the existing steady state structure  $\emptyset_{\mathbf{f}_1} = \mathbf{f}(\mathbf{Z}_1)$  does not correspond to the structure  $\emptyset_{\mathbf{f}_2} = \mathbf{f}(\mathbf{Z}_2)$  which is stable under the new conditions. However, the internal structure cannot change instantaneously, as it is influenced by the appropriate recovery kinetics. The second part of the flow stress transient can thus be regarded as corresponding to the attempt of the material to attain a stable structure suitable to the new value of the Zener-Hollomon parameter. In the present investigation, the gradual change in the flow stress is considered to be due to slow changes in the back stress

$$\sigma_{R} = \sigma - \sigma^{*} \tag{1-34}$$

where the effective stress remains approximately constant at constant strain rate.

Whether these changes are due mainly to the change in the dislocation density within the subgrains,  $\rho$ , or to the change in mean subgrain size,  $\bar{d}$ , is still a matter of conjecture, since the back stress can be associated with either the network of dislocations within the subgrains or with the sub-boundaries themselves. The back stress has been related to the two structural variables  $\bar{d}$  and  $\rho$  by the equations:

$$\sigma_{\rm B} = \frac{\sigma_{\rm S}}{f} = \frac{2\alpha}{f} \, \text{Gb} \, \sqrt{\rho} \tag{1-35}$$

$$\sigma_{\rm B} = \frac{\sigma_{\rm S}}{f} = \frac{k}{f} \left(\frac{1}{d}\right)^{\rm m} \tag{1-36}$$

Here G is the shear modulus and  $\alpha$ , k and M are constants, M being in the range from 3/4 to 1. Since  $\rho$  and  $\bar{d}$  vary together, it is difficult to determine which feature of the substructure is the source of the back stress<sup>(32)</sup>. The present work and other similar investigations should help clarify this point.

#### Chapter 2

#### EXPERIMENTAL MATERIALS AND APPARATUS

# 2.1 Experimental Materials

Two different ferrous materials which were used in a previous investigation were examined in the present study. Their origins are given below:

- Armco iron with increased manganese, supplied by the Armco Steel Corporation, Middletown, Ohio.
- 2.7% silicon steel, supplied by the Allegheny-Ludlum Steel Corporation, Dunkirk, New York.

The chemical compositions of these materials are given in Table II.

#### 2.2 Specimen Preparation

Compression cylinders were prepared from the available rods by machining, as outlined in Table III. In order to minimize the possible effect of different initial structures, the samples were strain-annealed, the resulting mean grain size being 0.5 mm in silicon steel and 0.1 mm in Armco iron. In the latter case, grain growth usually occurred near the surface. The strain-anneal sequence was optimized in order to minimize this effect, and is listed in Table III.

## 2.2.1 Machining

A standard lathe was used for turning and facing the cylinders. The dimensions are shown in Table III. The end faces were grooved (25,74)

TABLE II

CHEMICAL COMPOSITION (WEIGHT PERCENT) OF THE MATERIALS TESTED\*

Element	Armco iron (increased Mn)	Silicon steel
С	0.03	0.03
P	0.005	0.008
S	0.01	0.02
Mn	0.26	0.39
Si	0.15	2.70
Cu	0.13	0.07
Cr	0.01	0.02
Ni	0.05	0.05
A1	0.00	0.06
N	0.007	0.010

<sup>\*</sup> Suppliers' analyses.

in order to retain the glass lubricant used in high temperature compression (see section 2-4). For this purpose a 56 tooth/inch standard thread chaser was used. The thread chaser was modified by grinding off the top 0.006 inch of the teeth, in order to produce flat-bottomed grooves. (see Fig.5 for actual dimensions of the grooves.)

## 2.2.2 Strain-annealing

All annealing operations were performed in a Lindberg Hevi-duty high temperature furnace fitted with automatic temperature control (time-proportioning type). In order to prevent oxidation, the annealing was carried out under a controlled atmosphere in a high temperature Inconel retort. The retort was supplied by the Lindberg Co. to fit the existing furnace. For the annealing operations, the samples were first degreased carefully in carbon tetrachloride, rinsed in methanol and dried. The cylinders were then placed into ceramic boats and introduced into the retort chamber. The retort was evacuated and flushed with argon at least three times before being brought to temperature. The annealing temperature was reached in only 15 to 20 minutes, as the retort was placed directly into the hot furnace. Cooling was performed either by shutting off the furnace or by retracting the retort and having it air cooled, depending on the material involved (see Table III). All the above operations were performed under a constant flow of high purity argon. The temperatures within the retort were measured by means of a movable chromel-alumel thermocouple encased in a Mullite closed-end tube. Oxide-free, shiny surfaces resulted from all these operations, even after an annealing treatment of 100 hours at 850°C for the Armco iron.

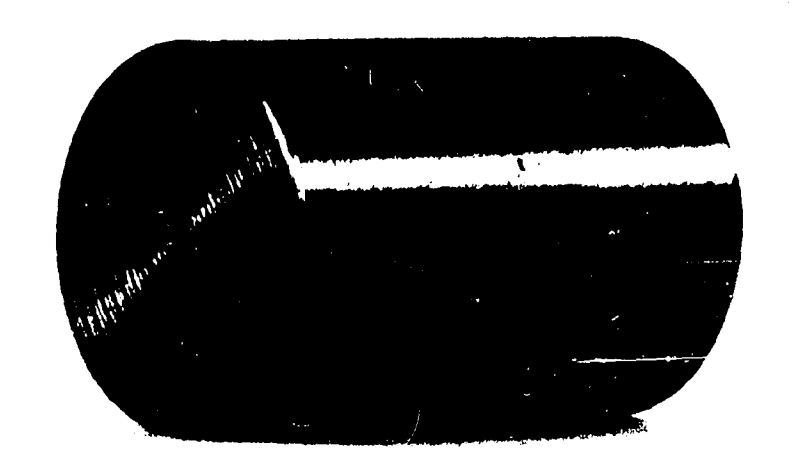
Straining by compression was performed in a standard Instron

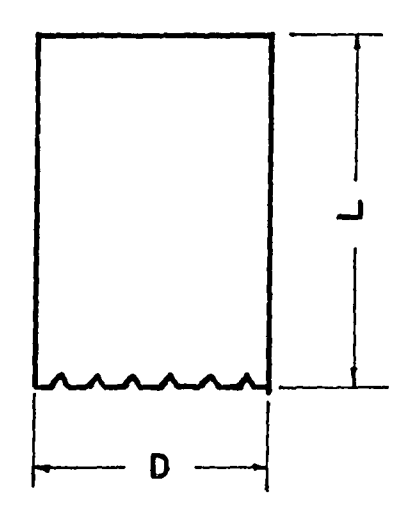
TABLE III
SPECIMEN FREPARATION PROCEDURE

Operation		Armco iron	Silicon steel
Turning	Dia.(in)	0.400	0.377
Facing	Length(in)	0.622	0.628
Grooving faces	see Fig.5		
Pre-annealing	T <sup>O</sup> C time(hr) cooling	950 7 air quench	1100 2 air quench
Straining		0.035	0.08
Strain-annealing	T <sup>O</sup> C time(hr) cooling	850 100 50°C/hr	1020 10 air quench

FIGURE 5.

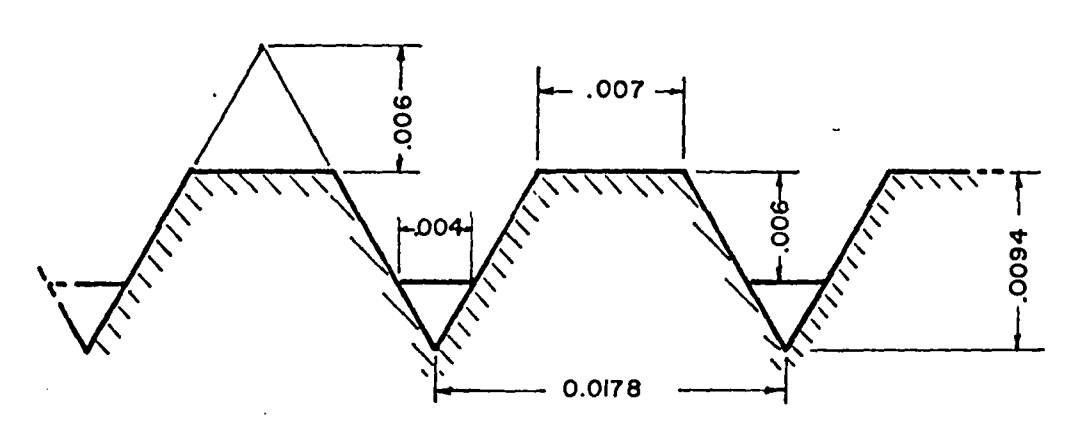
Specimen and modified thread chaser geometry





Dimension in in.	L	D
Armco iron	0.600	0.406
Silicon steel	0.580	0.393

Depth of grooves (in.)	0.006
Spacing of grooves (in.)	0.0178



Details of thread chaser

testing machine between two polished platens. A layer of teflon tape (PTFE tape) was placed at each end of the specimens to act as a lubricant. No barrelling was observed, and the grooves were not damaged because of the small strains involved. A second anneal followed the straining, as indicated in Table III.

# 2.3 High Temperature Compression Machine

There are various methods available for evaluation of the mechanical behaviour of metals under hot working conditions. Scaled-down practical working operation can be used, but the results are not easily interpretable and do not allow, in general, a comprehensive study of the parameters of hot working  $^{(75)}$ . In addition to scaled-down processes, three basic test methods can be employed, namely tensile, compression and torsion testing, and these have been discussed by various investigators  $^{(30,42,75)}$ . The decisive factor in the present investigation was the availability of the compression equipment. This was based on a standard 20,000 lb. Instron testing machine after the following major modifications were carried out:

- A constant true strain rate device was constructed which produced a continuous logarithmic decrease of the crosshead speed.
- (2) An environmental chamber was designed and assembled which permitted testing to be carried out over a wide range of constant temperatures.
- (3) A gas purification train was devised to allow the testing to be performed within a controlled atmosphere.
- (4) The compression train was designed so that the samples

could be quenched fairly rapidly after the compression cycle was completed.

The above modifications were constructed in conjunction with M.J. Luton, who designed the essential features of the compression train. The present author was responsible for item 3 above and also contributed to the construction of items 1 and 2. For the sake of completeness, the entire apparatus will now be described.

## 2.3.1 Description of the modified Instron compression machine

Fig.6 shows the overall arrangement of the accessories around and within the existing Instron frame. Fig.7 shows the detailed arrangements within the furnace. Basically, the machine consists of a split furnace that can be opened and pushed away on its supporting rolling cart for ease of specimen insertion. An Inconel sheath, within which a vacuum of  $10^{-2}$  mm Hg can be drawn, surrounds the compression ram and anvil. The latter are made of superalloys (Udimet 500, Udimet 700 and René 41) in order to minimize deformation of the machine under high stresses at high temperatures.

The ram and the anvil are water cooled at their top and bottom ends respectively. Further water cooling is provided at each end of the Inconel sheath and around the sheath support plate. The sheath can be raised and lowered for specimen insertion. At the highest crosshead speed (20 in/min) this takes approximately 30 seconds.

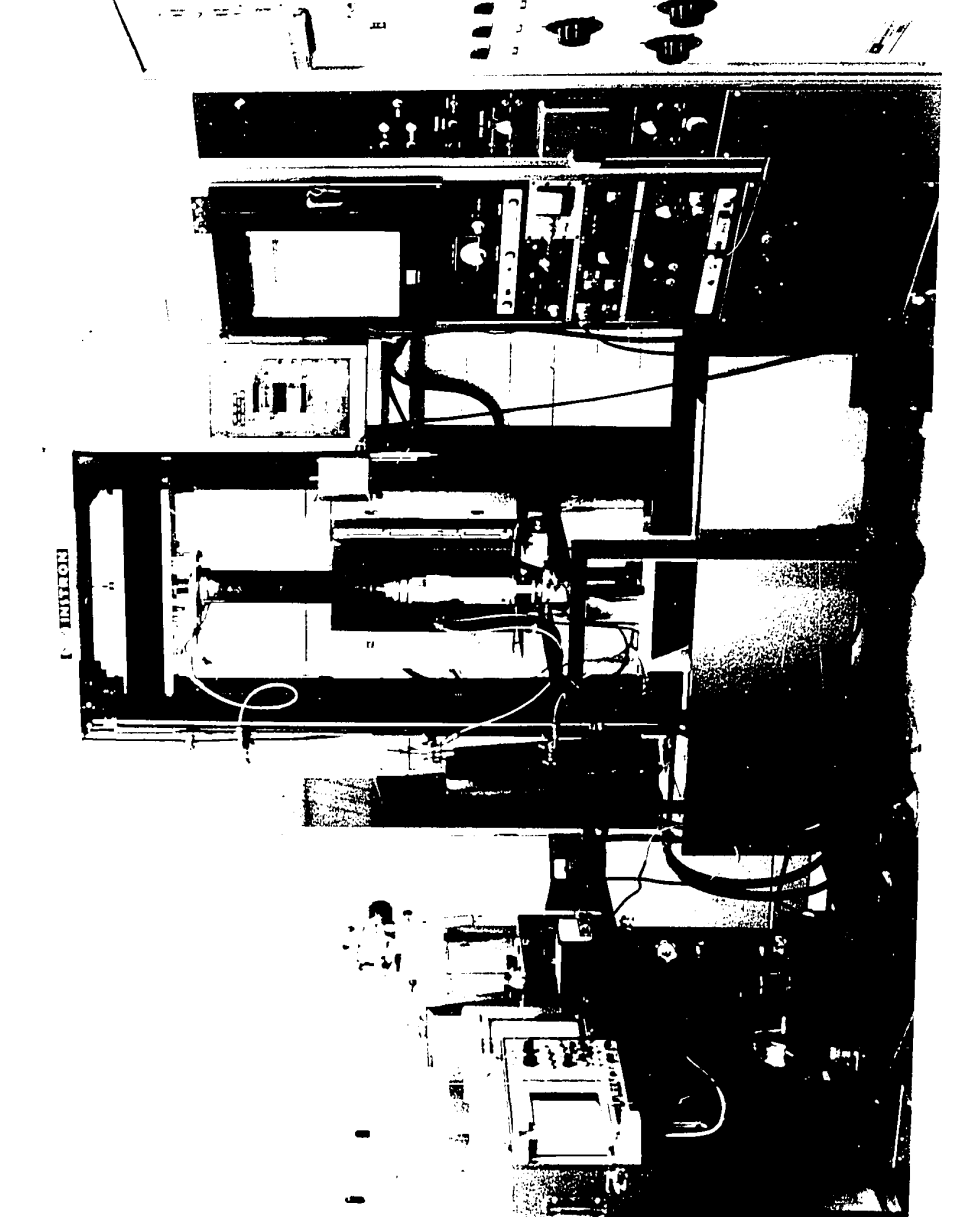
#### A. Quenching device

Quenching is accomplished in the following manner. The existing

Instron controller has an automatic return mechanism which is actuated

FIGURE 6.

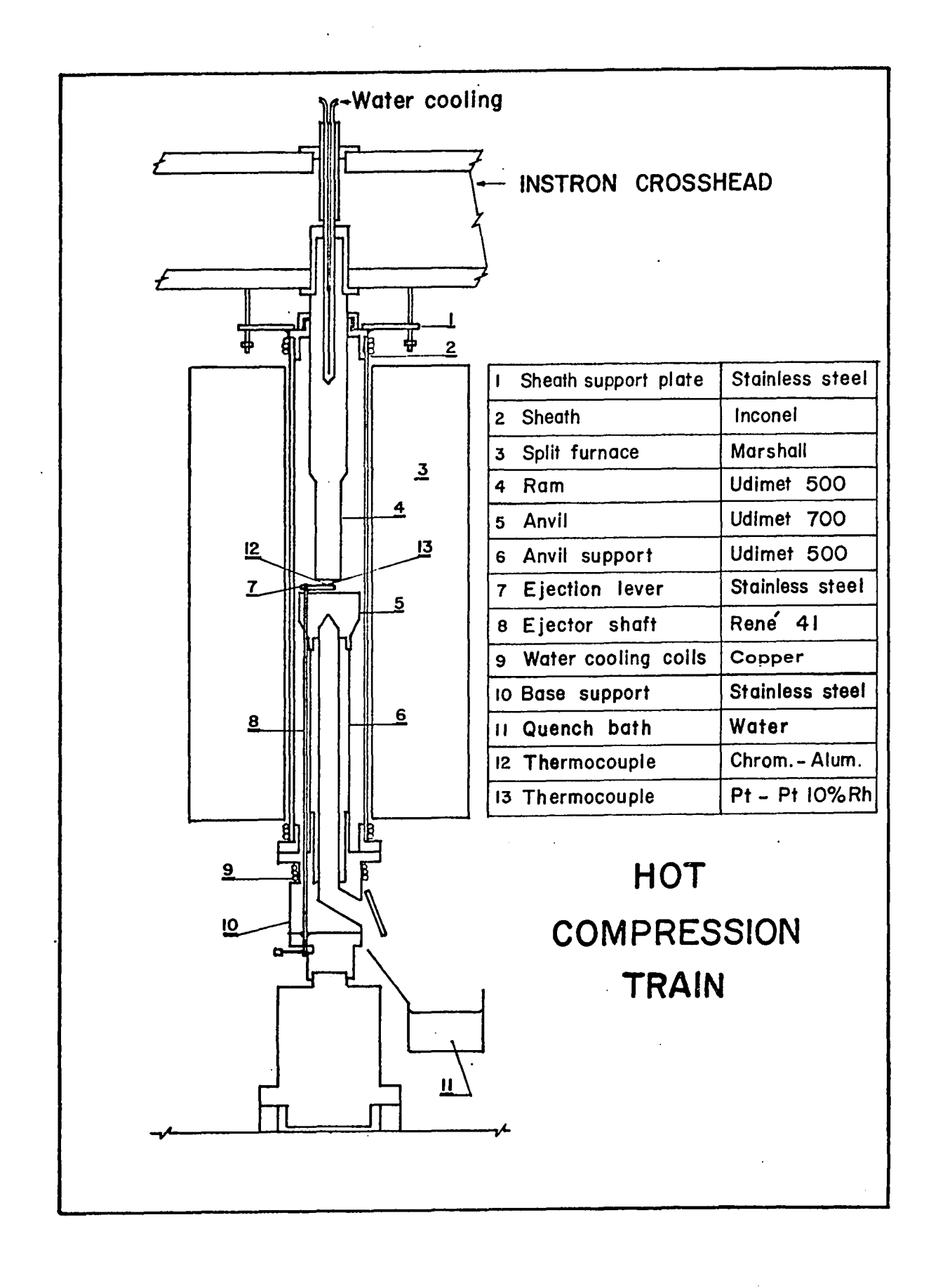
General layout of the equipment



A CHARLEST COURSE SHARE & .

# FIGURE 7.

Cross-section of the hot compression train



through a crosshead position detector. Upon completion of a test, the ram is rapidly raised by the return mechanism, removing the load. This permits a hand-actuated lever to push the compressed sample down the chute, through the vacuum trap and into the cold water bath. These features of the compression train are shown in Fig.7. With the aid of this equipment, quenching times never exceeded 2 seconds.

## B. Temperature control

A temperature of 675°C, used for all the tests in the present investigation, was produced by means of a Marshall (Norton), three-zone, split furnace with a maximum temperature of 1200°C. Temperature control was provided through a current-proportioning SCR Marshall console, operating on either the middle or the end zones. The controller was modified so that the temperature was actually controlled from within the Inconel sheath at a point between the two compression platens. The platinum-platinum 10% rhodium control thermocouple, and a chromel-alumel reference thermocouple were led out of the testing chamber through a vacuum-tight fitting sealed with epoxy. Opening the furnace and raising the outside sheath to insert a specimen usually resulted in a 200°C drop. A further 20 minutes were then required for the temperature to stabilize at the testing temperature, which was maintained constant within ±1-2°C. To facilitate the return to the set point, an approach control circuit was added to the controller.

#### C. Atmosphere control

To prevent the samples from being oxidized during the course of a test, a gas purification train was built, which was also used for

evacuation of the testing chamber (Fig. 8). A vacuum of about  $10^{-2}$  torr was reached within the system by means of a mechanical, two-stage pump of 75 liters/min. capacity. During a test, a positive gauge pressure and a constant flow of argon were maintained through the system.

The gas purification train was based on one described by Maak and Sellars (76). It was designed to remove oxygen, hydrogen, carbon monoxide, carbon dioxide and hydrocarbons from inert gases by means of Cu and Cu<sub>2</sub>0 granules. These were supplied by BASF Chemicals Ltd., under the name of BTS pellets. In the present case, four towers about 4 cm in diameter and 50 cm long were filled respectively with Linde molecular sieve type 13X, BTS pellets in their reduced state (Cu), BTS pellets in their oxidized state (Cu<sub>2</sub>0), and again type 13X Linde molecular sieve. Heating, as required for the BTS pellets, was provided by means of Kanthal wire wound around the pyrex towers and held in place by Kimax cement. Temperature control was achieved by means of two Variac auto-transformers. Glass wool was used around the towers as insulation. The argon circulated through the gas train, through the compression chamber and finally through an oil trap to atmosphere. The oil trap prevented back diffusion into the system.

#### 2.3.2 Strain rate controller and load detector

The provision of a constant true strain rate was probably the most important experimental condition required for the present experiments. This requirement meant that the crosshead velocity had to be varied in proportion to the instantaneous height of the specimen. The relation between this height and the crosshead velocity will now be described.

FIGURE 8.

Gas purification train



In axysimmetric compression, the true strain undergone by a cylindrical specimen is given by:

$$\varepsilon = -\int_{h_0}^{h} \frac{dh}{h} = -\ln \frac{h_0}{h}$$
 (2-1)

where  $h_0$  is the initial height of the cylinder and h is the instantaneous height.

Differentiation with respect to time leads to:

$$\dot{\varepsilon} = \frac{d\varepsilon}{dt} = \frac{d\ln h}{dt} \tag{2-2}$$

or  $\dot{\varepsilon} = \frac{1}{h} \frac{dh}{dt}$  (2-3)

Under constant strain rate conditions,  $\dot{\varepsilon} = \dot{\varepsilon}_{c}$ 

Hence 
$$\dot{\varepsilon}_{\rm c} = \frac{1}{\rm h} \frac{\rm dh}{\rm dt} \tag{2-4}$$

and 
$$\dot{\varepsilon}_{c}h = \frac{dh}{dt}$$
 (2-5)

But  $\frac{dh}{dt} = V$ , the crosshead velocity.

Therefore 
$$V = \dot{\epsilon}_{c}h$$
 (2-6)

A constant true strain rate will therefore be produced if Eq.(2-6) is obeyed at all times during compression.

For  $\dot{\epsilon}$  to remain constant, the crosshead velocity V, must decrease linearly with h. How this condition was achieved is described in the following paragraph.

To begin with, the standard Instron controller was equipped with the Instron variable speed control unit. With this unit, the velocity of the crosshead can be varied simply by turning a potentiometer having a linear signal/crosshead velocity characteristic. Taking the crosshead position during compression as representative of the instantaneous height, the following closed loop system was built, which resulted in a uniform logarithmic strain rate.

A linear potentiometer\* was mounted on the Instron frame and connected to the crosshead through a 1:3 gear ratio. A circuit was prepared and included in the Instron console which amplifies the signal from the potentiometer and permits calibration for different specimen heights. This signal is fed into the existing variable speed control. With the aid of the system described, the crosshead velocity could be varied as required from its full value to nearly an order of magnitude less. To eliminate possible errors due to thermal expansion of the compression machine, an offset calibration was provided in the circuit. Furthermore, a load detection device was prepared which switches in the variable speed unit only when the anvil contacts the specimen. Circuit diagrams for the above devices are shown in Fig.9.

## 2.3.3 Load and strain recording

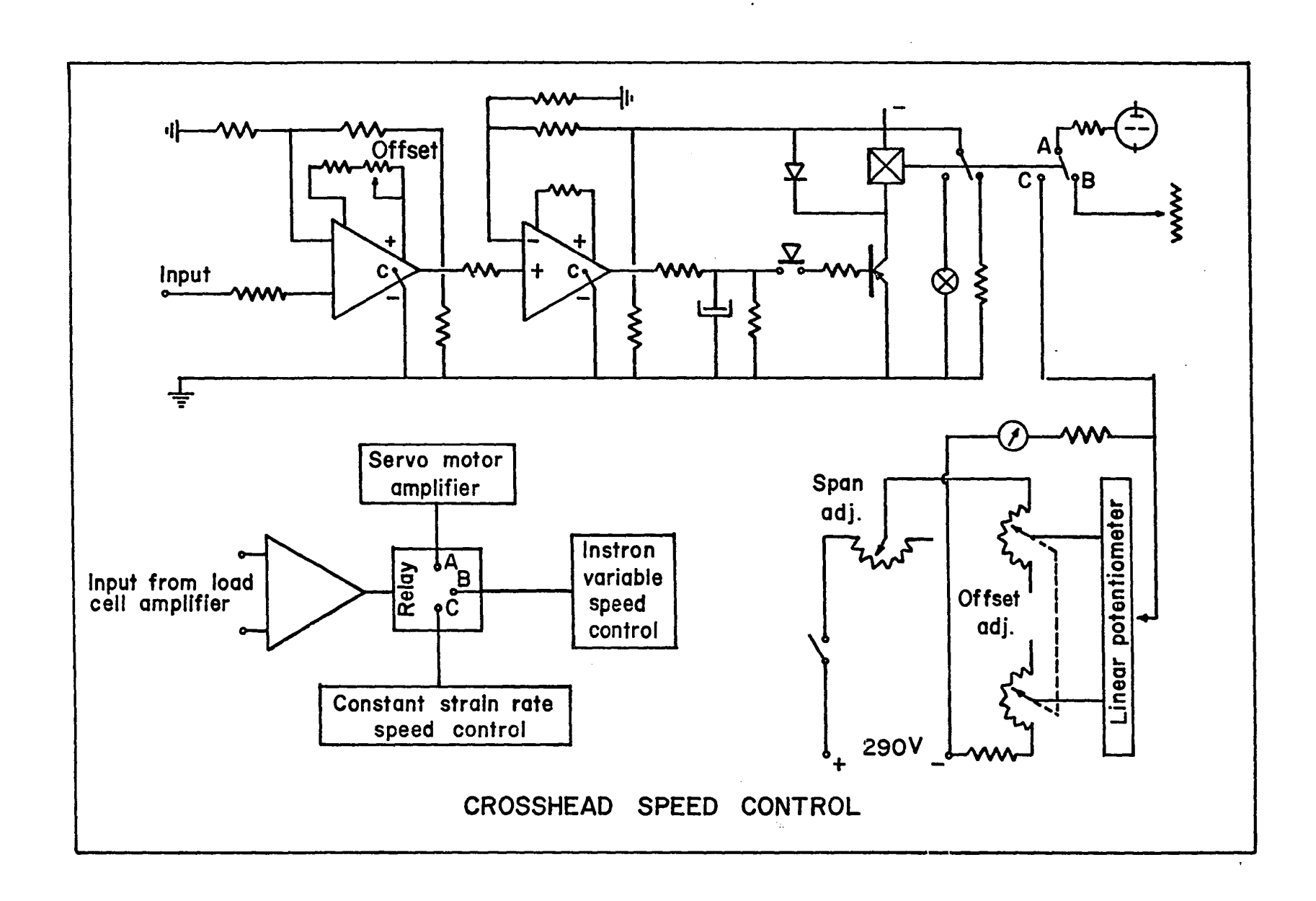
The standard Instron GR load cell was modified in order to accept and support the bottom part of the compression device. Water cooling was provided at the junction between the load cell and the compression rig.

With regard to strain measurements, the crosshead position was taken, as a first approximation, to represent the instantaneous specimen height. A simple mechanical device was fitted to the moving crosshead and connected for reference to the fixed frame. The displacement of the moving parts with respect to fixed parts was recorded by means of a 2 inch

<sup>\*</sup> Supplied by Pacific Scientific Co., Los Angeles, Model RP04-0101-1

FIGURE 9

Circuit diagrams for the constant strain rate device and the load detector



Instron strain gauge extensometer. Provisions were made in the design so that the crosshead could be raised completely for specimen insertion without having to remove the strain gauge extensometer. The amplified signals from both the load cell and the extensometer were used to drive the pens of a two-pen recorder mounted in the Instron control console.

### 2.3.4 Experimental range of the equipment

The Instron modified as described above enabled compression tests to be performed at temperatures up to  $925^{\circ}C$  and at any crosshead velocity in the range from 20 in/min to 0.002 in/min. This corresponds to strain rates of  $5.5 \times 10^{-1}$  s<sup>-1</sup> and  $5.5 \times 10^{-5}$  s<sup>-1</sup> for an initial specimen height of 0.6 in. One limitation must be mentioned. At velocities above 2 in/min., the maximum force capability is limited to 5,000 lb., although the Instron model TT-D is classified as a 20,000 lb. machine at lower velocities.

As described earlier, constant true strain rates were produced by means of the special closed loop control system. Instantaneous changes in strain rate were initiated by means of the Instron magnetic clutch and 10:1 gearbox in series with an additional decade speed reducer. Thus almost instantaneous strain rate changes of two orders of magnitude were produced. In order to avoid consuming wasteful amounts of recording paper and to facilitate the scaling off of data points, an instantaneous paper speed changer, an Instron accessory, was added to the existing twopen recorder. In the experiments, strains were limited to  $\varepsilon \simeq 1$  because of the maximum load limitations of the machine, and because, at high deformations, folding over of the edges of the sample became noticeable. The maximum size of the sample in the present device was limited by the

inside diameter of the tubular chute (0.8 in.) in the quenching device.

## 2.4 High Temperature Lubricants

In order to decrease the effect of friction and barrelling, powdered glass lubricants were used, as suggested by previous investigators (25,39,74). Successful lubrication is achieved when the glass has a viscosity of  $10^{-4}$  poises at the temperature of operation (39). Various glass compositions were tested and the following composition recommended by Uvira (25) was used:

TABLE IV

GLASS LUBRICANT FOR HIGH TEMPERATURE DEFORMATION

Compound	B <sub>2</sub> O <sub>3</sub>	РЪО	Window glass
Weight percent	15	75	10

The glasses were prepared by grinding the various components to a -200 mesh size, mixing them thoroughly, and melting the mixture to insure homogeneity. The melt was then water quenched and reground to a -200 mesh size. The following technique was used in order to coat the end faces of the compression cylinders with the powdered glass. A suspension of the glass in acetone was prepared, and the mixture was deposited on the end faces of the specimens by means of a small brush. Coating of the sides of the specimen, to prevent oxidation, was made a regular practice. Upon insertion of the specimen in the hot chamber, a viscous film was produced, which prevented oxidation until a vacuum could be drawn within the enclosure.

#### Chapter 3

#### EXPERIMENTAL PROCEDURE

### 3.1 Testing Procedure

Prior to a test, the compression chamber was brought to temperature (675°C) and calibration procedures for the variable speed unit and the constant strain rate device were performed. Then the furnace was retracted, the Inconel sheath raised, and the glass coated sample inserted between the compression platens. Some talcum powder was sprayed, by means of a wash bottle, down the quenching chute in order to prevent sticking of the sample. The above sequence was then reversed, the whole operation usually requiring less than 1 minute. The compression chamber was next evacuated and purged with argon at least three times, before a constant flow of inert gas was established through the enclosure. Tests were started fifteen minutes after the temperature had again stabilized at the set point. In tests requiring a strain rate change, the paper speed of the load-contraction recorder was changed simultaneously with the strain rate. Quenching was performed within one to two seconds of the end of a test.

The experiments performed on the Armco iron and on the silicon steel were of three types:

a) Specimens were deformed into the steady state at strain rates of  $10^{-3} \, \mathrm{s}^{-1}$  and  $10^{-1} \, \mathrm{s}^{-1}$ , corresponding to initial maximum crosshead velocities of 0.0333 in/min and 3.33 in/min respectively. The maximum steady state strains reached were

lower at the higher speed because of the load limitation of the machine.

- b) Specimens were deformed into one of the above steady state regions, after which a sudden strain rate change was initiated. Straining was carried to the point where the steady state stress corresponding to the second strain rate was established. Experiments were performed for strain rate changes from  $10^{-3} \, \mathrm{s}^{-1}$  to  $10^{-1} \, \mathrm{s}^{-1}$  and vice versa.
- c) Specimens were deformed as in b) above, but in this case
  the samples were quenched at various increasing values of
  strain after the strain rate change.

The purpose of the last sequence of experiments was to "freeze" the transient substructure, so that the changes between the two steady state conditions could be followed by means of electron microscopy.

### 3.2 Measurement of the Deformation Variables

Three deformation variables, namely load, strain and temperature were recorded for each compression cycle.

- 1) The loads were recorded with respect to time on the Instron 10 in.

  chart paper running at constant speeds of 50 in/min at the high strain

  rate and 5 in/min at the low strain rate.
- 2) The axial contractions were recorded on the same chart, with the strain pen running ahead in time and in the direction opposite to that of the load pen.
- 3) The temperature was controlled by means of the thermocouple described earlier and was also checked using a separate thermocouple and a Leeds and Northrup model 8690 millivolt potentiometer. In between

manual verification periods, the supplementary temperature reading was registered on a Leeds and Northrup Speedomax H recorder.

## 3.3 Calculation of True Stress and True Strain

The true stress  $\sigma$  was calculated from the measured uniaxial force F using the relation:

$$\sigma = \frac{F}{A} \tag{3-1}$$

Here A is the instantaneous cross sectional area of the compressed cylinder, which is related to the initial cross sectional area of the specimen, A, by the relation:

$$A = A_0 \frac{h_0}{h}$$
 (3-2)

where h and h are the initial and instantaneous height of the specimen. It should be noted that the recorded loads include a contribution due to friction and barrelling and therefore appear larger than in the case of frictionless, homogeneous deformation. The sources of error will be discussed later.

The true strain was derived from the axial contractions and Eq. (2-1)

$$\varepsilon = -\ln \frac{h_0}{h} \tag{2-1}$$

Again, the recorded contraction does not represent the true deformation, since the strain gauge extensometer also records the elastic compression of the machine, and the high temperature compression train is not a "hard" machine. Not only do the lengths of the ram and anvil vary with stress, but they also vary with temperature. The corrections applied will be described later.

A computer program was prepared, which converts the loads and contractions read off the graphs into true stress and true strain, both with and without corrections. The program also verifies that the experimental strain rate corresponds to the desired true strain rate.

## 3.4 Preparation of Specimens for Optical Metallography

Optical metallography was performed on annealed, undeformed samples in order to check the grain size. The cylinders were sectioned by spark machining (see section 3.5.1) and mounted in bakelite along planes either containing the compression axis or perpendicular to it. Mechanical polishing was performed as described in section 3.5.2 below. Final polishing was performed on two Selsyt wheels coated with 9 and .5 µm diamond paste. The samples were then degreased in acetone, washed in methanol and dried. The grain structure was revealed by chemical etching in a 1% nital solution. However, apart from the grain size check, no optical metallography was performed. Instead, the hot-worked substructures were studied by means of transmission electron microscopy.

# 3.5 Preparation of Specimens for Electron Microscopy

#### 3.5.1 Sectioning of specimens

The compressed cylinders were cut along planes containing the compression axis by means of an SMD Servomet spark machine. A Servomet accessory, the spark slicer, was used for this purpose, and relatively undamaged plates 0.8 mm in thickness were prepared. The adhering glass, which coated the compressed cylinders, was removed by carefully filing down the side walls of the specimens. This improved the electrical contact required for machining. SWG 28 tinned copper wire was used in the

spark slicer. In general, the cutting of a slice required four to six hours. At least two slices were cut from each sample.

In the spark machining process, a series of spark discharges of controlled energy is produced between the wire and the bottom of the cut in the specimen. Erosion occurs by melting close to the sparks. The rate of removal by vaporization and ejection of the liquid metal is controlled by the energy and frequency of the discharges. As the dielectric break-down voltage V is proportional to the work gap, that is to distance between the tool and the specimen, V can be used to control a servo-system which maintains the work gap D at its optimum value. Range 5 on the SMD was used for all cuts.

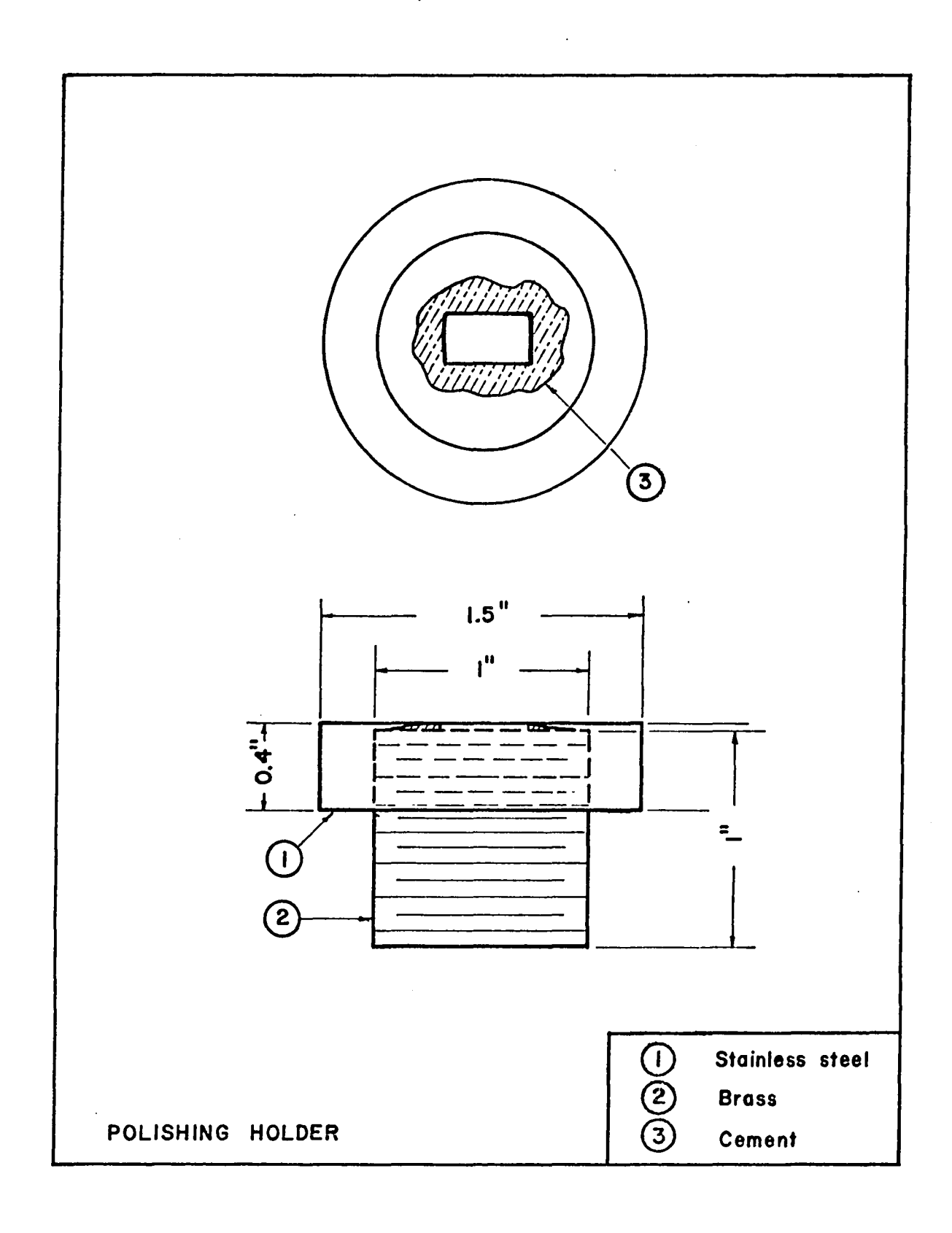
The principles and practice of spark machining have recently been reviewed by Bucklow and Cole  $^{(77)}$ . They describe the nature of spark machined surfaces, and the mechanisms that produce damage under these surfaces. It appears that less damage is introduced in this way than by careful mechanical sawing and grinding. Actual figures, quoted in the literature, indicate that for silicon iron (3.2% Si) a depth of damage of less than  $20~\mu\text{m}$  is produced on range 5 and  $< 2~\mu\text{m}$  on range 7.

### 3.5.2 Mechanical polishing of specimens

The surface resulting from spark machining was not perfectly smooth and it was found that the preparation of thin foils directly from spark-machined slices resulted in preferential, irregular thinning. The results were greatly improved when the slices were mechanically polished prior to chemical and electrochemical polishing. A sample holder, shown in Fig.10, was constructed in order to maintain parallelism between the faces of the slice. The slice was glued to the brass screw by means of

Polishing holder for thin slices





a few drops of No. 70C Lakeside brand thermoplastic (quartz) cement.\*

One face was then polished, flatness being ensured by means of the stainless steel ring. Polishing of the other face was performed, after the slice was turned over by heating the brass screw on a hot plate (cement flow point:  $140^{\circ}$ C). Polishing was performed on a series of emery papers, with water as lubricant, starting with a 220-grit paper, followed by 320, 400 and 600-grit papers. The polished slices, by now roughly .4 mm thick, were carefully washed in acetone, rinsed in methanol and dried.

# 3.5.3 Thinning procedures

Numerous thinning techniques are described in the literature (78-84). Various methods were tried in the present investigation and thin foils for transmission electron microscopy were produced in two ways: an electropolishing/thinning procedure, and a chemical thinning procedure, both of which will now be described.

# A. Jet machining and electrolytic thinning

First the polished slices were further reduced to 0.3 mm in thickness by means of a chemical polishing solution having the following composition in volume per cent (79):

15% HC1

30% HNO2

10% HF

45% H<sub>2</sub>0

<sup>\*</sup> Supplied by H. Courtright and Co., Chicago, Illinois.

The slices held by tweezers were immersed in the hot solution (75°C), and rotated regularly in order to keep the faces parallel.

A jet machining device was constructed in order to cut out discs from the above slices. The electrolyte, projected as a thin jet stream, was translated in a circular direction by means of a variable speed motor and an eccentric shaft arrangement. The electrolyte used was a 50% HCl solution in water, and the size of the cutting jet was roughly 0.1 mm. Approximately 20 min. were required to cut a disc from the 0.3 mm thick sheet at a voltage of 100V. A connecting gap was maintained between the disc and the slice for further electrothinning purposes. Dishing in the centre of the disc was performed with a thicker (0.2 mm) stationary jet, under 80 volts, until the thickness in the centre of the disc had reached 50 - 100  $\mu$ m. This usually required 30 seconds. The final thinning was performed under microscopic observation in an electrolyte having the following composition (by volume) (84):

10% HC10,

90% СН<sub>3</sub>СООН

Here the cathode was a stainless steel sheet. Microstop lacquer was used to stop off any parts not requiring thinning; that is, the tweezer and all of the slice but the small disc. Electrowinning performed under 12 volts (29) at a current density of 0.1 amp/cm² was continued until perforation occurred in or near the center of the disc. The foil was then cleaned in microstop reducer, washed and rinsed in methanol and dried between two sheets of filter paper.

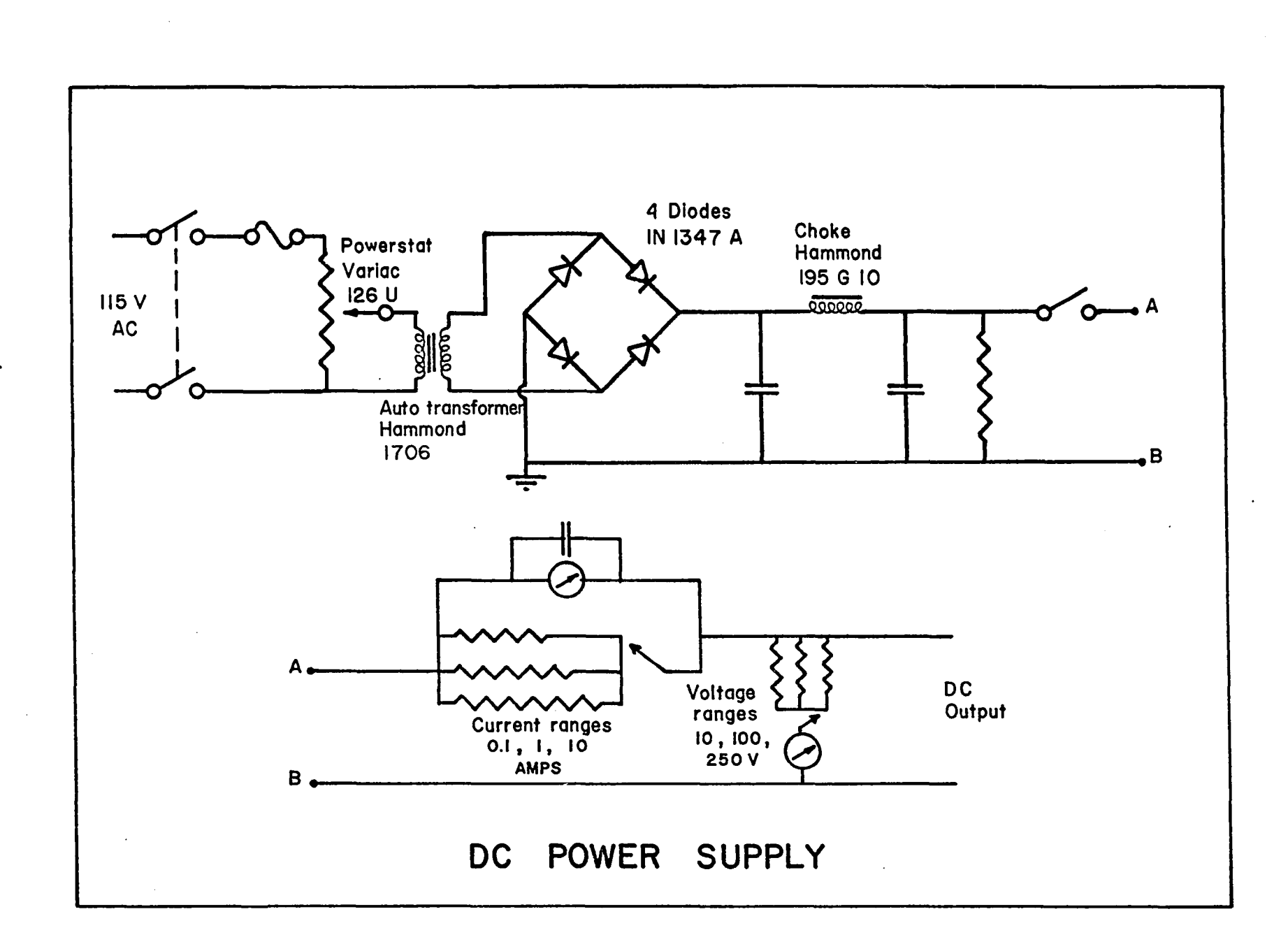
All the above electrolysis was performed with a DC power supply built by the author, following standard circuit diagrams (see Fig.11).

Only the Armco iron samples were thinned according to this procedure,

Ø

FIGURE 11

Circuit diagram of the DC power supply



and many Armco iron samples were also prepared by the chemical thinning method, which will now be described.

### B. Chemical thinning

The polished slices of both Armco iron and silicon steel were chemically thinned in a solution suggested by Packwood (85), having the following composition in volume per cent:

80% H<sub>2</sub>O<sub>2</sub> (30%) 5% HF (48%)

15% H<sub>2</sub>0

The slices held with platinum-tipped tweezers were rotated continuously in a 100 ml. bath of the above solution. Polishing from 0.4 mm down to a few microns required roughly 10 minutes. As perforations appeared within the slice, the foil was rapidly transferred into a bath of absolute ethyl alcohol. Pieces of foil close to the holes were then cut off by means of a fine scalpel blade. They were rinsed carefully in three successive baths of ethanol, dried on filter paper and carried to the electron microscope as soon as possible, to avoid oxidation of the metal. The remaining material was then further polished until new holes appeared, and again pieces of foil were cut off, the whole procedure being repeated until no further material was left. In this way many small thin foils were obtained, at random, from one slice of the compressed sample.

### 3.5.4 Electron microscopy

Transmission electron microscopy of the foils of Armco iron and silicon steel was performed on a PHILIPS EM 300 (100 kV) electron micro-

scope. The instrument was equipped with a goniometer stage, permitting rotation of the specimen and tilting up to ±45°. A liquid nitrogen "cold finger" next to the specimen reduced contamination of the foil by the electron beam. The microscope was run under an accelerating voltage of 100 kV for maximum penetration. The magnifications used were in the range 5000X to 30,000X. Photomicrographs were taken on 3 1/4 x 4 in Kodak electron image plates. Developing was performed in a two-bath, saturation process developer (DIAFINE). Selected area electron diffraction patterns were recorded for all observed samples, in order to check the misorientation between adjacent subgrains. A variable diffraction aperture was used for this purpose. Since the specimen and the diffraction was possible at any magnification. The patterns were produced in three different ways:

- a) The electron beam was passed through the center of two adjacent subgrains and the two separately exposed patterns were subsequently compared by superimposition.
- b) The beam was directed toward a sub-boundary, and the displacement of the spots originating from the two adjacent subgrains
  was determined.
- c) The diffraction aperture was opened, in order for the beam to cover several subgrains, and again the relative positions of the patterns were compared.

These three techniques have been used previously by various investigators (24,26,28,38). In the present study, only qualitative observations were recorded.

# 3.6 <u>Determination of Subgrain Size</u>

Subgrain size was determined by methods usually described for grain size measurements. These methods can be divided into three groups (86):

- a) counting methods;
- b) comparison methods;
- c) determination of the grain size distribution.

In the present investigation, counting procedures were used for the measurement of subgrain size and some subgrain size distributions were also determined. Measurements were made from traced copies of the electron micrographs.

# 3.6.1 Planimetric method (Jeffries procedure)

A rectangle of known area, 5,6,7 or 8 cm<sup>2</sup>, was superimposed on the  $3\frac{1}{4} \times 4$  in. electron micrograph. The number of complete subgrains plus one half the number of the subgrains intersected by the perimeter of the rectangle was taken as the total equivalent number of subgrains lying within this area. The total area divided by the number of subgrains counted in this fashion was taken as the average subgrain area  $\overline{A}$ . The square root of this value,  $\sqrt{\overline{A}}$ , is taken as the subgrain size. This procedure is described in more detail in reference 87. Since the magnifications were not standardized, the ASTM formulae were modified in order to allow for the various magnifications used. The final formula was:

$$\bar{d} = \frac{10,000}{M} \sqrt{\frac{A}{N}}$$
 (5-3)

where  $\bar{d}$  is the average subgrain "diameter" in  $\mu m$ 

A is the area of the rectangular frame used, in  ${\rm cm}^2$  N is the total equivalent number of subgrains, and M is the magnification of the electron micrograph.

## 3.6.2 Intercept method (Heyn's procedure)

Basically this method involves drawing at random one or more straight lines across the subgrains to be measured. The number of points of intersection between these lines and the sub-boundaries can then be counted. The total length of the lines divided by the number of intersections gives the average subgrain size or mean linear intercept,  $\bar{\ell}$ . Again, the method is described in reference 87.

In the present work, the mean linear intercept was determined by means of an image analysing computer, the Quantimet (QTM), from Metals Research Ltd. The Quantimet was equipped with an epidiascope, thus permitting direct quantitative analysis of the traced copies of the electron-micrographs.

The function of the Quantimet was to detect, on the basis of optical intensity and contrast, the sub-boundary tracings and then to perform some computing operations on the detected features. A threshold control was used to set an optical intensity below which the Quantimet would not detect sub-boundaries. The threshold was then increased until only the dark outlines of the sub-boundaries were detected, as indicated by the monitoring cathode ray tube (CRT). The instrument was calibrated to give directly the average number of sub-boundary intersections/horizontal scan within a reference frame of known dimensions. This was achieved by super-imposing, on the monitor, the image of a rectangle of known dimensions with a blank frame. The mean linear intercept is then simply given by the formula:

$$\bar{\ell} = \frac{10,000}{M} \times \frac{L}{\bar{N}}$$
 (5-4)

where  $\overline{\boldsymbol{\ell}}$  is the mean linear intercept in  $\mu m$ 

L is the horizontal length of the frame in cm

M is the magnification of the electromicrograph, and

N is the average number of intercept/CRT scan.

A frame 7 cm long (L=7cm) was chosen for the present work. The blank frame on the monitor was made up of 100 to 150 scanning lines, and two sets of two readings each were taken from each plate. One set was taken in a direction perpendicular to that of the other. The four readings were then averaged for each plate and successively for all plates.

The Quantimet has a facility for rejecting counts from features shorter than a chosen horizontal length on the monitor screen. Readings were taken for a few representative samples at various settings of this size rejection (minimum chord) control in order to obtain a chord size distribution of the detected features. In Chapter 4, these results will be described.

#### Chapter 4

## EXPERIMENTAL RESULTS

# 4.1 <u>True Stress - True Strain Curves</u>

The true stress-true strain curves shown in Figs.12 and 13 are for continuous constant strain rate deformation and those in Figs.14 and 15 are for various sequences of strain rate change in both Armco iron and silicon steel. In Figs.16 to 18, curves which have been corrected for the elastic compression of the testing train are compared with uncorrected curves.

Friction and barrelling were minimized by the use of the lubricant (25,39,74) described in section 2.4. The effectiveness of lubrication was increased by the practice of grooving the end faces (25,74) of the specimens, as mentioned earlier. In the early part of the investigation, corrections were also made for the presence of friction, using the empirical equation suggested by Siebel and subsequently applied by Uvira (25) to Armco iron and silicon steel:

$$\frac{\sigma_{AV}}{\sigma} = \left(1 - \frac{2}{3}\psi - \frac{R}{h}\right) \tag{4-1}$$

Here  $\sigma_{\mbox{AV}}$  is the average stress for a cylinder loaded in compression

- σ is the flow stress
- $\psi$  is the coefficient of friction,  $\simeq$  0.1 and

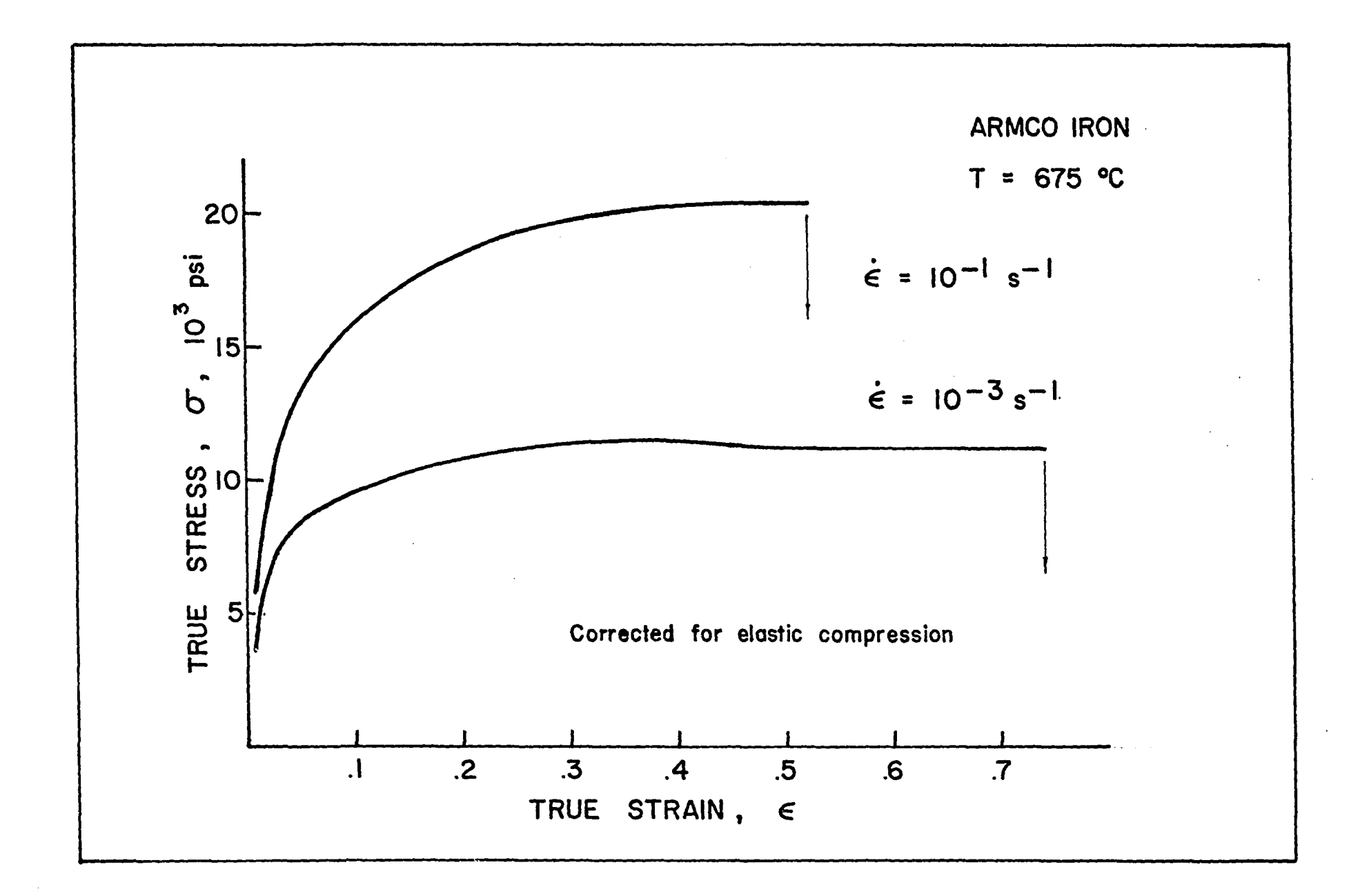
R and h are the specimen radius and length.

However, the present results are not corrected for friction, since barrelling was almost always absent, and hence frictional effects were

True stress-true strain curves for Armco iron

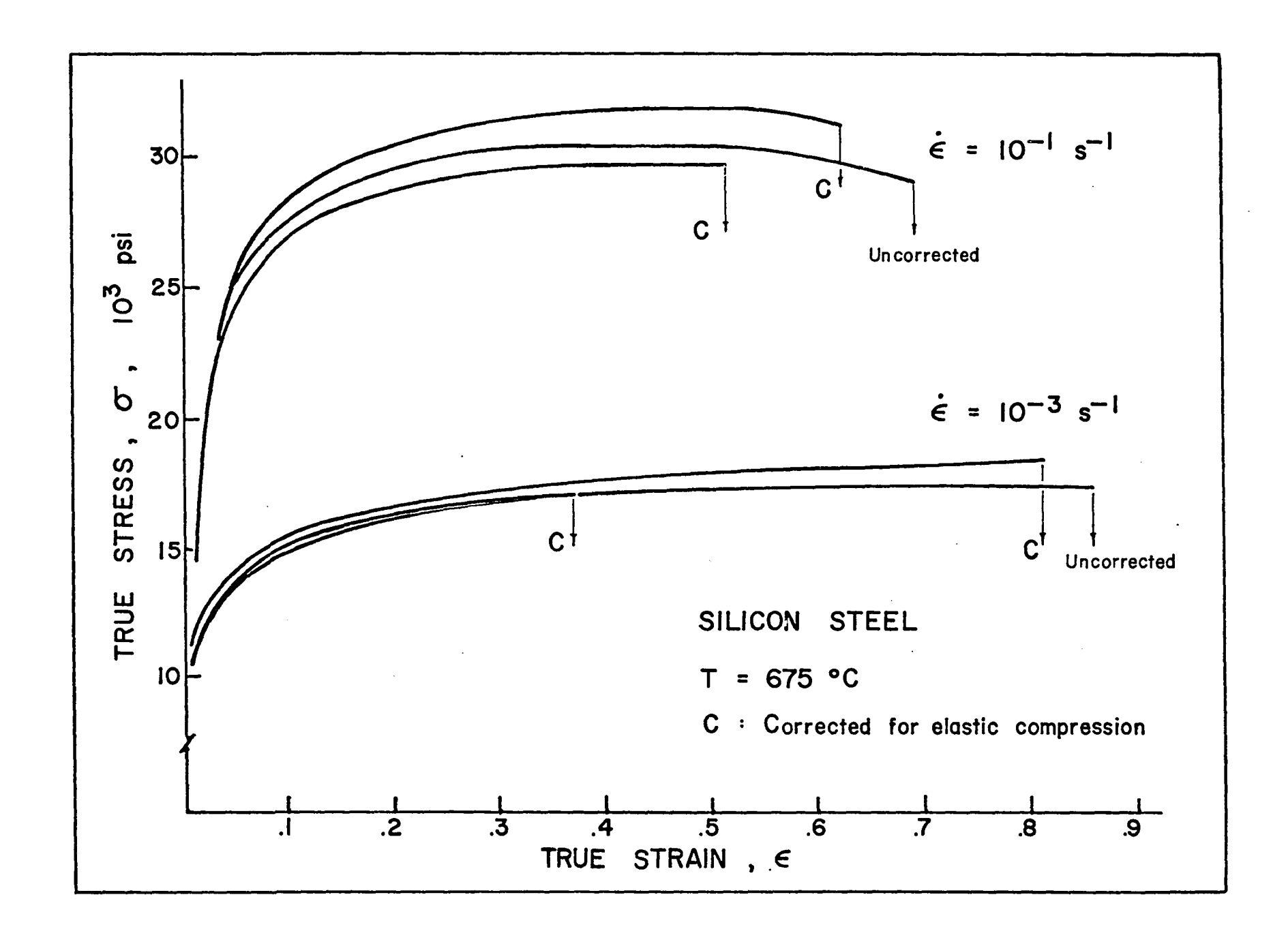






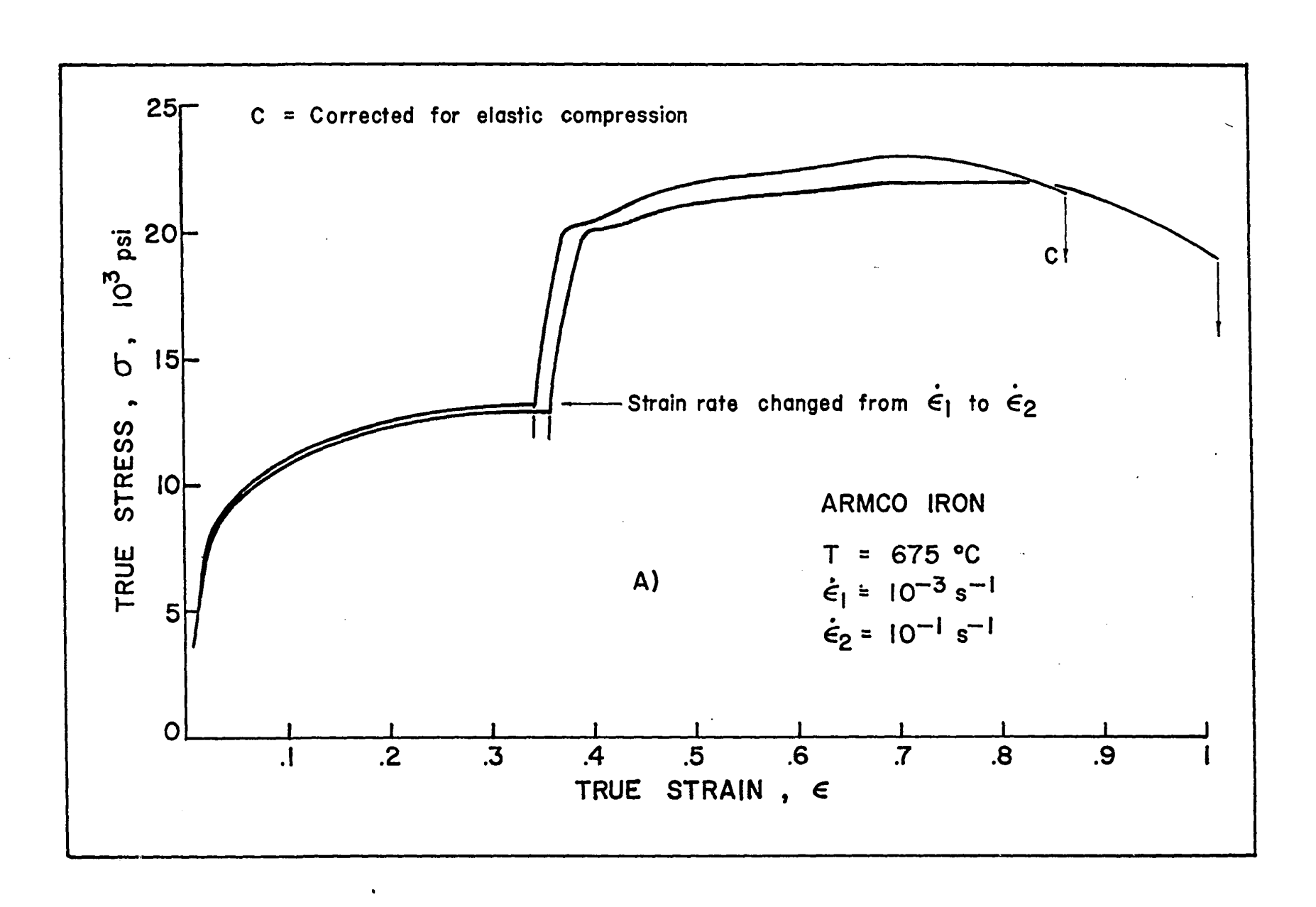
True stress-true strain curves for silicon steel



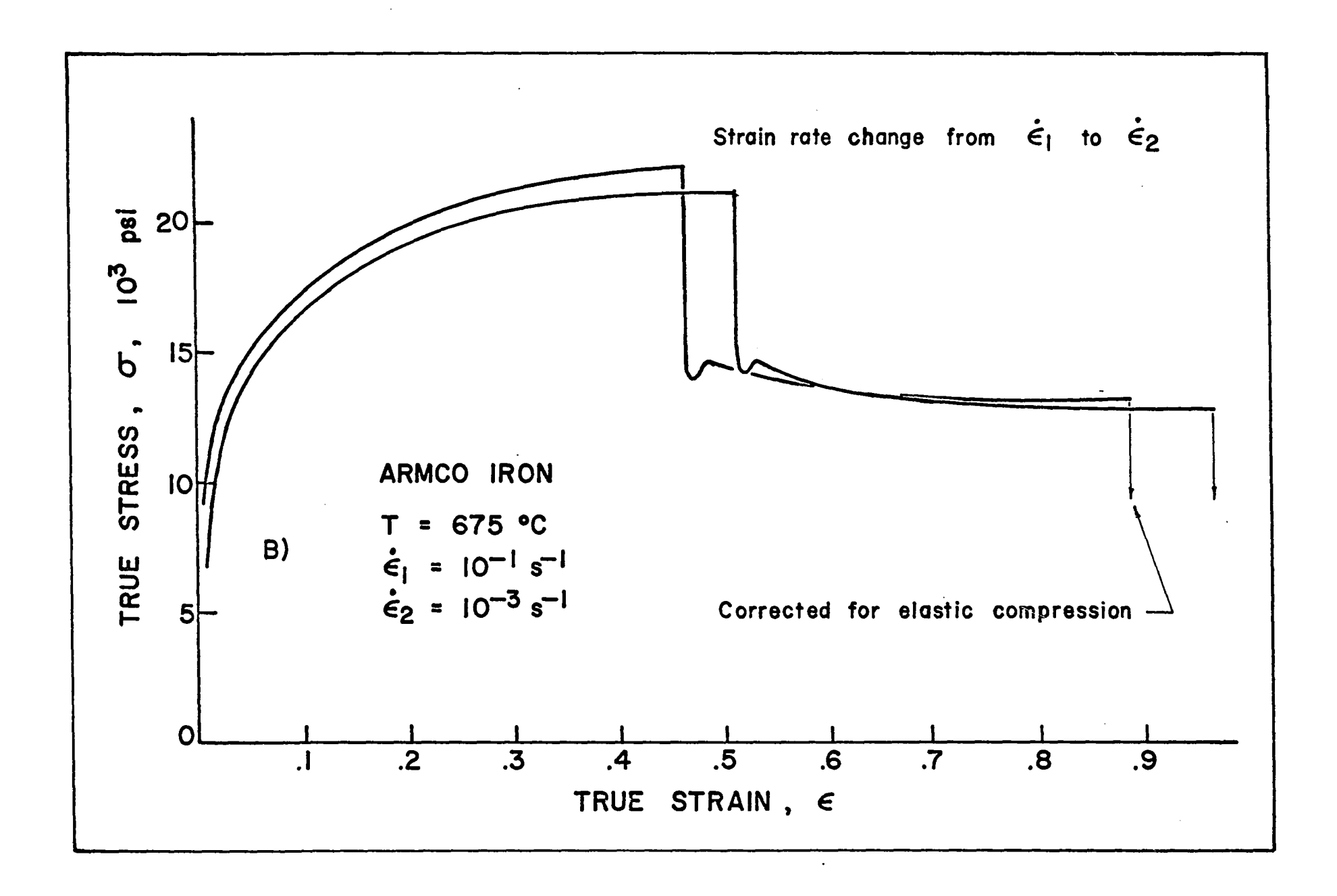


True stress-true strain curve for Armco iron showing the effect on the flow stress of:

- a) a sudden increase in strain rate
- b) a sudden decrease in strain rate

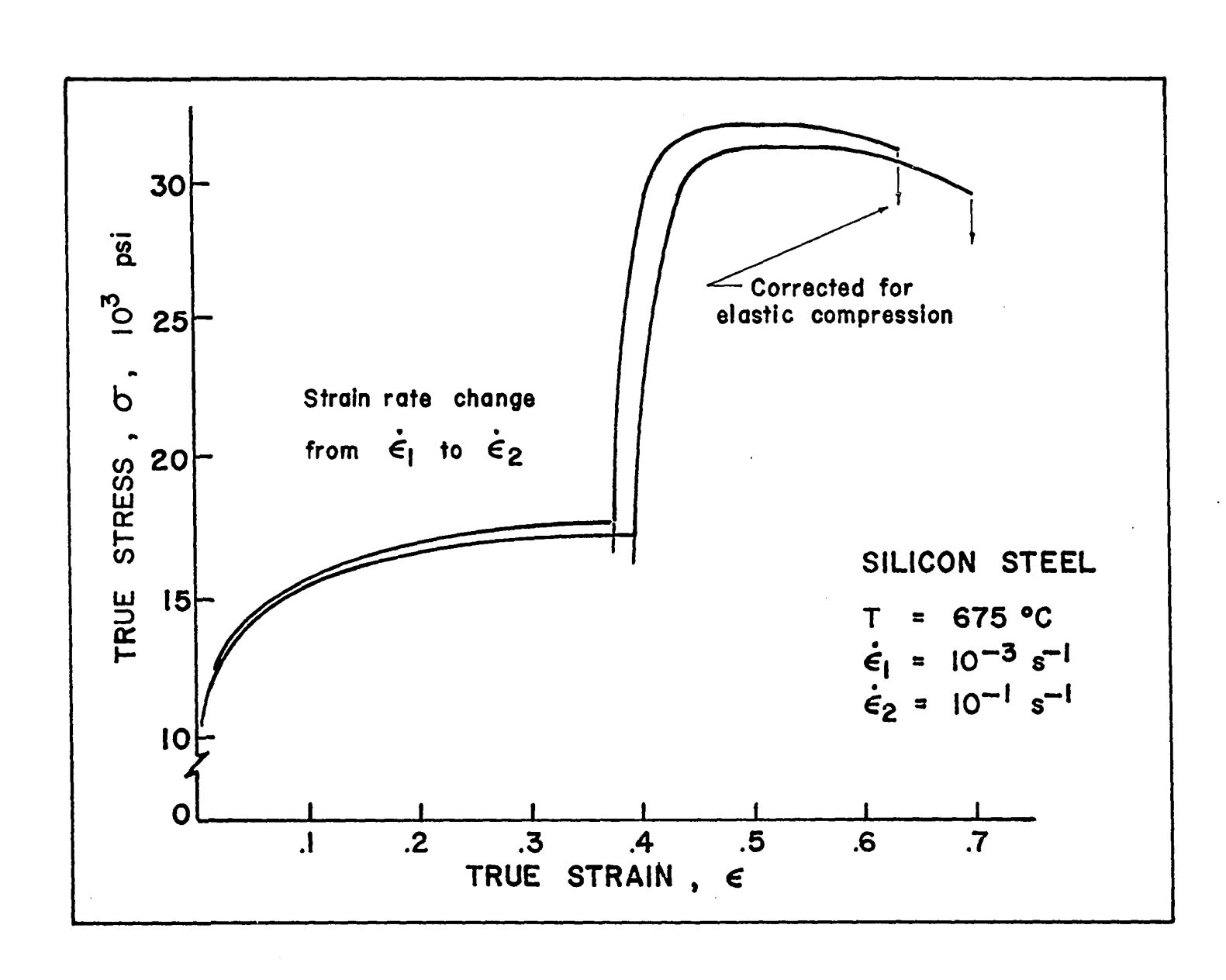


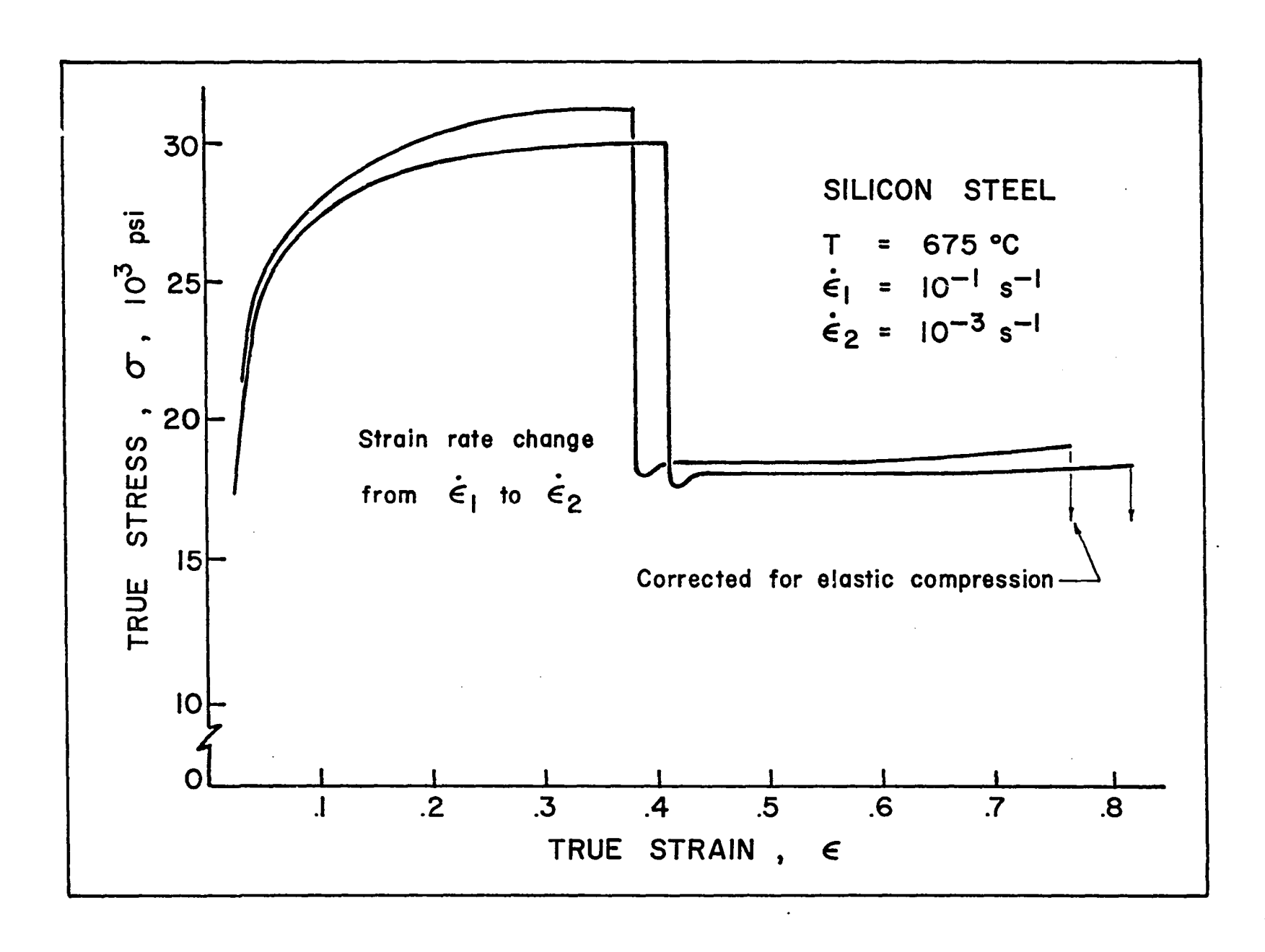




True stress-true strain curve for silicon steel showing the effect on the flow stress of:

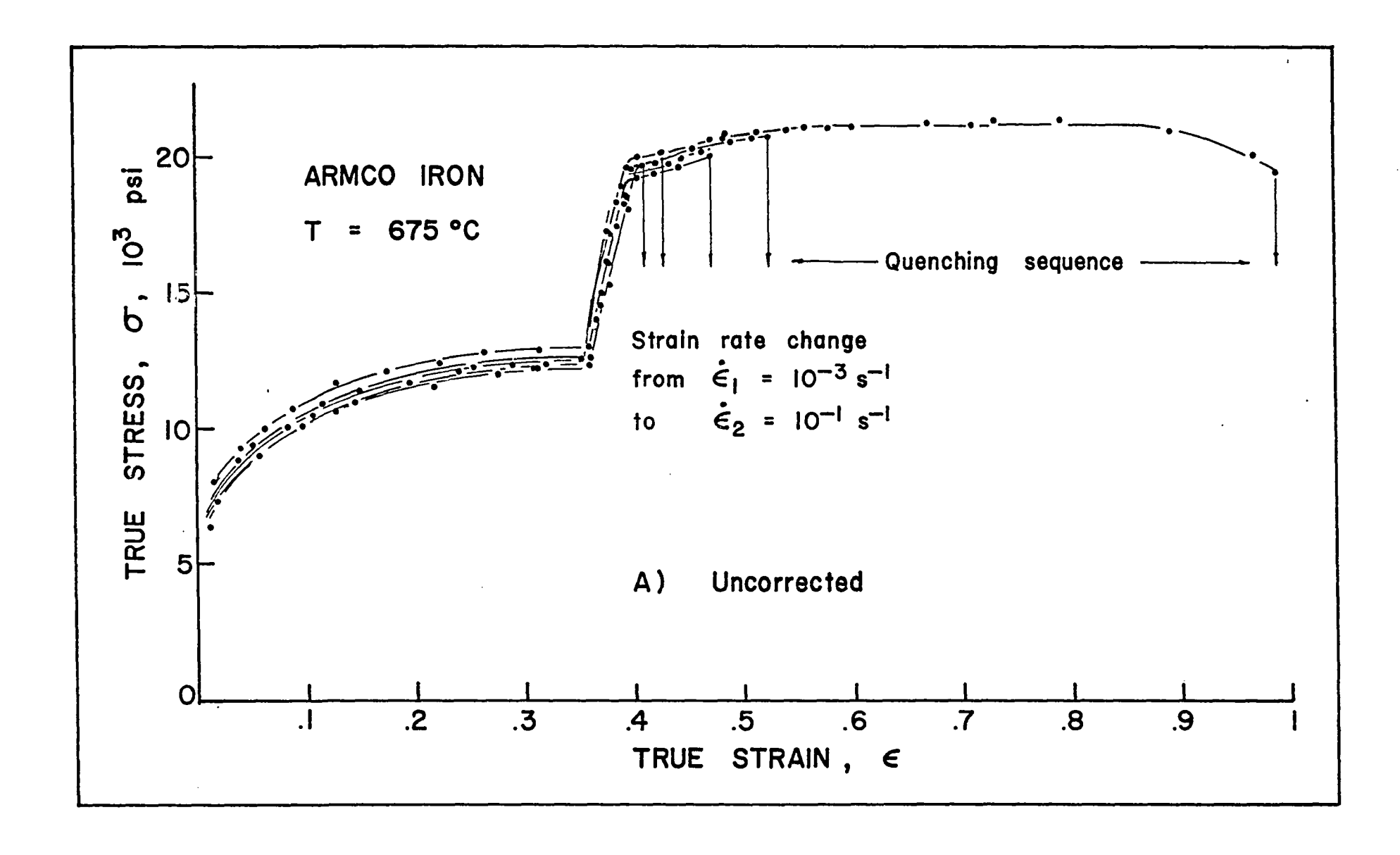
- a) a sudden increase in strain rate
- b) a sudden decrease in strain rate

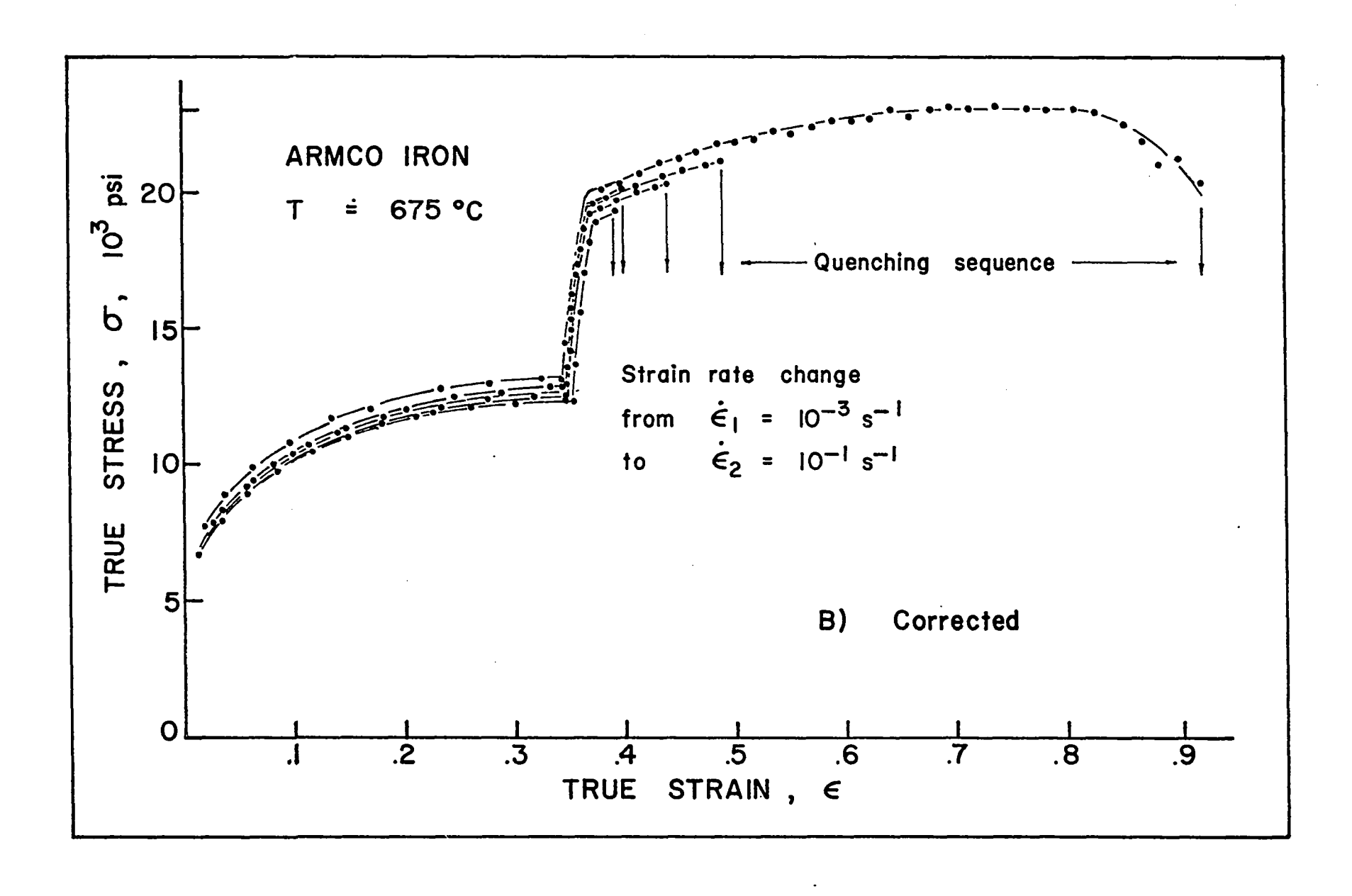




Armco iron quenching sequence along the transient resulting from a strain rate increase

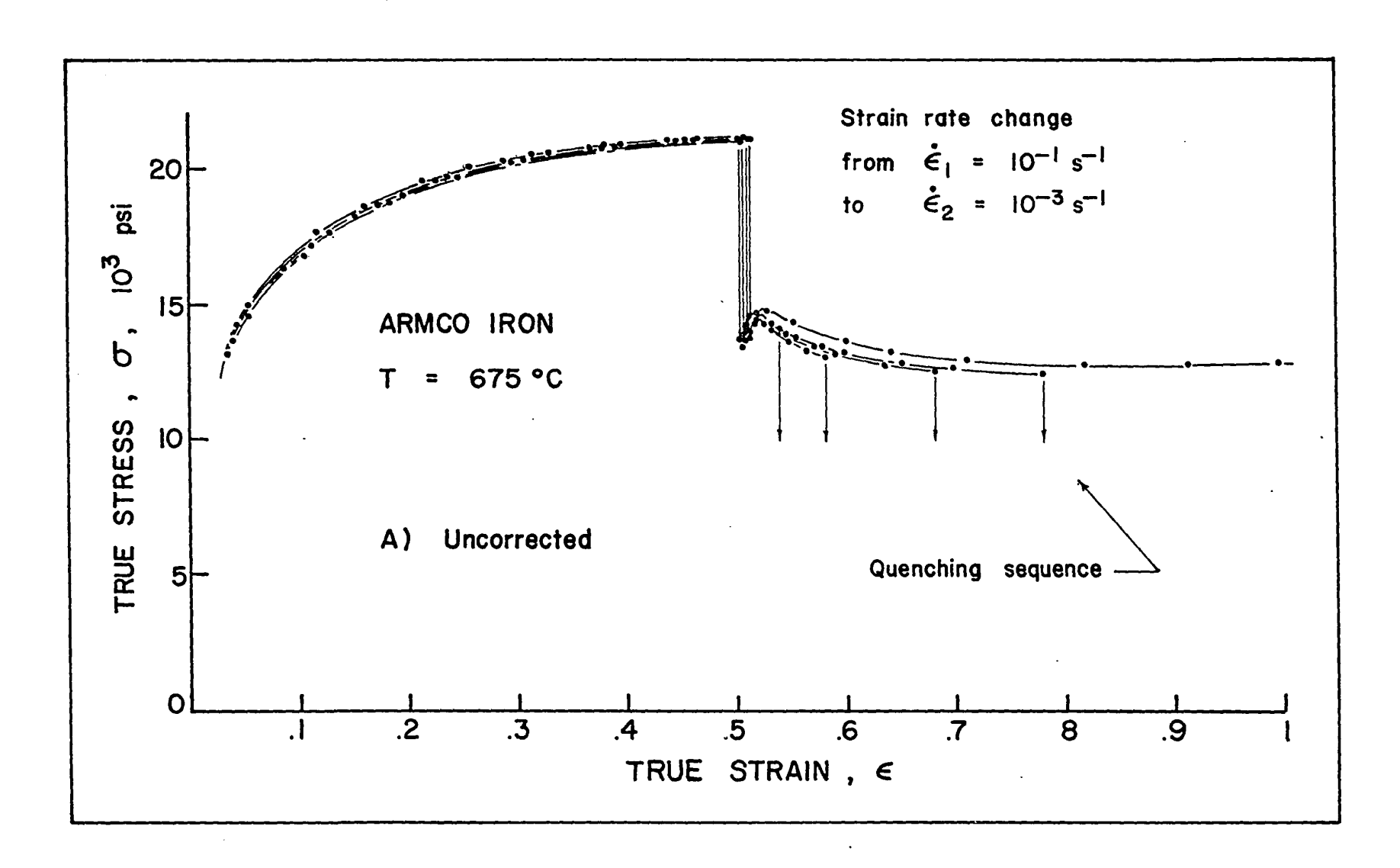
- a) uncorrected
- b) corrected for elastic compression of the testing train

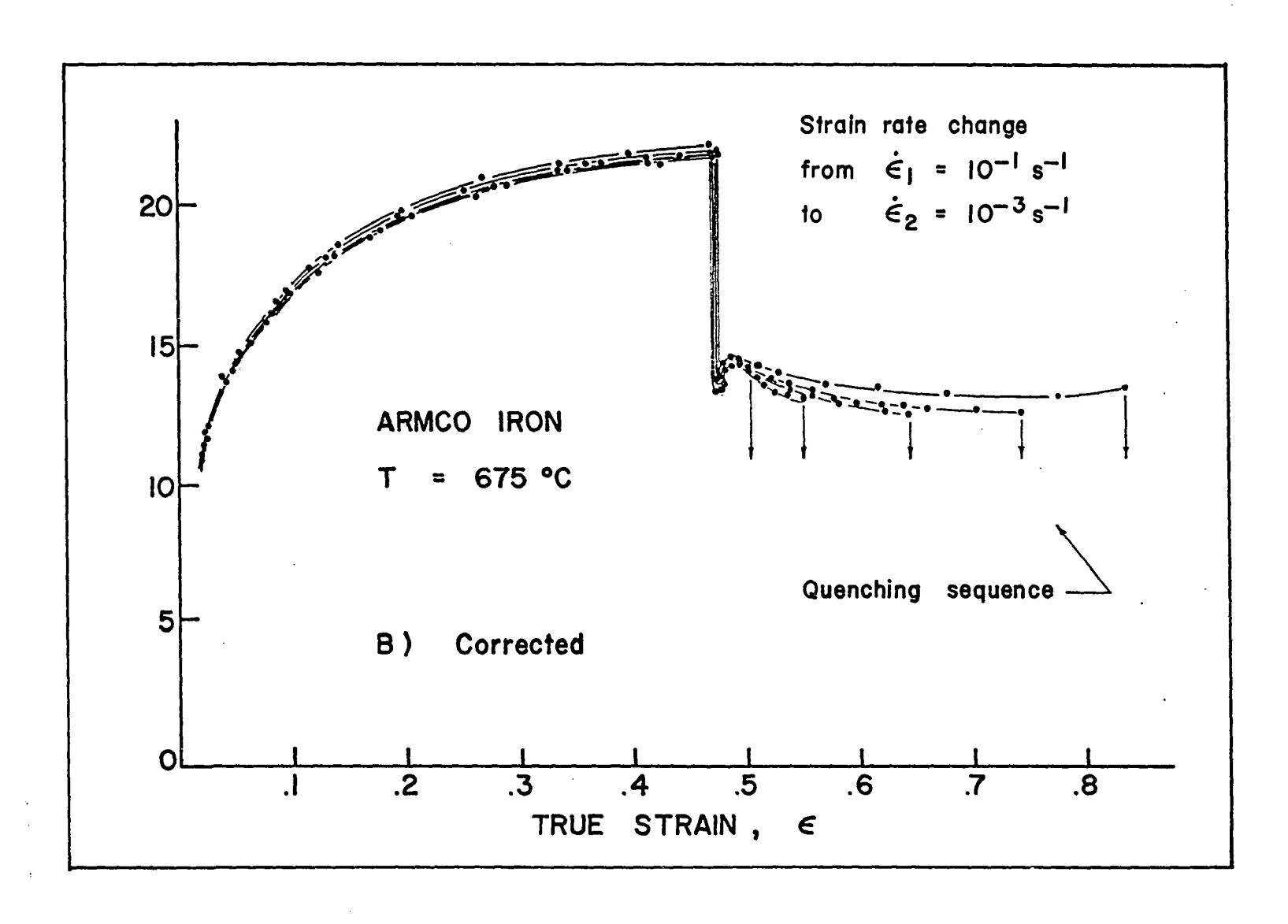




Armco iron quenching sequence along the transient resulting from a strain rate decrease

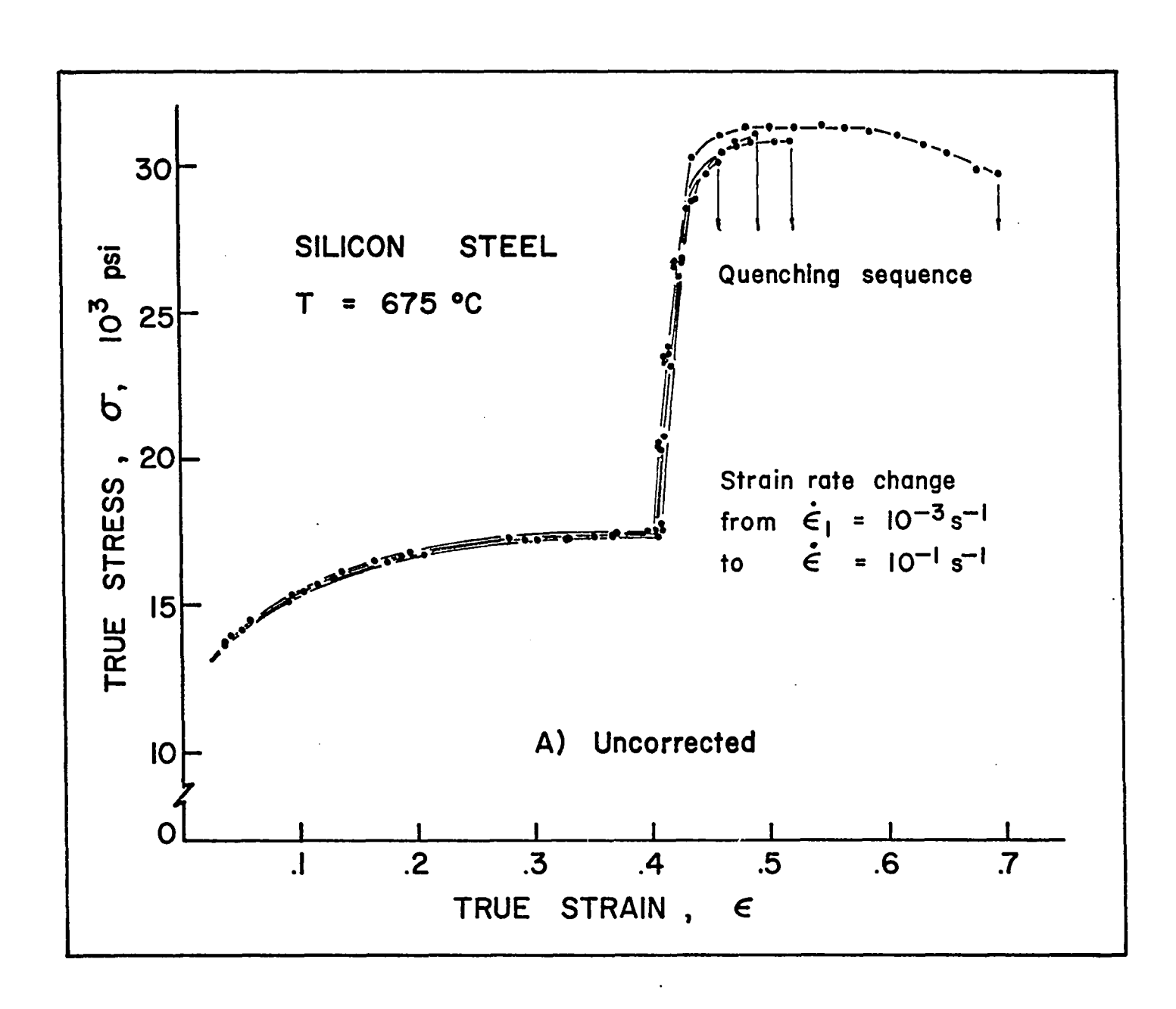
- a) uncorrected
- b) corrected for elastic compression of the testing train

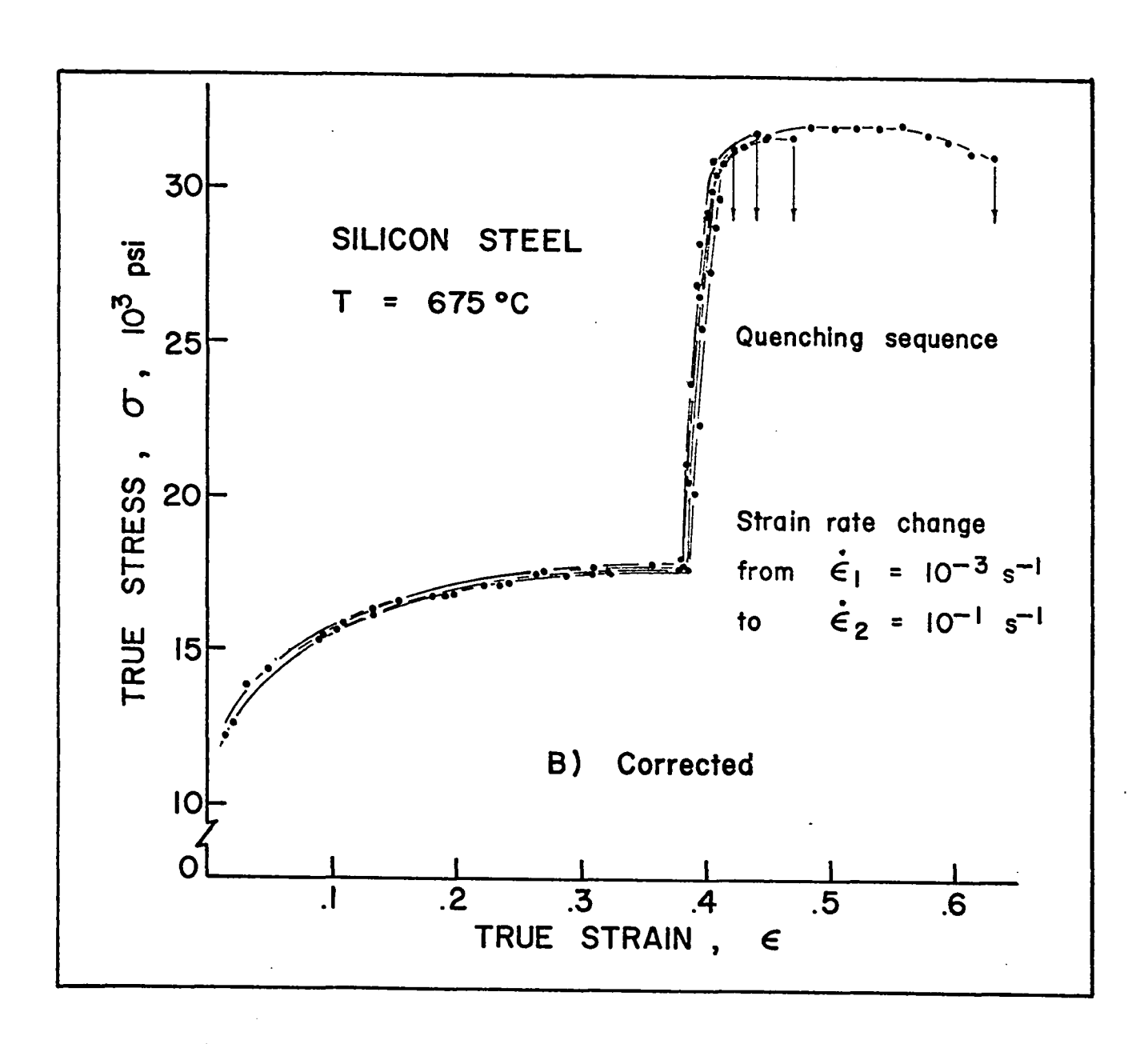




Silicon steel quenching sequence along the transient resulting from a strain rate increase

- a) uncorrected
- b) corrected for elastic compression of the testing train





judged to be negligible. In certain cases, a slight inverse barrelling was observed, the compressed samples having a "Diabolo" appearance. This was also reported by Jaoul and Séjournet (88). In most cases the walls of the cylinders remained approximately vertical. It must be noted that, in Uvira's work (25), the strains achieved were in general much higher than those attained in the present work. Also, much larger samples were used. This explains why Uvira had to apply a temperature correction for adiabatic compression at the higher strain rates. In the present case, no correction is applied since it appears that, at the strains and strain rates involved, the temperature increase is only of the order of a few degrees (Ref. 25, Table V).

The curves shown in Figs.12, 13 to 15, 16b and 17b are corrected for the elasticity of the compression machine. These corrections will now be discussed.

### 4.1.1 Elastic compression of the testing train under load

A correction affecting both stress and strain was performed on the recorded data in order to account for the elastic compression of the ram and anvil within the high temperature region. The compressions within the temperature range 625°C to 875°C were determined by carrying out blank tests, i.e. loading in the absence of samples, and recording the strains indicated by the strain recording apparatus. In order to obtain a generalized equation applicable at all temperatures and loads, the deflections in inches were divided by the corresponding loads in pounds and this value, denoted as F, was plotted against temperature. A straight line resulted, the equation of which is given below:

$$F = 3.34 \times 10^{-6} + (2.87 \times 10^{-10})T$$
 (4-2)

where T is the temperature in the range 625°C to 875°C (expressed in degrees centigrade). The contraction of the machine under a given load and a given temperature is then simply found from:

$$D = F \times L \tag{4-3}$$

where D is the contraction of the compression machine in inches

F is given by Eq.(4-2), and

L is the load in 1b.

Eqs.(4-2) and (4-3) were derived in conjunction with M.J. Luton who designed the essential features of the compression train. The true specimen height is then given by the relation

$$h = H - D \tag{4-4}$$

where H is the recorded height, and

D is given by Eq. (4-3).

All the above operations are incorporated into the computer program that determines the true strain and the true stress from the relations described earlier

$$\varepsilon = -\ln \frac{h_0}{h} \tag{2-1}$$

$$\sigma = \frac{F}{A} \tag{3-1}$$

$$A = A_0 \frac{h_0}{h}$$
 (3-2)

It should be noted that Eqs.(4-2) and (4-3) do not lead directly to the elastic constant and expansion coefficient of the material, but to the two equivalent machine coefficients, since a temperature gradient exists within the compression chamber along the lengths of the ram and the anvil.

### 4.1.2 Transient stress-strain behaviour

Following a strain rate change, the two materials behave in some-

what different ways. In the case of the Armco iron (Figs.14a and 14b), when the strain rate is decreased, the stress drops abruptly and then decreases gradually to the stress level characteristic of the steady state at the second strain rate. The stress reaches this level after a true strain of 0.25 to 0.3 (25% to 30%). Upon a strain rate increase, an initial very rapid stress rise is followed by a gradual, smooth increase to the steady state stress indicated by the new value of the Zener-Hollomon parameter. In both cases, steady state stresses are similar during tests carried out with or without a strain rate change, as long as the same final Z applies.

With regard to the silicon steel, its behaviour differs from that of the Armco iron in that no detectable transient is observed upon a strain rate decrease (Fig.15b). When  $\dot{\epsilon}$  is increased (Fig.15a), the flow stress rises very rapidly at first. The rate of strain hardening then rapidly decreases to zero over a strain interval of approximately 5% to 8%. Once the steady state is re-established, the stress level is again similar to that obtained during a test begun under the second set of conditions.

The above observations show that, whereas strains of about 0.3 are required in the case of the Armco iron for the steady state to be re-established following a strain rate change, the change in flow stress in the silicon steel takes place over a strain interval of only 0.05 to 0.08 or less after the strain rate change is initiated.

### 4.1.3 Reproducibility of tests

Most of the curves shown in Figs.12 to 15 are for one specimen only. However, two to three samples were tested in the case of the

continuous experiments, in order to verify the reproducibility of the results. The good agreement of the data can be seen from Figs.16 to 18, where the same conditions are reproduced in effect 4 to 6 times. The true stress-true strain curves do superimpose within approximately 0.5%.

## 4.2 Electron Microscopy

The electron microscopy was carried out to investigate the behaviour of the substructure under transient conditions following a strain rate change. Examination of the steady state substructures was also carried out for comparison purposes. The observations will be described in turn, with particular emphasis on substructure breakdown during transient deformation.

# 4.2.1 Steady state substructures

With regard to samples that have not undergone a strain rate change, the observed steady state substructures compare well with those obtained by previous investigators and described in Chapter 1 of the present work. Briefly, the substructures are composed of equiaxed subgrains, the size of which decreases with an increase in strain rate. At the higher strain rates, the subgrains are less well defined, the subboundaries being more ragged. Furthermore, the dislocation density within the subgrains increases with an increase in strain rate. These observations are typified by the substructures shown in the electron micrographs of Figs.19 to 22. At the higher strain rates the subgrains appear slightly elongated, which is a characteristic of the subgrains formed at homologous temperatures below  $0.6^{(20,22)}$ . In the present case, the homologous temperature for Armco iron and silicon steel is .52  $T_m$  at  $675^{\circ}C$ .



FIGURE 19 Electron micrograph of Armco iron deformed at  $675^{\circ}$ C and at  $10^{-3}$  s<sup>-1</sup>.  $\epsilon$  = 0.74



FIGURE 20 Electron micrograph of Armco iron deformed at  $675^{\circ}\text{C}$  and at  $10^{-1}~\text{s}^{-1}$ .  $\epsilon$  = 0.52



FIGURE 21 Electron micrograph of silicon steel deformed at  $675^{\circ}$ C and at  $10^{-3}$  s<sup>-1</sup>.  $\epsilon = 0.82$ 



FIGURE 22 Electron micrograph of silicon steel deformed at  $675^{\circ}$ C and at  $10^{-1}$  s<sup>-1</sup>.  $\epsilon$  = 0.53

### 4.2.2 Transient region substructures

The substructures characteristic of the transient region are shown in the electron micrographs of Figs. 23 to 34. The main feature is the presence of equiaxed subgrains throughout the entire region corresponding to the changes in Z. However, as the strain after the change in strain rate increases, changes in subgrain size and shape can be observed. Immediately after the strain rate increase, it is difficult to detect changes in the dislocation density. However, after a few percent of strain, the subgrain size decreases and the dislocation density within the subgrains increases\* to values appropriate to the steady state substructure for the higher strain rate. In the Armco iron, the substructure geometry reaches a stable configuration by the onset of the new steady state whether the strain rate was increased or decreased. When the strain rate is decreased, the subgrain size increases and the dislocation density decreases to the values characteristic of the new steady state. By contrast, in the silicon steel it is apparent that changes in subgrain size and shape continue to take place even after the steady state of flow stress is re-established.

It is difficult to distinguish major differences between steady state and transient substructures. In both cases the sub-boundaries appear to be quite complex. Regular hexagonal networks, simple tile boundaries, irregular networks made up of mixed edge and screw dislocations, and intricate tangles can be observed in Figs.23 to 34. The misorientation between neighbouring subgrains was not observed to vary in any systematic way along the transient. Figs.35 and 36 show that

<sup>\*</sup> The observations concerning dislocation density are qualitative only, as no actual density measurements were carried out.



FIGURE 23 Electron micrograph of Armco iron deformed at  $675^{\circ}$ C. Transient region following a strain rate change from  $10^{-3}$  to  $10^{-1}$  s<sup>-1</sup>  $\epsilon$  = 0.04 after change.



FIGURE 24 Electron micrograph of Armco iron deformed at  $675^{\circ}$ C. Transient region following a strain rate change from  $10^{-3}$  to  $10^{-1}$  s<sup>-1</sup> c = 0.11 after change



FIGURE 25 Electron micrograph of Armco iron deformed at  $675^{\circ}$ C. Transient region following a strain rate change from  $10^{-3}$  to  $10^{-1}$  s<sup>-1</sup>.  $\epsilon = 0.14$  after change



FIGURE 26 Electron micrograph of Armco iron deformed at  $675^{\circ}\text{C}$ . Transient region following a strain rate change from  $10^{-3}$  to  $10^{-1}$  s<sup>-1</sup>.  $\epsilon$  = 0.57 after change

Mark States Asset



FIGURE 27 Electron micrograph of Armco iron deformed at  $675^{\circ}$ C. Transient region following a strain rate change from  $10^{-1}$  to  $10^{-3}$  s<sup>-1</sup>.  $\epsilon = 0.03$  after change



FIGURE 28 Electron micrograph of Armco iron deformed at  $675^{\circ}$ C. Transient region following a strain rate change from  $10^{-1}$  to  $10^{-3}$  s<sup>-1</sup>.  $\epsilon = 0.08$  after change



FIGURE 29 Electron micrograph of Armco iron deformed at  $675^{\circ}$ C. Transient region following a strain rate change from  $10^{-1}$  to  $10^{-3}$  s<sup>-1</sup>.  $\epsilon = 0.17$  after change



FIGURE 30 Electron micrograph of Armco iron deformed at  $675^{\circ}$ C. Transient region following a strain rate change from  $10^{-1}$  to  $10^{-3}$  s<sup>-1</sup>.  $\epsilon = 0.32$  after change



FIGURE 31 Electron micrograph of silicon steel deformed at  $675^{\circ}$ C. Transient region following a strain rate change from  $10^{-3}$  to  $10^{-1}$  s<sup>-1</sup>.  $\epsilon$  = 0.03 after change



FIGURE 32 Electron micrograph of silicon steel deformed at  $675^{\circ}$ C. Transient region following a strain rate change from  $10^{-3}$  to  $10^{-1}$  s<sup>-1</sup>.  $\epsilon = 0.06$  after change



FIGURE 33 Electron micrograph of silicon steel deformed at  $675^{\circ}$ C. Transient region following a strain rate change from  $10^{-3}$  to  $10^{-1}$  s<sup>-1</sup>.  $\epsilon = 0.09$  after change



FIGURE 34 Electron micrograph of silicon steel deformed at  $675^{\circ}$ C. Transient region following a strain rate change from  $10^{-3}$  to  $10^{-1}$  s<sup>-1</sup>.  $\epsilon = 0.25$  after change



FIGURE 33 Electron micrograph of silicon steel deformed at  $675^{\circ}$ C. Transient region following a strain rate change from  $10^{-3}$  to  $10^{-1}$  s<sup>-1</sup>.  $\epsilon$  = 0.09 after change



FIGURE 34 Electron micrograph of silicon steel deformed at  $675^{\circ}\text{C}$ . Transient region following a strain rate change from  $10^{-3}$  to  $10^{-1}$  s<sup>-1</sup>.  $\epsilon$  = 0.25 after change

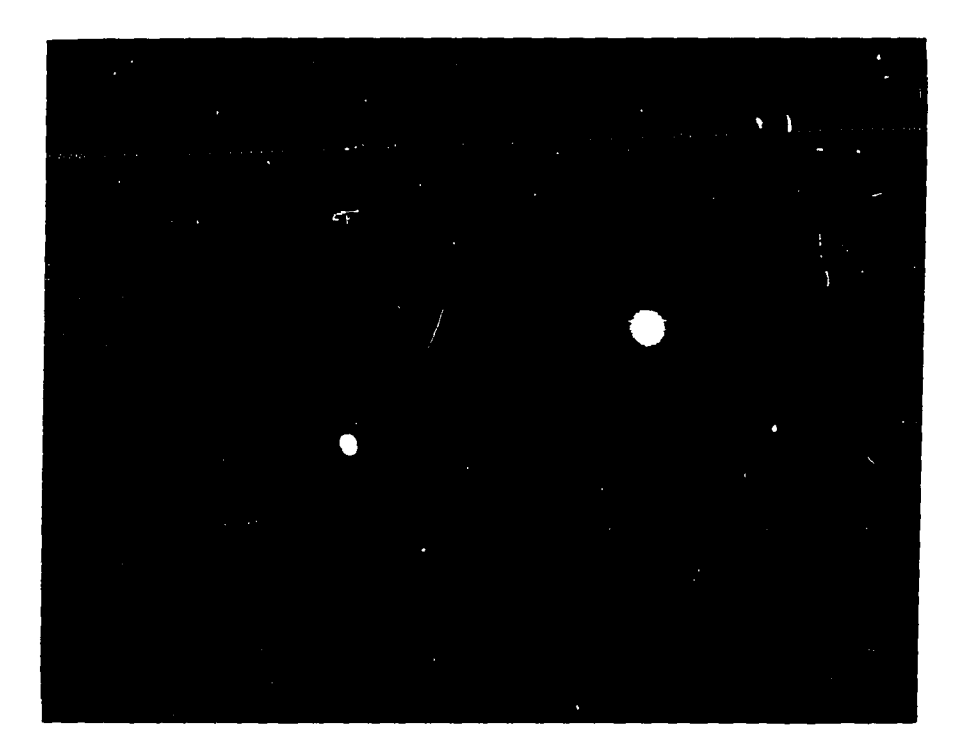


FIGURE 35 Electron diffraction pattern from a cluster of subgrains in Armco iron (111 reflections).



FIGURE 36 Electron diffraction pattern from a cluster of subgrains in silicon steel (110 reflections)

)

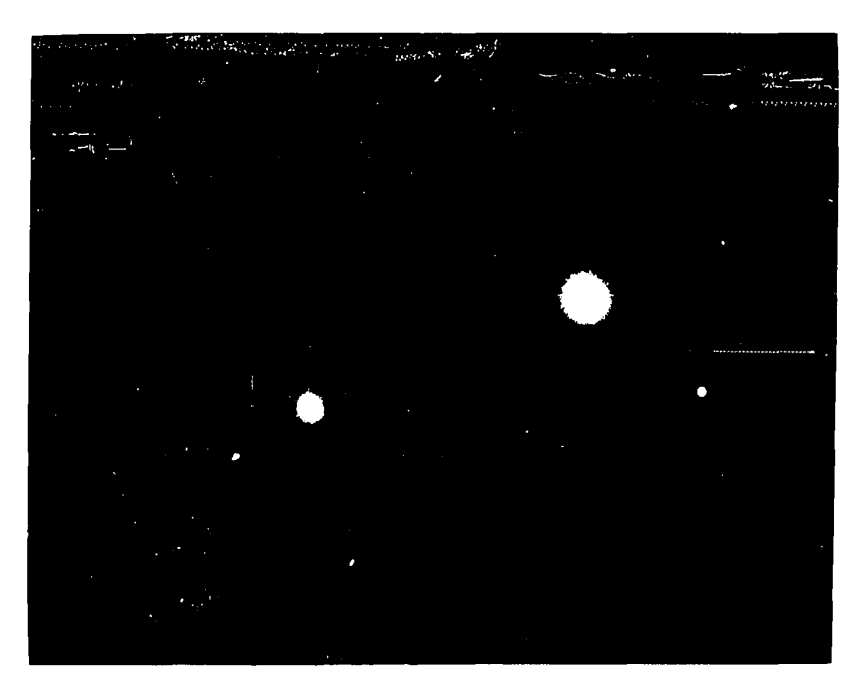


FIGURE 35 Electron diffraction pattern from a cluster of subgrains in Armco iron (111 reflections).



FIGURE 36 Electron diffraction pattern from a cluster of subgrains in silicon steel (110 reflections)

the misorientations are similar to those present in steady state substructures and fall within the range observed and quoted in the literature (25,26), i.e. 1 to  $7^{\circ}$ .

### 4.3 Subgrain Size Measurements

Table V gives a brief survey of the previous work regarding subgrain size measurement. None of the above investigations cover transient hot working. It must also be noted that the spread in the reported values is considerable, and it can therefore be expected that substantial scatter will generally result from subgrain size determination.

In the present investigation, subgrain sizes were determined for the two steady state substructures and for those representative of the transient region that followed a sudden strain rate change. The results are given in Table VI for Armco iron and Table VII for silicon steel. The subgrain sizes obtained by the planimetric method (Jeffries' procedure) and the intercept method (Heyn's procedure) are given in both tables, together with their corresponding 95% confidence limits (that is the limits which will contain the subgrain size with a probability of 95%). The formulae described in sections 3.6.1 and 3.6.2 were used for the determination of  $\bar{d}$  and of  $\bar{\ell}$ . Each individual value was obtained from a count of 300 to 450 subgrains covering 8 to 12 photographic plates. In the counting procedure, k plates were analysed, each plate having n subgrains. It can then be shown that the standard deviation (or standard error) of the mean subgrain size is given by (93):

$$SE_{(\bar{d})} = S_{(\bar{d})} = \sqrt{\frac{\sum_{0}^{i} (\bar{d}_{i} - \bar{d})^{2}}{k(k-1)}}$$
 (4-1)

where  $\bar{\mathbf{d}}$  is the mean subgrain size , and

 $\overline{\mathbf{d}}_{\mathbf{1}}^{+}$  represents the individual averages from each measurement.

The 95% confidence limits quoted in Tables VI and VII are given by the relation (93)

95% confidence limits = 
$$\pm 2 \text{ SE}_{(\overline{d})}$$
 (4-2)

It appears from an observation of the tables that the subgrain size changes gradually over the transient region that follows the strain rate change. In the case of the Armco iron the subgrain size decreases with strain after an increase in strain rate and increases after a decrease in strain. These changes are shown in Figs. 37 and 38.

From the tables it can also be seen that the mean linear intercept is consistently smaller than the mean subgrain size determined by the areal or planimetric method. This has also been observed by Phillips in his investigation of the grain size of rolled aluminum (94). From his Table I, it can be seen that the intercept method gives consistently higher values for the number of grains per sq. mm.. The two methods cannot therefore be used interchangeably. In the present work, the Jeffries procedure ( $\bar{d} = \sqrt{\bar{A}}$ ) was used since, due to the greater scatter in  $\overline{\ell}$  than in  $\overline{A}$ , a smaller number of grain areas than of intercepts is required to attain the same accuracy (86). Furthermore, the planimetric method involves no arbitrary assumptions concerning the uniformity of subgrain size or shape. However, the intercept method possesses the advantage that it gives a direct indication of subgrain shape as well as of size. An additional advantage of the latter method is that the measuring procedure can be automatized as described in section 3.6.2, and also allows for the determination of the size distribution. Fig. 39 shows the subgrain size distribution in representative samples of silicon steel. The two steady state distributions are shown as well as those

TABLE V

MEAN SUBGRAIN SIZES IN IRON DEFORMED AT HIGH TEMPERATURE

Material	Mode of Deformation	€ s−1	т °С	ε	Quench Delay (s)	Measuring Procedure	μm d	Ref.
Iron 99.97%	Tension	4·10 <sup>-5</sup>	-77 to 500	to 0.28	not specified	X-ray	1.2 to 2.9	89
Iron 99.97%	Tension	10 <sup>-3</sup> to 10 <sup>-4</sup>	0 to 870		not specified	X-ray TEM	8 to 70	90
Iron 99.97%	Compression creep	2.10-3	742 to 885	0.2	not specified	TEM	10	*
Iron comm. and hi. pur.	Torsion	.45 and 4.5	600 to 1050	4.5 to 1.8	10	Optical	2 to 6	91

<sup>\*</sup> Quoted in Ref. 25

TABLE V (Cont'd)

MEAN SUBGRAIN SIZES IN IRON DEFORMED AT HIGH TEMPERATURE

Material	Mode of Deformation	έ s-1	o C	ω	Quench Delay (s)	Measuring Procedure	<u>d</u> μm	Ref.
Iron BISRA 5102	Torsion	. 45	500 to 950	<b>%</b> 9	<10	Optical	1.4 to 2.3	92
Armco .26% Mn	Compression	.07 to 4.0	600 to 800	0.6 to 1.5	1 to 1500	Optical TEM	2.5-5.6	25 26
Fe-3% Si	Creep	8.3·10 <sup>-6</sup>	643	to 0.2	-	TEM	2 to 18	*
Fe-3% Si	Compression	0.075 to 0.5	650 to 1000	0.4 to 1.8	1 to 1200	Optical TEM	2.5-5.6	25 26

<sup>\*</sup> Quoted in Ref. 25

TABLE VI

EXPERIMENTAL MEAN SUBGRAIN SIZES FOR ARMCO IRON

Strain rate	ε	σ psi	Quench Delay (s)	μm d	95% conf. limit (±) μm	2 µm	95% conf. limit (±) μm
10 <sup>-1</sup>	0.52	20,600	2	1.20	0.08	-	-
10 <sup>-3</sup>	0.74	11,600	2	2.40	0.20	-	-
Original/Final	<del></del>	. <del></del>		<del></del>	<del></del>		
10 <sup>-3</sup> / 10 <sup>-1*</sup>	0.39 0.40 0.44 0.49 0.92	19,500 20,000 20,800 21,600 21,000	2 2 2 2 2	2.18 1.90 1.89 1.84 1.53	0.22 0.11 0.16 0.19 0.19	- - -	- - - -
10 <sup>-1</sup> / 10 <sup>-3**</sup>	0.50 0.55 0.64 0.79	14,000 13,200 12,600 12,400	2 2 2 2	1.87 1.99 2.32 2.41	0.15 0.09 0.22 0.15	1.56 1.63 2.12 2.01	0.10 0.10 0.20 0.28

<sup>\*</sup> Change of strain rate at strain of 0.35

<sup>\*\*</sup> Change of strain rate at strain of 0.47

TABLE VII

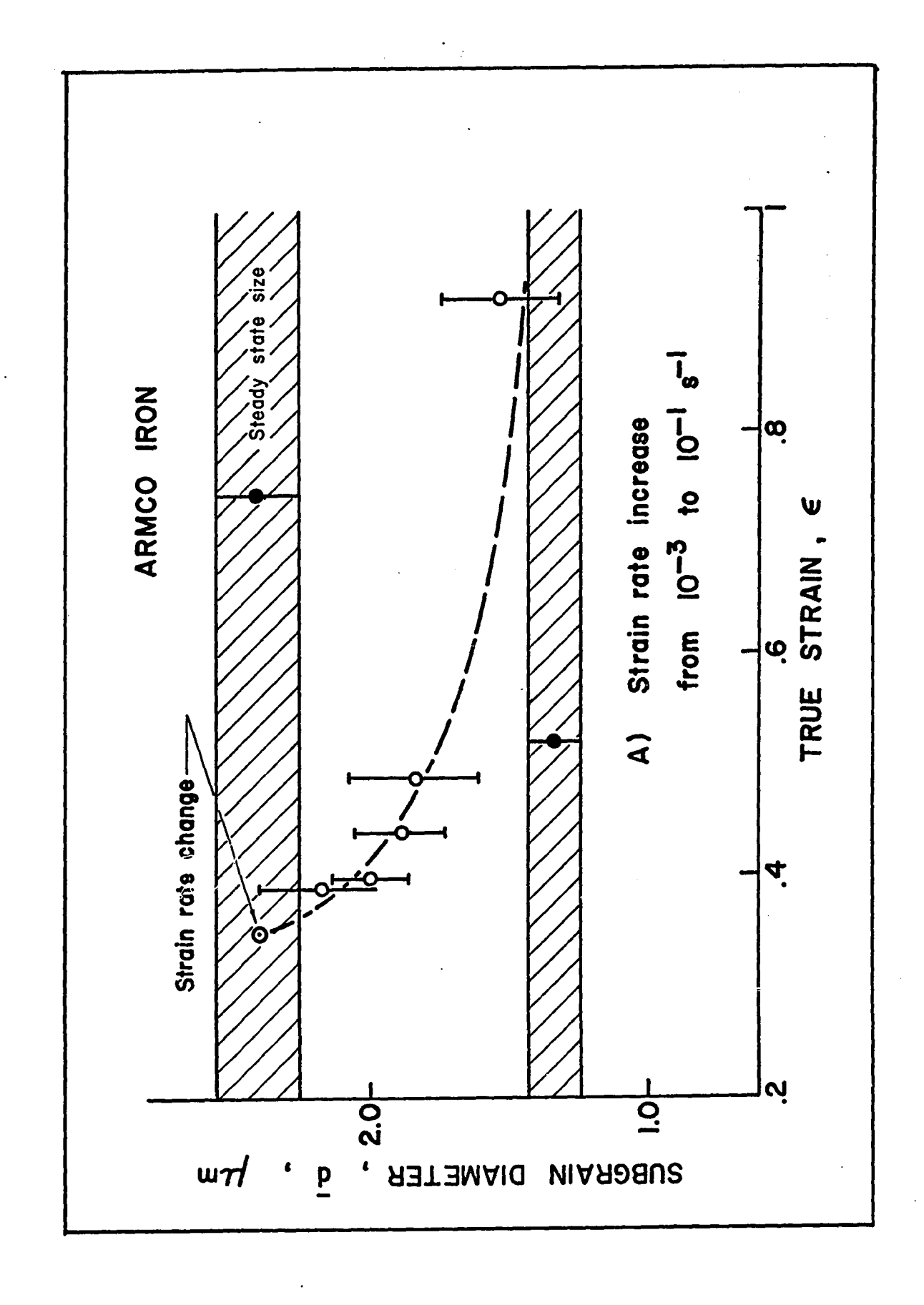
EXPERIMENTAL MEAN SUBGRAIN SIZES FOR SILICON STEEL

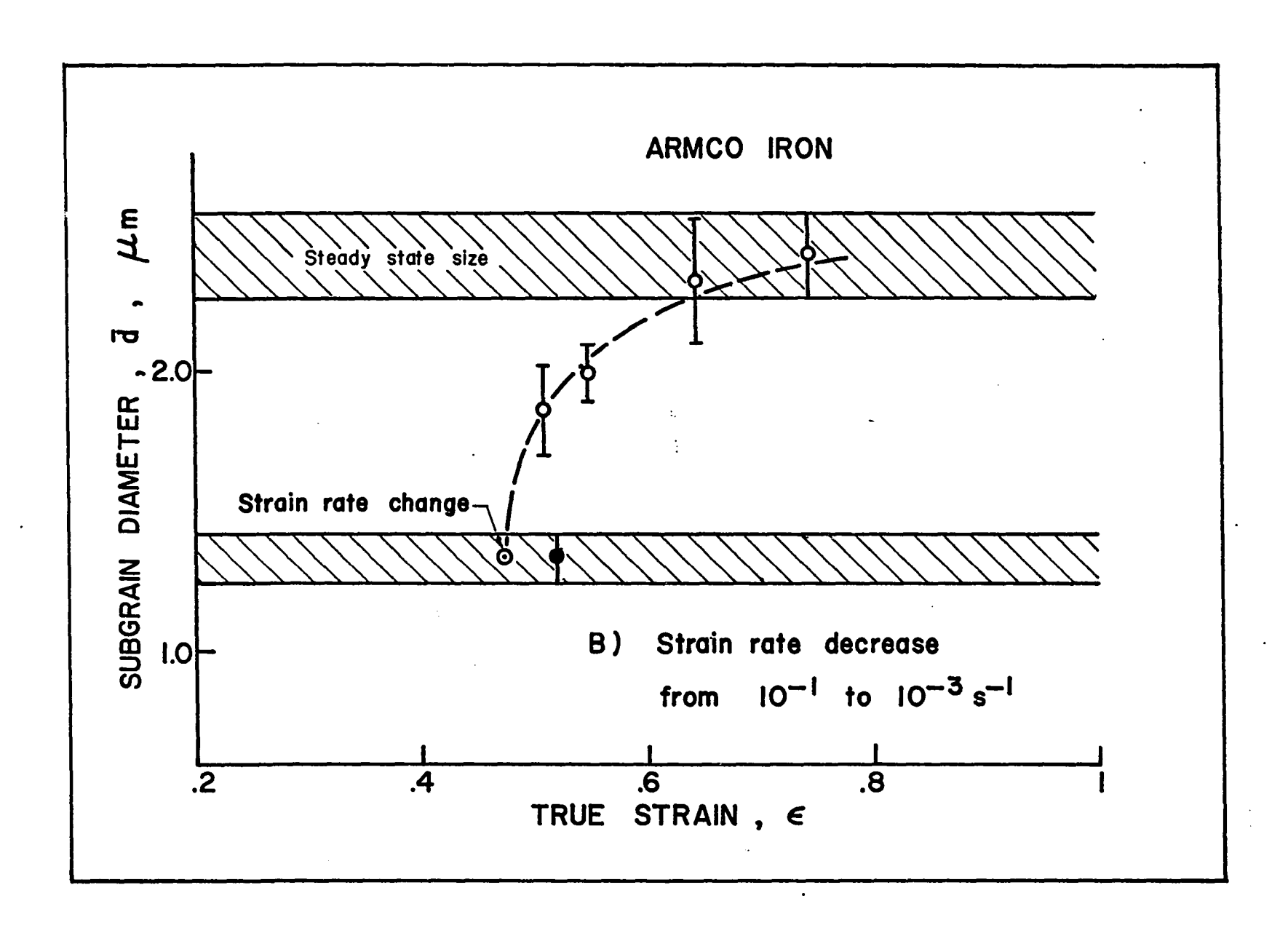
Strain rate	ε	σ psi	Quench Delay (s)	<u>d</u> μm	95% conf. limit (±) μm	L um	95% conf. limit (±) μm
10 <sup>-3</sup>	0.37	17,200	2	2.11	0.26		_
	0.82	18,000	2	1.92	0.21	1.64	0.29
10 <sup>-1</sup>	0.53	30,000	2	1.26	0.10	_	_
10	0.63	32,000	. 2	1.48	0.09	1.12	0.06
Original/Final			<del></del>				
<del></del>	0.41	30,080	2 -	2.15	0.18	1.70	0.14
$10^{-3} / 10^{-1*}$	0.44	31,900	2	1.93	0.15	1.54	0.09
10 / 10	0.47	30,800	2	1.87	0.21	1.22	0.23
	0.63	29,800	2	1.43	0.17	1.10	0.17

<sup>\*</sup> Change of strain rate at strain of 0.38

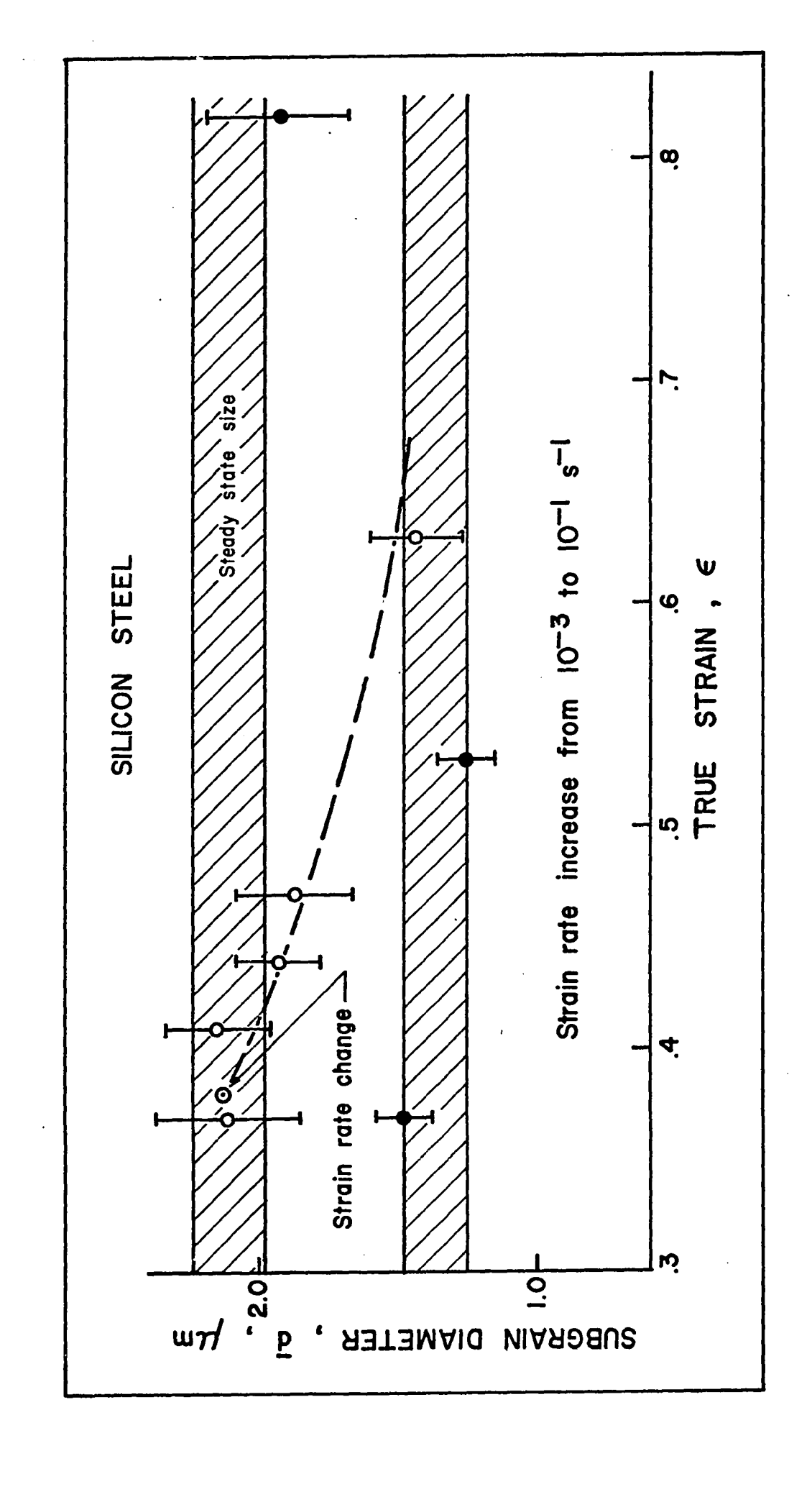
Variation of subgrain size during the transient deformation of Armco iron:

- a) strain rate increase
- b) strain rate decrease

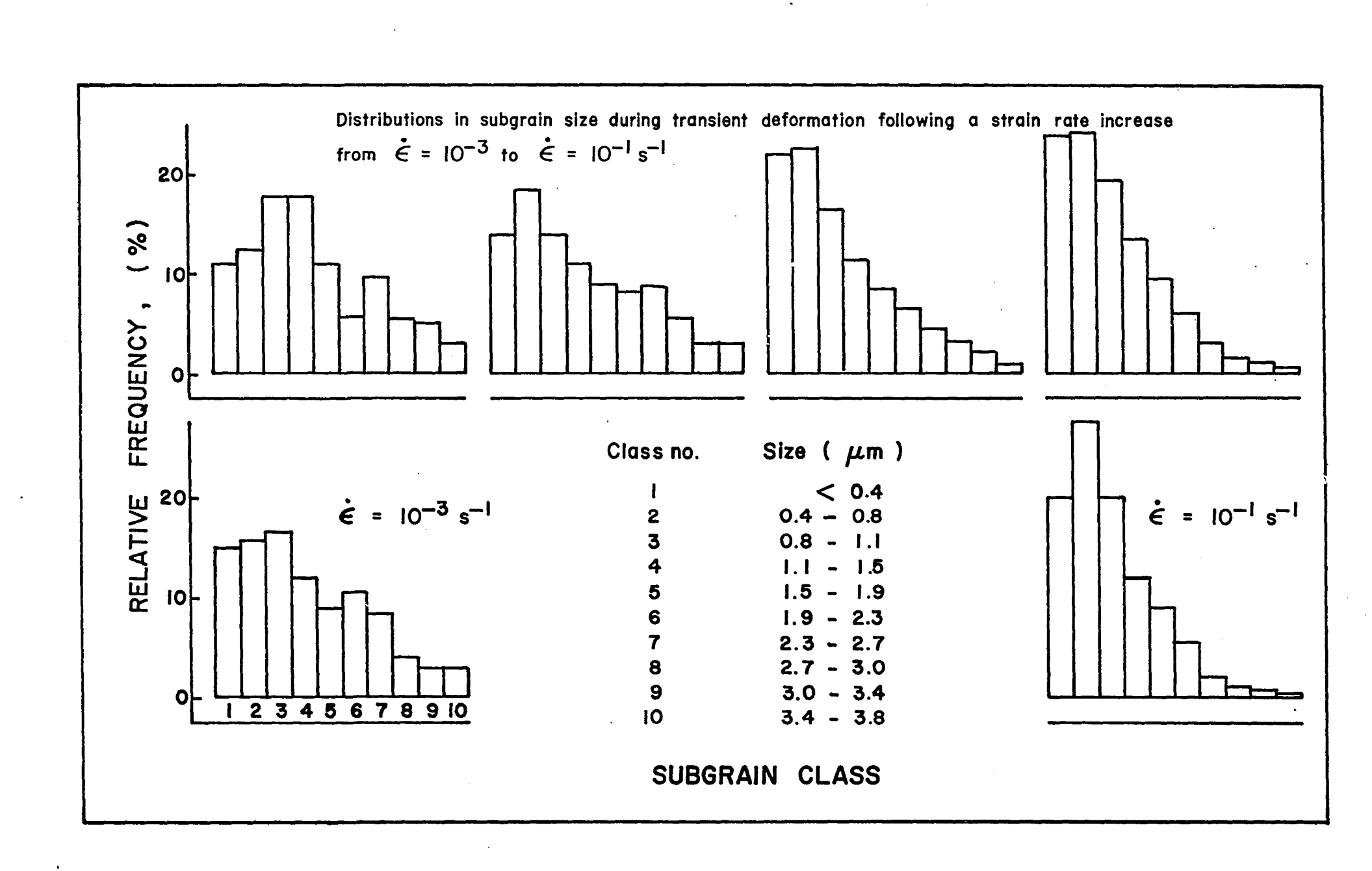




Variation of subgrain size during the transient deformation of silicon steel.



Subgrain size distributions in silicon steel during transient deformation following a strain rate increase.



during transient deformation following a strain rate increase. The mean subgrain size can be seen to decrease and the relative percentage of smaller subgrains to increase as the structural changes take place. The substructural observations described above will be discussed in more detail and interpreted with reference to the stress-strain curves in the next chapter.

### Chapter 5

#### DISCUSSION

## 5.1 True Stress-True Strain Curves

Figs.12 to 18 depict the stress-strain curves obtained in the present investigation. These curves will now be discussed with particular reference to the transient region following a sudden strain rate change.

## 5.1.1 General features of the curves

As far as the continuous tests are concerned, the flow stress can be seen to increase initially due to high temperature work hardening, and then to remain approximately constant with increasing strain. However, in certain cases the steady state flow stress was observed to increase slightly with increasing strain, as shown in Fig.13. This can be attributed to lubrication breakdown at the lower strain rates and to consequent barrelling during compression. It should be noted that the slight increase is initiated at the highest strains. In fact, if deformation is carried further, then the flow stress can increase noticeably as observed by Uvira (25). In Fig.12, at the lowest strain rate, a slight peak in flow stress can be seen to precede the establishment of the steady state. The peak, present in torsion tests of similar materials, has not been regularly observed in the present investigation, however.

Figs.13, 14a, 15a, 16 and 18 indicate that at the highest strain rates the flow stress decreases at high strains. This is not believed to be a material property but to be the result of overloading the Instron. During testing, the loads increase continuously because of the increase in cross sectional area of the compressed cylinders. At the highest strains, the loads approach the maximum values that the Instron crosshead drive will tolerate. Once the machine capacity is exceeded, the load and contraction curves can no longer be relied on, even though the overload fuses do not blow. The loads corresponding to the drop in flow stress are of the order of the maximum permissible and the recorder decrements are believed to be due to "slipping" of the machine. The fact that the contraction curves for high and low strain rates do not superimpose at the highest strains can be quoted in support of this conclusion. The true stress-true strain curves exhibiting this drop at high strains still show a well defined steady state at intermediate strains.

Regarding the elastic corrections, it should be noted that they are more substantial for the higher strain rate curves. This is predictable since the corrections are a function of load (Eq.(4-3)) and, at the higher stresses developed under high strain rate conditions, the corrections are larger than at the lower stresses. This can also be seen from the curves of Fig.13.

In general the stress-strain curves can be reproduced within a few percent. However, in some cases they differ by larger amounts. This can be attributed to differences in initial structure, such as local preferred orientation or large local grain size, or to compositional differences.

The above observations apply to the region preceding the change in the deformation conditions. The effect of a sudden change in strain rate can be seen in Figs.14 to 20. After the strain rate change, the elastic corrections are larger for an increase in  $\dot{\epsilon}$  than for a decrease in  $\dot{\epsilon}$ , as shown in Figs.14a and b and Figs.15a and b. The steady state in flow stress appears better defined for the uncorrected curve, particularly for the Armco iron. In both cases, however, the slow transient is well defined.

Before discussing further the transient regions it must be stressed that much of the information in the early part of the transient is lost because of the high time constant of the Instron recorder. recorder used had a 1 second/full deflection characteristic. As described in section 1.6.4, the change in stress is almost instantaneous when the strain rate is increased. However, the pen cannot follow such a rapid change because of its maximum speed of 10 in/sec across the paper. The recorded loads always lag in time as long as dL/dt > m. Here L is the recorded load, m is the slope of the pen trace when the full load signal is fed into the recorder amplifier and t is the time indicated on the chart running at constant speed. Thus, in Figs. 14a, 15a, 16 and 18, the early steep part of the transient is not representative of the actual stress change. This is unfortunate because useful and important information is clearly lost in this region. What may possibly take place during the early transient will be described in the next section, by extending the present results obtained for a decrease in strain rate to the case of a strain rate increase.

A further source of error should be mentioned for completeness.

The initiation of a strain rate change by manual actuation of the magnetic

clutch produced vibrations in the Instron frame and in the strain gauge extensometer. These vibrations were recorded together with an apparent unloading of the sample and are therefore included in the computed curves. At the higher strain rates, the vibrations persisted for the entire early transient and therefore affected all the early part of the stress-strain curves. As will be seen in the next section, important features of the stress-strain curve can be obscured in this part of the transient.

## 5.1.2 Characteristics of the transient region

When the strain rate is decreased (Figs.14b, 15b, and 17), the stress drops abruptly, then increases for approximately 1% strain, and finally decreases to the level characteristic of the steady state under the new strain rate. Even in the case of the silicon steel, where no gradual transient was observed, the slight initial increase in stress was detected, as indicated in Fig.15b. The question that arises is whether this behaviour is due to a material property or is an effect of the testing machine.

If the increase in stress is a machine effect, it corresponds to a reloading following a temporary partial removal of the load. This removal of the load would be due to the gear change during the strain rate change operation. The magnetic clutch-lever used for a strain rate change goes through a neutral position and it is possible that in this position the load is partially removed. The fact that similar decreases occur on both strain rate increases and decreases supports this hypothesis. This is shown in Figs.14a and 15a by the vertical lines at the strain rate change positions. The load drop must be visualized as taking place over a small fraction of a second, that is during the gear

shifting operation. Upon a strain rate decrease the dip is more noticeable, perhaps because reloading takes longer at the slower speed. From the above discussion, it appears likely that unloading does in fact take place during the strain rate change.

A small dip can also be explained in terms of substructural modifications within the material. If this alternative is valid, then a similar but opposite peak should be observed at the onset of the gradual transient that follows a strain rate increase. Unfortunately the peak, if present, is not observed because the pen does not follow the true stress variation in the early transient for the reasons given previously.

It has been shown in section 1.6.4 that the strain rate can be given in the form:

$$\dot{\varepsilon} = \alpha b \rho_{\rm m} \bar{v} \tag{1-31}$$

or as 
$$\dot{\varepsilon} = B' \alpha b \rho_m \sigma^{*m}$$
 (1-32)

This last equation can be rewritten as: \*\*

$$\dot{\varepsilon} = B''\emptyset \exp(\frac{-\Delta H_O}{kT}) \exp(\frac{b\overline{A}\sigma^*}{kT})$$
 (5-1)

Here  $\Delta H_{\text{O}}$  is the apparent activation enthalpy in the absence of stress

b is the burgers vector

A is the mean activation area

B" is a geometric constant

 $\emptyset = \rho_m b v \overline{\ell}_2$ 

 $\boldsymbol{\rho}_{m}$  is the mobile dislocation density

<sup>\*\*</sup> In Eq.(5-1), it is assumed for convenience that  $\Delta S \simeq 0$ 

 $\nu$  is an obstacle attempt frequency, and

 $\bar{\ell}_2$  is the distance between successive barriers in obstacle or drag controlled glide  $^{(95)}$ .

The effective stress  $\sigma^*$  can be expressed in terms of the flow stress  $\sigma$  and the back stress  $\sigma_R$  as:

$$\sigma^* = \sigma - \sigma_{\rm B} \tag{5-2}$$

When a strain rate decrease in initiated, the conditions must gradually change from those initially given by:

$$\dot{\hat{\epsilon}}_1 = \alpha b p_m \bar{v}_1 \tag{1-31}$$

to those of: 
$$\dot{\epsilon}_2 = \alpha b \rho_{m_2} \bar{v}_2$$
 (1-31)

The manner in which the effective stress must decrease instantaneously as a result of the stress dependence of the average dislocation velocity (Eq.(1-32)) has already been described. According to this view, subsequent slow changes in the substructure lead to slow decreases in  $\boldsymbol{\sigma}_{_{\boldsymbol{R}}}$  and thus in the flow stress  $\sigma$ . However, it is likely that rapid adjustments in the terms  $\emptyset$  and  $\rho_{m}$  take place in the moments following the strain rate change (95). In the case of a strain rate decrease, the dislocation density  $\rho_{\text{m}}$  is initially too high for the second set of conditions. The  $\rho_m$  excess means that lower values of  $\overline{v},~\sigma\star$  and  $\sigma$  (Eqs.(1-31), (1-33) and (5-2) respectively) are required initially than when the final value of  $\rho_{m}$  is attained. Thus, the initial excess in  $\rho_{m}$  produces the first half of the dip. The second, rising part of the dip is due to the decrease of  $\rho_m$  to its stable value, accompanied by appropriate increases in  $\bar{\mathbf{v}}\text{,}$  $\sigma^{\bigstar}$  and  $\sigma. \;$  Finally, with  $\rho_m$  and  $\bar{v}$  relatively constant, the further decrease in  $\sigma$  is due to the slow decrease in  $\sigma_{\mbox{\scriptsize B}}$  which accompanies the substructural changes.

The experimental observations in the case of strain rate decreases can be interpreted in terms of the above description as an alternative or in addition to the machine unloading explanation. However, the  $\rho_{m}$  adjustments for a strain rate increase should lead to a slight peak in the effective stress, just after its sudden increase and prior to the back stress changes. Unfortunately, due perhaps to recorder limitations, this peak was not observed, so that the operation of the mechanism of  $\rho_{m}$  adjustment cannot be considered to be absolutely verified in the present experiments.

# 5.2 Microstructural Changes during Transient Deformation

The changes in the flow stress levels discussed above are paralleled by similar readjustments of the substructure. Generally speaking, the substructure present during a transient following a sudden strain rate change does not appear to be markedly different from that which characterizes the steady state regime. No abrupt changes in the dislocation substructure seem to occur during the transient stage. Rather, rapid changes in the dislocation density and gradual changes in the subgrain size seem to be taking place toward values appropriate to the new steady state substructure. The latter changes occur fairly slowly in both Armco iron and silicon steel. Prior to a discussion of these changes, various aspects of the subgrain size measurements will be considered.

### 5.2.1 Subgrain size determination

From Tables VI and VII, it can be seen that the standard errors in subgrain size measurement are fairly substantial. The 95% confidence limits are in general of the order of ±0.1 to 0.2, leading to relative errors of the order of 5 to 10%. These errors are, however, quite

satisfactory when compared to similar subgrain measurements in the literature (25,26,89-92). It must be noted that the standard deviations computed in the present investigation do not include the effect of experimental errors resulting, for example, from unresolved sub-boundaries. Since electron microscopy operates on a diffraction principle it can arise that at a particular sample tilt, the dislocations in a given sub-boundary will be largely out of contrast. Thus the measured mean subgrain diameter would be higher than the true value. Furthermore the high contrasts encountered between subgrains on a given plate can hinder the resolution of sub-boundaries in the lighter and the darker regions.

It was noticed in the present work that when the measurements were made on carefully traced copies of the electron micrographs, a smaller mean linear intercept or mean subgrain diameter resulted. It also appears that the criteria used in identifying a sub-boundary are important. Whenever a kink was observed in a cell wall, the possible presence of a dislocation array out of contrast was carefully checked. For instance, a similar kink in the opposite cell wall was in general taken as conclusive of the presence of an out of contrast sub-boundary. Using this careful counting method and always applying the same criteria, the mean subgrain diameters were decreased by a factor of two.

This can explain why the present results do not correlate perfectly with the subgrain size measurements carried out by Uvira  $^{(25)}$  on the same material. From Table V it can be seen that the subgrain diameters determined by Uvira are larger than those obtained in the present investigation; e.g., his  $\bar{d}^{-1}/\sigma$  plots  $^{(25)}$  suggest that subgrain sizes roughly twice those reported here should have been obtained. Thus, although his results and the present ones are not interchangeable, the method adopted here is well

suited to studies in which substructural changes are followed and relative sizes compared.

It should be borne in mind that the mean subgrain diameter used here is not a rigorously defined physical quantity, since a true average diameter is accessible only through topological parameters which must eventually be measured by serial sectioning  $^{(96)}$ . The topological parameters of importance in metallography are the number in unit volume  $(N_V)$  and the connectivity in unit volume. The only exact method of determining an average subgrain diameter  $\bar{D}$  is then given by  $^{(96)}$ 

$$\bar{D} = 2 \frac{N_A}{N_V}$$
 (5-3)

where  $N_{\boldsymbol{A}}$  is the number of subgrain intercepts in unit area, and

N<sub>V</sub> is the number of subgrains in unit volume However, undertaking serial sectioning measurements of this type is a very arduous task. Therefore, in the present work the three basic Euclidean parameters (volume, area and length) were used, rather than the topological parameters. Both mean areal intercept  $\overline{A} = 1/N_A$ , and mean linear intercept  $\overline{L} = 1/N_L$ , where  $N_L$  is the number of intercepts per unit length of test line, were determined and the results obtained are shown in Tables VI and VII as  $d = \sqrt{\overline{A}}$  and  $\overline{L}$ . These parameters are the only geometric parameters of a single phase system that can be derived rigorously from a two-dimensional microsection alone (96).

## 5.2.2 Subgrain size distributions

Whichever method of subgrain size measurement is used, Euclidean or topological, only an average value is obtained. Not all the subgrains of a given sample have the same shape and size, so there is always at

least a size variation. (97) In the present work, a few representative silicon steel samples were analysed for size variation, and the distributions are shown in Fig.39. The diagrams actually illustrate the changes in distribution brought about by a strain rate increase. Each distribution is expressed in terms of the same subgrain size classes. As the strain after the strain rate change increases, it can be seen that the percentage of subgrains in the small classes increases at the expense of the others. This results in a gradual decrease in subgrain size. Fig.39 shows that changes in subgrain size are still taking place at strains of 0.25 after the strain rate increase.

## 5.2.3 Sub-boundary misorientation and dislocation density

The other characteristics that can be used to describe the substructure have not been investigated to the same extent as the subgrain size. In the present work, using qualitative methods alone, the misorientations between neighbouring subgrains were not observed to vary in any systematic way. If a trend exists, it is probably masked by the scatter in experimental results. Similar observations have been reported in "constant-structure" tests on 304 stainless steel (98). In this work, the misorientations were determined by the shift in the Kikuchi lines associated with adjoining subgrains. No regular change in misorientation paralleled the change in stress.

Although no quantitative work was carried out regarding dislocation densities in the present work, it appears that the dislocation density within the subgrains increases with the increase in stress during the transient. This is foreseeable inasmuch as two different dislocation densities can be expected to characterize the initial and final states of a test.

Stress reduction creep tests have been carried out by various researchers (62,70,71,99). Their findings suggest that the substructural changes following the drop in stress are extremely complicated. Following the sudden reduction in stress, an abrupt drop in creep rate is always observed for all materials tested. However, during the subsequent transient period, the creep rate either increases or decreases to the appropriate steady state value. For a normal transient, i.e. when the initial decrease in strain rate is followed by a slow increase, the substructural changes can be associated with reductions in the back stress in the relation

$$\dot{\varepsilon} \propto \emptyset \exp(\frac{V(\sigma - \sigma_B)}{kT}) \tag{5-4}$$

As  $\sigma_B$  decreases to its new steady state value, the exponential term increases and so does the strain rate. In this case, the changes in the dislocation density  $\rho_m$  or the term  $\emptyset \propto \rho_m$  are negligible compared to the changes in the exponential term.

When an inverted transient is observed, however, the term  $\Delta \exp(\frac{V(\sigma - \sigma_B)}{kT}) \text{ becomes of lesser importance compared to the changes in the mobile dislocation density, i.e. in <math>\emptyset$ . Immediately after the stress reduction,  $\rho_m$  is much higher than the steady state value for the second stress. As the dislocation density decreases to the appropriate steady state density, so does the strain rate, since  $\dot{\epsilon} \propto \rho_m$ .

A transition from normal to inverted transients with increasing stress, has been observed for an Fe - Mo solid solution (100). A change in the relative magnitude of  $\emptyset$  and  $\Delta \exp(\frac{V(\sigma-\sigma_B)}{kT})$  as outlined above, leads to a simple explanation of this observation. Thus it appears that the dislocation density can play an important role in transient deformation, particularly when inverted transients are present.

#### 5.2.4 Substructures under transient conditions

In view of the above discussion, the changes taking place along the transient region can be visualized as follows. Immediately after the strain rate change, the mobile dislocation density changes rapidly giving rise to an inverted transient in the true stress-true strain curve. After a few percent of strain, the subgrain size and the dislocation density within the subgrains adjust to the new deformation conditions. This occurs by means of concurrent work hardening and recovery processes. In the case of a strain rate increase, the dislocation velocity increases instantaneously because of the imposed higher strain rate. Since the dislocation density is initially too low, the initial increase in flow stress is too large and, as  $\rho_{\text{m}}$  adjusts, it decreases again over a few percent of strain. Then the subgrain size starts to decrease toward the new steady state value. The processes by which this occurs are not clearly understood. The sub-boundaries may migrate by glide and climb of the dislocations or they may relocate by the process of "repolygonization". In the latter process, the subboundaries are continuously breaking-up and reforming until the average distance between cell walls reaches the value characteristic of the steady state for the second strain rate. In the meantime the dislocation density increases along the transient to the value appropriate to the higher strain rate.

## 5.3 Applicability of the Effective Stress Model

The above observations can be interpreted in terms of the effective stress models introduced in Chapter 1 and discussed in sections 5.1 and 5.2 above. According to these models, the strain rate  $\dot{\epsilon}$  can be

expressed in terms of three structural parameters as follows:

$$\dot{\varepsilon} = B''\emptyset \exp(\frac{-\Delta H_0}{kT}) \exp(\frac{b\bar{A}(\sigma - \sigma_B)}{kT})$$
 (5-2)

The three structural parameters are the pre-exponential  $\emptyset$ , which is proportional to the mobile dislocation density, the mean activation area  $\overline{A}$  and the internal or back stress  $\sigma_B$ . The experimental results of the present investigation seem to support such an interpretation of high temperature deformation. However, depending on the material, different features of the substructure can be associated with the structural parameters.

In the case of the Armco iron, upon a strain rate decrease,  $\sigma^*$  drops abruptly and then increases slightly due to the adjustments in  $\emptyset$ , i.e. to a decrease in the mobile dislocation density. The major substructural changes follow. The subgrain size increases and the dislocation density within the subgrains decreases, perhaps more quickly. This is associated with a decrease in  $\sigma_B$  to the constant value appropriate to the new steady state. Thus in this case  $\sigma_B$  is controlled by either the sub-boundary density  $\overline{d}^{-1}$  or possibly by the network dislocation density  $\rho_m$ . The present work does not definitely establish the sub-boundaries as the source of the back stress in the Armco iron, although this seems to be more likely than the alternative of the network density. Such a preference is based on the observation that, during the transient, the changes in sub-boundary density and in the flow stress are both fairly slow, whereas the changes in the network density seem to be fairly rapid.

For completeness it should be noted that the nature of the sub-boundaries may also be of importance. In hot rolled  $^{(35)}$  or extruded  $^{(24)}$  aluminum, the sub-boundaries were observed to change with a decrease in Z

from dense ragged tangles to neat regular networks of dislocations. Although creep and hot working studies do not reveal a similar change in misorientation with Z, the complexity of the dislocation structure in a sub-boundary and the associated quantities of redundant dislocations both increase with Z. (S.Weissman; discussion, Ref.26). This "redundancy" of the dislocation content could also affect the back stress.

In the case of the silicon steel the situation is different. An important aspect of the present experimental results is that the subgrain size continued to change during the so-called steady state deformation of silicon steel. Comparison of Figs.18 and 38 shows that, although the steady state stress is reached after strains of 0.01 to 0.08, the mean subgrain diameter reaches its steady state value only after strains of 0.25 to 0.35. Thus it seems clear that the subgrain size does not directly control the back stress in this material. Instead the back stress is more likely to be associated with the network dislocation density  $\rho_{\rm T}$ , for which much shorter transients can be expected.

Somewhat similar conclusions were reached in recent creep investigations of 304 stainless steel  $^{(98)}$  and of Fe-0.75 Mn  $^{(71)}$ . It should be noted that, like silicon steel and unlike Armco iron, both these materials contain appreciable solute. In Fig.12 of Cuddy's work  $^{(98)}$ , the increase in dislocation density within the subgrains  $\rho_{\rm T}$  and in sub-boundary density  ${\rm d}^{-1}$  are both compared with the increase in the internal or back stress.  $\sigma_{\rm B}$  appears to increase linearly with  $\rho_{\rm T}$  and to be proportional to  ${\rm d}^{-2}$ . Cuddy concludes from his observations that the dislocations within the subgrains are more effective in producing an internal stress than are the sub-boundaries  $^{(98)}$ . In his work on iron-manganese solid solutions  $^{(71)}$ , Ishida reached a similar conclusion which can be paraphrased as follows.

The subgrain boundaries do not seem to control the creep strength and second stage recovery (the gradual transient) is associated instead with the change in dislocation density.

To summarize the differences with respect to strain rate changes, the behaviour of the two present materials can be interpreted as follows. In Armco iron, a relatively pure metal, the change in the sub-boundary spacing accounts for the increase in flow stress. Immediately following a strain rate increase and the adjustments in the dislocation density, the strengthening of the material is paralleled by an increase in the subboundary density. In terms of the offective stress model, the back stress can thus be associated with the sub-boundary density or subgrain size. However, in silicon steel, for reasons not yet known, the effect of the sub-boundaries is masked by the network density. Although the subgrain size does change after the rapid adjustments of  $\boldsymbol{\rho}_{\text{m}}$  and  $\boldsymbol{\rho}_{\text{T}}\text{,}$  the flow stress does not increase further. The back stress is no longer associated with the sub-boundaries but with the network density. In terms of the effective stress model, when the strain rate is changed, the back stress associated with the network density adjusts itself fairly quickly and no long term transient is observed.

#### 5.4 Industrial Significance of the Present Results

It is important for the design of industrial equipment to be able to predict working loads in processes such as rolling, extrusion or forging. In such processes, the deformation conditions do not remain constant throughout the operation. The local strain rates and temperatures vary within the material and are also a function of time. Moreover several deformation operations can follow one another after minimal delays, as in

ten-stand continuous mills. Each operation will then be affected by the previous history of the sample. Thus industrial deformations involve transients in temperature and strain rate which are typified by the transient tests studied here.

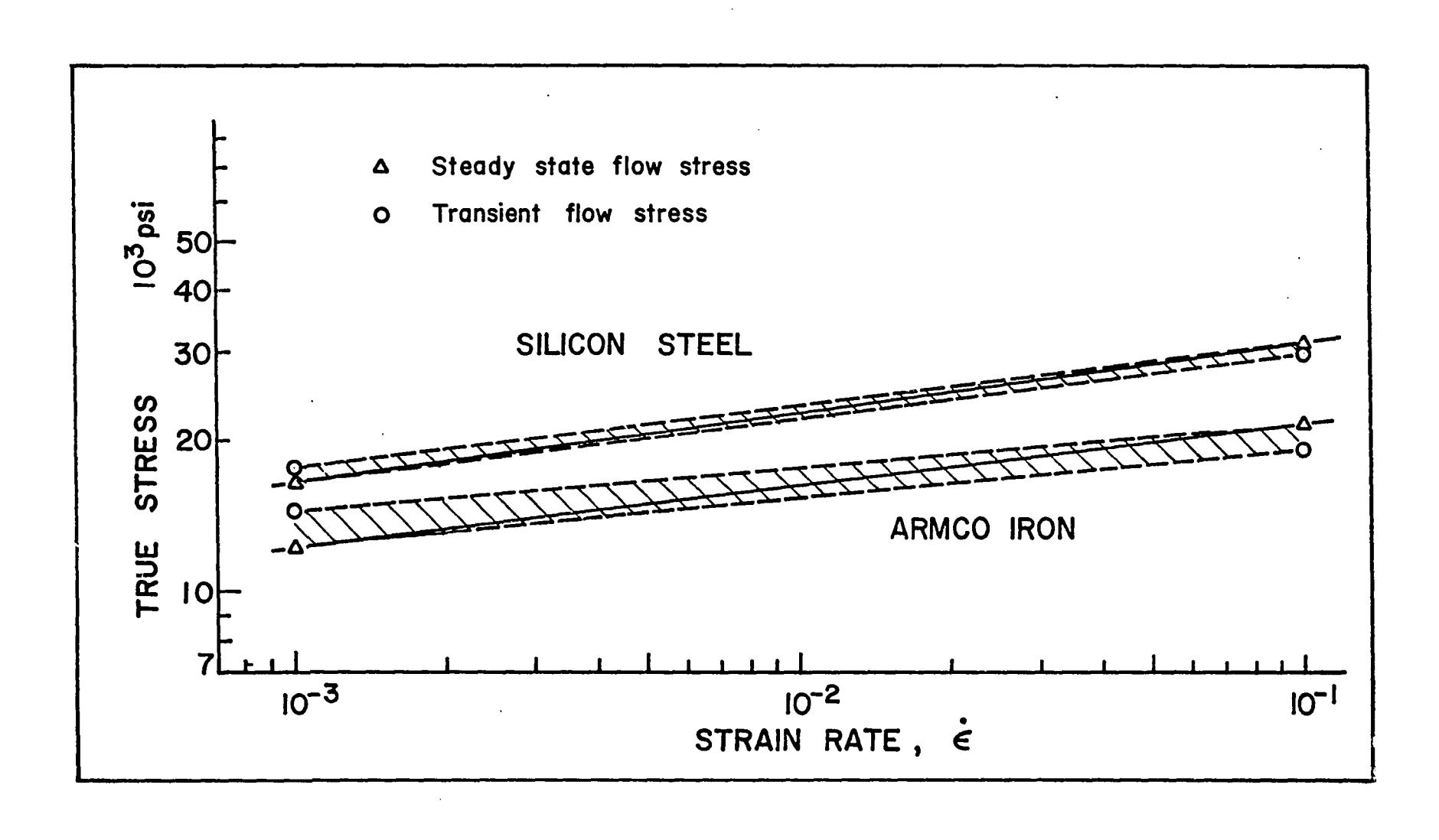
The industrial working load depends on the instantaneous flow stress, which is in turn made up of two components. The first of these is the effective stress, which is determined by the instantaneous strain rate imposed by the equipment. The second component is the back stress, which is associated with the substructure inherited from the previous thermomechanical history of the sample. With respect to the latter, it is important to know for instance whether the structure produced in the first or second rolling stand will affect the flow stresses developed further down the line, e.g. in stands four or six.

If the "previous history" of the deformed material persists for strains of 30% or more, it is clear that the loads during the later operations will be significantly influenced by early operations. However, if the internal stress changes rapidly over a few percent of strain, the previous history will not be of primary importance in determining the flow stress.

From the present results it appears that, in pure metals, the previous history is of moderate importance, since about 18% of the change in flow stress is governed by slow changes in internal stress. By contrast, in solid solution alloys, the "previous history" is erased within a few percent of strain, since the back stress is now governed by the rapid changes in total dislocation density. In general, of the two components that affect the loads, the effective stress is the larger. Fig. 40 illustrates the above remarks. On this diagram, the steady state flow

FIGURE 40

Comparison of transient and steady state flow stresses



stresses are joined by a heavy line. The flow stress values corresponding to the two-order of magnitude increase or decrease in strain rate, and joined by a dashed line, are also plotted. The heavy line indicates the flow stresses corresponding to the extreme of infinitely slow changes in strain rate (i.e. to steady state deformation). The dashed lines indicate the flow stresses associated with instantaneous strain rate increases or decreases. For most industrial operations, the rates of strain rate change are intermediate between the present instantaneous and infinitely slow rates. Thus the flow stresses associated with these operations will be found between the limits indicated in the diagram. The graph indicates that, when the strain rates vary continuously as in rolling or extrusion, the flow stress will remain in the narrow cross-hatched region. This band is slightly wider in the purer material. Thus it appears that, under conditions of changing strain rate, the working loads can be predicted to a first approximation from steady state data, such as those depicted in Fig.2.

### 5.6 Suggestions for Further Work

From the above considerations it appears that further work is necessary in order to assess the validity of the effective stress model. Also additional research is required to determine more definitely the features of the dislocation substructure which are associated with the internal stress. It would also be desirable to isolate the configuration of the dislocation network which causes recovery after a sudden strain rate change.

With regard to the mechanical aspect of the experiments, the initial part of the transient is clearly of importance in determining the

response of the material to sudden changes of strain rate. As far as strain rate decreases are concerned, the mechanical behaviour of the materials tested has been satisfactorily followed. However, for strain rate increases, faster recorders must be used in order to follow the "instantaneous" and rapid changes in flow stress.

In addition a truly instantaneous strain rate changer would have to be designed and added to the Instron machine. The design should allow for instantaneous changes of any magnitude within the performance range of the Instron. Work in this direction has already been initiated by the author. Such a device should also avoid shaking the Instron frame and thus prevent the vibrations of the strain gauge extensometer described earlier. Not until the stress-strain curves can be faithfully recorded will a complete study of the mechanical aspects of transient deformation be possible.

#### CONCLUSIONS

The present investigation shows that the substructural changes taking place during transient deformation are quite complex. An attempt has been made to explain the observations obtained by means of electron microscopy in terms of an effective stress model and the following general conclusions were reached:

- 1. The substructures produced during transient deformation have features similar to those of steady state microstructures. Dynamic changes are occurring, however, in the mean subgrain size and in the dislocation density within the subgrains. The final substructures developed after a strain rate change are similar to those obtained through steady state deformation. In particular, the subgrain size changes gradually from the initial to the final steady state value over strains of 0.25 to 0.35 for both materials. When the strain rate is increased, the subgrain size decreases. It increases upon a strain rate reduction.
- 2. Following a strain rate increase or decrease, there is an immediate rapid increase or decrease in flow stress. This rapid change can be attributed to the change in stress required to make the existing dislocations move at the new mean strain rate. In terms of the effective stress model, this rapid change corresponds to an effective stress change.
- 3. After the rapid change in flow stress, there is some evidence for a small inverse transient in flow stress. More rapid recorder

response is required to follow this transient adequately. The transient, which takes place in both materials over strains of 0.01 to 0.05, can be associated with a fairly rapid adjustment in the mobile dislocation density, taking it from the original to the final steady state value.

- 4. In Armco iron, the gradual changes in the flow stress which follow are paralleled by slow substructural modifications. The subgrain size slowly changes from the original to the final steady state value. In this case the sub-boundary density is considered to be the source of the back stress. The slow increase in flow stress is taken as characteristic of the behaviour of pure metals.
- panied by gradual flow stress changes. Instead, the flow stress associated with the new strain rate is established within strains of 0.01 to 0.08. In this case, the network dislocation density, which can quickly adjust to new conditions of deformation, is considered to be the source of the back stress. The absence of slow transients is regarded as characteristic of the behaviour of solid solution alloys.
- proportionately larger than the changes in internal stress. Thus, immediately following a change in strain rate, the flow stress is close to the value characteristic of the new steady state. For the design of forming equipment, the working loads can therefore be predicted, to a first approximation, from steady state data.

#### REFERENCES

- C. Rossard and P. Blain: Rev. Mét., 59, 223-235, 1962.
- C. Rossard and P. Blain: Rev. Mét., 55, 573- , 1958.
- 3. C. Rossard and P. Blain: Mém. Sci. Rev. Mét., 56, 285-300, 1959.
- 4. C. Rossard and P. Blain: Mém. Sci. Rev. Mét., 57, 173-175, 1960.
- 5. C. Rossard: Mét. Cor.-Ind., 35, No. 415, 102-115; No. 416, 140-153; No. 417, 190-205, 1960.
- 6. C. Rossard: Rev. Mét., 65, 181-195, 1968.
- C. Rossard, A. Le Bon, D. Thivellier, J. Manenc: Mém. Sci. Rev. Mét., 66, 263-270, 1969.
- 8. D. Hardwick and W. J. McG. Tegart: J. Inst. Met., 90, 17-21, 1961-62.
- 9. D. Hardwick, C. M. Sellars and W. J. McG. Tegart: J. Inst. Met., 90, 21-22, 1961-62.
- H. Ormerod and W. J. McG. Tegart: J. Inst. Met., <u>92</u>, 297-299, 1963-64.
- 11. C. M. Sellars and W. J. McG. Tegart: Mém. Sci. Rev. Mét., <u>63</u>, 731-746, 1966.
- 12. M. J. Luton and C. M. Sellars: Acta Met., 17, 1033-1043, 1969.
- 13. M. M. Farag, C. M. Sellars and W. J. McG. Tegart: "Deformation under Hot Working Conditions" (Special Rep. No. 108) London (Iron and Steel Inst.) 60-67, 1968.
- 14. H. P. Stüwe: Acta Met., 13, 1337-1342, 1965.
- 15. H. P. Stüwe: Ref. 13, 1-6.
- 16. G. E. Dieter, J. V. Mullin and E. Shapiro: Ref. 13, 7-13.
- 17. E. Shapiro and G. E. Dieter: Final Rep. Contract N00019-68, C-0131, (Naval Air Systems Command), 1969.
- 18. W. A. Wong: M.Eng. Thesis, McGill University, Montreal, 1965.
- 19. W. A. Wong: Ph.D. Thesis, McGill University, Montreal, 1967.

- 20. H. J. McQueen, W. A. Wong and J. J. Jonas: Can. J. Phys., 45, 1225-1233, 1967.
- 21. H. J. McQueen, W. A. Wong and J. J. Jonas: Acta Met., <u>15</u>, 586-588, 1967.
- 22. W. A. Wong, H. J. McQueen and J. J. Jonas: J. Inst. Met., <u>95</u>, 129-137, 1967.
- 23. W. A. Wong and J. J. Jonas: Trans. TMS-AIME, 242, 2271-2280, 1968.
- 24. J. J. Jonas, H. J. McQueen and W. A. Wong: Ref. 13, 49-59.
- 25. J. L. Uvira: Ph.D. Thesis, McGill University, Montreal, 1967.
- 26. J. J. Jonas, D. R. Axelrad and J. L. Uvira: Proc. of Int. Conf. on the Strength of Metals and Alloys, Tokyo, 1967, 257-267; Supp. to Trans. Japan. Inst. Met. 9, 1968.
- 27. J. L. Uvira and J. J. Jonas: Trans. TMS-AIME, 242, 1619-1626, 1968.
- 28. H. J. McQueen: Ref. 26, 170-177.
- 29. H. J. McQueen: J. Metals, 20, 31-38, 1968.
- 30. H. J. McQueen: Materials Technology An Inter-American Approach ASME (new-York), 379-388, 1968.
- 31. J. Jonas, C. M. Sellars and W. J. McG. Tegart: Met. Reviews, 14, 1-24, 1969.
- 32. J. J. Jonas: Acta Met., <u>17</u>, 397-405, 1969.
- 33. D. J. Abson and J. J. Jonas: Met. Sci. J., 4, 24-28, 1970.
- 34. M. J. Luton and J. J. Jonas: Acta Met., 18, 511-517, 1970.
- 35. J. P. Immarigeon and H. J. McQueen: Can. Met. Quart., 8, 25-34, 1967.
- 36. H. Bühler and H. W. Wagener: Bander, Bleche, Rohre, <u>6</u>, 625-630, 667-668, 677-684, 1965.
- 37. H. Bühler and H. W. Wagener: Z. Metallkde., <u>57</u>, 825-830, 1966; 58, 136-144, 1967.
- 38. J. J. Jonas and J. P. Immarigeon: Z. Metallkde., 60, 227-231, 1969.
- 39. J. F. Alder and V. A. Phillips: J. Inst. Met., 83, 80-86, 1954-55.
- 40. F. Garofalo: Fundamentals of Creep and Creep Rupture in Metals, Macmillan, New York, 1965.

- 41. D. McLean: Mechanical Properties of Metals, 285-334, John Wiley and Sons, New York, 1965.
- 42. H. Conrad in Mechanical Behaviour of Materials at Elevated Temperature, ed. J. E. Dorn, McGraw Hill, New York, 149-217, 1961.
- 43. G. Schoeck in Ref. 42, 77-107.
- 44. F. Garofalo: Trans. AIME, 227, 351-356, 1963.
- 45. G. Gagnon: Ph.D. Thesis, McGill University, Montreal, 1968.
- 46. J. J. Jonas: Trans. ASM, 62, 300-303, 1969.
- 47. J. E. Bird, A. K. Mukherjee and J. E. Dorn in Quantitative Relation Between Properties and Microstructure, ed. D. G. Brandon and A. Rosen, Israel University Press, Jerusalem, 255-342, 1969.
- 48. R. E. Reed-Hill: Physical Metallurgy Principles, D. Van Nostrand, New York, 1964.
- 49. J. G. Byrne: Recovery, Recrystallization and Grain Growth, Macmillan, New York, 1965.
- 50. A. H. Clauer, B. A. Wilcox and J. P. Hirth: Acta Met., <u>18</u>, 381-397, 1970.
- 51. F. H. Hammad and W. D. Nix: Trans. ASM, 59, 94-104, 1966.
- 52. D. McLean: J. Inst. Met., 80, 507-519, 1951-52.
- 53. O. D. Sherby and J. E. Dorn: Trans. AIME, 197, 324-330, 1953.
- 54. F. Garofalo, W. F. Domis and F. Von Gemmingen: Trans. AIME, <u>230</u>, 1460-1467, 1964.
- 55. A. Orlová and J. Cadek: Phil. Mag., 21, 495-508, 1970.
- 56. D. McLean: Met. Rev., 7, 481-527, 1962.
- 57. J. J. Jonas, H. J. McQueen and D. W. Demianczuk: Ref. 13, 97-99.
- 58. V. P. Gupta and P. R. Strutt: Can. J. Phys., 45, 1213-1220, 1967.
- 59. J. L. Lytton, C. R. Barrett and O. D. Sherby: Trans. AIME, <u>233</u>, 1399-1408, 1965.
- 60. P. B. Hirsch and D. H. Warrington: Phil. Mag., 6, 735-768, 1961.
- 61. C. R. Barrett and W. D. Nix: Acta Met., 13, No.2, 1247-1258, 1965.
- 62. L. Raymond and J. E. Dorn: Trans. AIME, 230, 560-567, 1964.

- 63. A. K. Mukherjee, J. E. Bird and J. E. Dorn: Trans. ASM, <u>62</u>, No.1, 155-179, 1969.
- 64. J. Weertman: Trans. ASM, <u>61</u>, 681-694, 1968.
- 65. J. Weertman: J. Appl. Phys., <u>26</u>, 1213-1217, 1955.
- 66. J. E. Dorn in Energetics in Metallurgical Phenomena, ed. W. M. Mueller, Vol.1, 241-344, Gordon and Breach, New York, 1965.
- 67. R. W. Bailey: J. Inst. Met., <u>35</u>, 27-43, 1926.
- 68. E. Orowan: J. West Scot. Iron Steel Inst., 54, 45, 1946-47.
- 69. D. McLean: Trans. TMS-AIME, 242, 1193-1203, 1968.
- 70. S. K. Mitra and D. McLean: Met. Sci. J., 1, 192-198, 1967.
- 71. Y. Ishida: Trans. Japan Inst. Met., 9, 120-124, 1968.
- 72. C. R. Barrett, C. N. Ahlquist and W. D. Nix: Met. Sci. J., 4, 41-46, 1970.
- 73. W. G. Johnston and J. J. Gilman: J. Appl. Phys., 30, 129-144, 1959.
- 74. A. T. English and W. A. Backofen: Trans. TMS-AIME, <u>230</u>, 396-407, 1964.
- 75. P. Moore: Ref. 13, 103-106.
- 76. F. Maak and C. M. Sellars: J. Scient. Inst., 42, 900-901, 1965.
- 77. I. A. Bucklow and M. Cole: Met. Rev., <u>14</u>, No.135, 103-118, 1969.
- 78. W. J. McG. Tegart: The Electrolytic and Chemical Polishing of Metals, Pergamon, New York, 1959.
- 79. P. B. Hirsch, A. Howie, R. B. Nicholson, D. W. Pashley and M. J. Whelan: Electron Microscopy of Thin Crystals, Butterworths, London, 1965.
- 80. P. M. Kelly and J. Nutting: JISI, 192, 246-248, 1959.
- 81. G. W. Briers, D. W. Dawe, M. A. P. Dewey and I. S. Brammar: J. Inst. Met., <u>93</u>, 77-80, 1964-65.
- 82. K. R. Carson and W. J. McG. Tegart: J. Scient. Inst., <u>42</u>, 435-436, 1965.
- 83. Y. Le Coadic et A. Bourret: Rapport CEA-R 3258, 1967.
- 84. D. G. Brandon and J. Nutting: Acta Met., 7, 101-110, 1959.

- 85. R. Packwood: Private communication.
- 86. F. Schuckher in Quantitative Microscopy, ed. R. T. DeHoff and F. N. Rhines, McGraw Hill, New York, 201-265, 1968.
- 87. ASTM Standard, Designation E 112-63.
- 88. B. Jaoul: Etude de la Plasticité et Application aux Métaux, 179-180, Dunod, Paris, 1965.
- 89. C. J. Ball: JISI, 191, 232-236, 1959.
- 90. D. H. Warrington: JISI, 201, 610-613, 1963.
- 91. D. M. Keane, C. M. Sellars and W. J. McG. Tegart: Ref. 13, 21-28.
- 92. G. A. Redfern and C. M. Sellars: Ref. 13, 29-37.
- 93. R. T. DeHoff: Ref. 86, 11-44.
- 94. H. W. L. Phillips: J. Inst. Met., <u>58</u>, 47-106, 1942.
- 95. J. J. Jonas: Mat. Sci. Eng., in press.
- 96. F. N. Rhines: Met. Trans., 1, 1105-1120, 1970.
- 97. J. E. Hilliard: Ref. 47, 3-15.
- 98. L. J. Cuddy: Met. Trans., <u>1</u>, 395-401, 1970.
- 99. W. D. Ludeman, L. A. Shepard and J. E. Dorn: Trans. AIME, <u>218</u>, 923-926, 1960.
- 100. A. Fuchs and B. Ilschner: Acta Met., <u>17</u>, 701-710, 1969.